# Low dimensional electronic states at metal surfaces investigated by photoemission and nonlinear optics

## Dissertation

zur Erlangung des akademischen Grades

doctor rerum naturalium (Dr. rer. nat.)

vorgelegt der

Naturwissenschaftlichen Fakultät II
der Martin-Luther-Universität Halle-Wittenberg

von Herrn Mariusz Pazgan
geb. am 22. April 1982 in Nowy Sącz, Polen

angefertigt am
Max-Planck-Institut für Mikrostrukturphysik
in Halle an der Saale

Gutachter

1. Prof. Dr. J. Kirschner

2. Prof. Dr. M. Weinelt

3. Prof. Dr. G. Woltersdorf

Halle (Saale) 17.12.2014 (Verteidigungsdatum)

# Contents

# 1 Introduction

In the last two decades, the role of the size of a studied system has gained a large importance in the natural sciences [1]. Size matters also in solid state physics, as is especially evident when the relevant dimensions approach the atomic scale and quantum effects become defining factors of a system. In recent years, a broad range of experimental and theoretical investigations of systems of reduced dimensionality provided a ground for manipulation of the structural and electronic properties of solid state systems. This was leading to many important applications. Moreover, the Nobel Prize in Physics of the year 2010 for groundbreaking experiments regarding the two-dimensional material of graphene emphasized the practical importance of our understanding of the nanoscale world. One of the most noticeable influences of low dimensional systems is their impact on the development of semiconductor devices, in which also the electronic structure of surfaces and interface regions can play an important role [2]. To understand the relevant chemical and physical mechanisms, the study of model systems under precisely controlled conditions is extremely helpful. For instance, the investigation of adsorbate chemistry involving the electronic excitations at surfaces allowed better control and understanding of various processes at surfaces with the help of alkali atoms as relatively simple model systems [3–5]. Without a deeper understanding of the relevant processes of vibrational excitations, dissociation, desorption, charge transport, catalysis and general chemical reactions [4], the modern era of the epitaxial growth of semiconductors would hardly be possible. Additionally, with the present challenge of developing high efficiency batteries for sustainable energy use [6], the example of single atom substrate catalysts proves the importance of research on the electronic effects in the interaction between single adsorbate atoms and a substrate [7]. Going from a picture of single atom on a surface to a regime of higher adsorbate coverage, quantum effects arise due to confinement of electrons to regions comparable to their de Broglie wavelength [2, 8]. Depending on the remaining available degrees of freedom, a "zero dimensional", "one-dimensional", or "two-dimensional" confining situation can be created at a surface [2, 9]. The resulting structures resemble atoms (quantum dots), wires (quantum wires) and thin films (quantum wells). Especially the two dimensional electron gas in thin film quantum well states, associated with discrete variation of a wide range of physical properties [8], is found to be useful in model investigations concerning quantized electronic states in artificial structures with adjustable physical dimensions. Since numerous advances have been made in this field, a whole branch of so-called "quantum-well-spectroscopy" investigations [8] has provided vital information about quantum well state effects on physical systems. This investigations include the bulk band structure by determination of band dispersions as a function of $k$,

a variety of quantum size effects and properties like the density of states [8], the work function [10], electron-phonon coupling [11–13], surface reactivity [14], the total energy of the system and its stability [15–17], the oscillatory magnetic anisotropy [18, 19], and the exchange coupling between two ferromagnetic films separated by paramagnetic spacer layers [20, 21]. The exchange coupling is responsible for the giant magnetoresistance (GMR), which has revolutionized the magnetic storage technology and found multiple applications in magnetic sensors, magnetic random access memory and spin -valve devices [22]. However, not only the GMR-based devices but also the general development of semiconductor devices in a wide range of applications like light-emitting diodes, semiconductor lasers, and high-electron mobility transistors can be given as examples. Additionally, as mentioned recently in Ref. [23] concerning the magneto-electric charge trap memory (designed out of high quality epitaxial Fe film grown on a Ag(001) single crystalline substrate), the low dimensionality of the system causes the shift of spin-polarized electronic bands, leading to pronounced field driven changes of magnetic properties. This enforces the importance of investigations regarding the electronic structure of low dimensional systems.

In this work, photoemission and non-linear optics are used to probe different types of low dimensional electronic states on metal surfaces. Photoemission spectroscopy has established itself as the most versatile technique for studying the electronic states of solids, surfaces and adsorbates on surfaces [24].

As a first application, in spectroscopic photoemission experiments combined simultaneously with non-linear optics investigations, changes of the electronic structure during continuous deposition of caesium atoms on a single-crystalline Cu(111) substrate are investigated. By variation of different parameters like the incident photon energy or the growth temperature, we are able to get direct access to information concerning the contributions to the intensity of the observed resonant optical transition and determine which states take part in the previously mentioned resonances. Additionally, calculations based on simple models are performed in order to get better insight into the interesting phenomena of surface state energy shifts.

Next, we probe the changes in the electronic structure during continuous deposition of iron films on Ag(001) substrates. The good control over the experiment allows us to study the formation of specific electronic states near to the Fermi level. By varying the polarization of the incident light we can access the information regarding the symmetry of the investigated states which is used to recognize their character and origin in comparison to the bulk band structure. We analyze the experimental data by use of the "phase accumulation model" (PAM). Additionally, we determine the spin character of the investigated states by means of the spin-resolved photoemission. The angle-resolved photoemission of clean and iron covered silver surfaces allowed the experimental estimation of the effective

mass and the binding energies of the $n = 1$ image potential state which were compared with a PAM prediction.

Finally, time-resolved photoemission investigations aimed at the examination of the lifetime of excited electrons in the unoccupied quantum well states of Co on Cu(001) are presented. The analysis of the interferometric autocorrelation curves by means of phase-averaged envelopes reveals the effect of the electron life time. Further examination by simulation of the cross-correlation curves, allowed an estimation of the electron relaxation time.

This thesis is organized as follows: Chapter 2 describes the physics of the experimental methods used in this work. Chapter 3 contains an overview of the experimental setup and measurement procedures. In chapter 4, the results of the experiments carried out in this work are described. Chapter 5 contains the discussion of the presented results in the scope of quantitative models for the explanation of the measured data and their physical interpretation.

# 2 Basic concepts

## 2.1 Photoemission

### 2.1.1 Energy- and Angle-Resolved Photoelectron Spectroscopy

Photoemission spectroscopy is known to be one of the most direct methods for studying the electronic states of solids, solid surfaces and adsorbate covered surfaces [25–27]. In the general description of the process, after illumination of the sample the emission of electrons with a specific energy and momentum distribution occurs. The photoemission spectra provide information of the initial density of states below the Fermi level of the investigated system, from which photoelectrons are excited into the states above vacuum level. Depending on the incident photon energy we can gain access to core level electrons using soft x rays ($10^2 - 10^3$ eV), and to valence band electrons using UV radiation ($3 - 10^2$ eV). Photoemission spectroscopy has found application to a multiple number of issues like superconductivity [28], metal-isolator transitions [29], the electronic structure of Graphene [30–32], topological isolators [33, 34] and low dimensional systems [35–37]. The external photoelectric effect - photoemission from the surface of a solid placed in vacuum which was observed for the first time by H.G. Hertz in 1888 and explained by Einstein [38] who used Planck's idea of energy quanta to describe it, considers energy transfer from singe photons, to the electrons. The equation below, includes the main thought of this discovery:

$$h\nu = \phi + E_B + E_{kin} \tag{2.1}$$

where $h$ -Plank constant, $\nu$ -photon frequency, $\phi$ -work function of the surface, $E_B$ - electron binding energy, $E_{kin}$ -electron kinetic energy. The meaning of Eqn. 2.1 which describes the energy conservation law, is as follows: each electron absorbs only one photon at a time. If the absorbed energy is large enough to excite the electron it leaves the metal. If is not, the electron dissipates its energy in collisions with nearby electrons and atoms before it can absorb another photon. The theoretical approach to the photoemission process requires a full quantum-mechanical treatment of the complete coherent process in which an electron removed from an occupied state within the solid and excited into a final state above the vacuum level and is detected by the detector. There are two theoretical approaches used to explain the photoemission experiment: the *one step process* and less accurate but simpler approach called *three step model* [26]. In the *three step model* the photoemission process is separated into three independent steps. In the first step an

electron in an initial state after adsorption of a photon is excited into a final state. In the second step the electron is propagating through the material towards the surface. In the third step the electron is emitted from the solid into the vacuum where it can be detected. The separation of above mentioned processes is in principle artificial because above mentioned steps are quantum mechanically not independent. In the so called *one step process* all the above described steps are treated as one step. In this model an electron is directly excited from the ground state in the solid to the final state in which the freely propagating wave in vacuum can decay in to the solid due to scattering [39]. In a simplified description the photoemission current $J$ is a result of single particle photo-induced transitions between occupied ($|\psi_i\rangle$, $E_i$, $\mathbf{k_i}$) and unoccupied ($|\psi_f\rangle$, $E_f$, $\mathbf{k_f}$) states. This single-particle states have an energy difference $E_f - E_i$, corresponding to the incident photon energy $h\nu$. By using the first order perturbation theory, the interaction of the electromagnetic field with the electrons in solid can be described by use of the Fermi golden rule:

$$
\begin{aligned}
J(E_{kin}, k_{||}) \quad &\propto |\langle\psi_f| \hat{V}_I |\psi_i\rangle|^2 \delta(E_f - E_i - h\nu) \\
&= |M_{fi}|^2 \delta(E_f - E_i - h\nu)
\end{aligned}
\tag{2.2}
$$

where $\psi_i$ and $\psi_f$ are the wave functions of the electron in the initial and final state respectively. The matrix element $M_{fi}$ can be written as:

$$
M_{fi} = \langle\psi_f| \hat{V}_I |\psi_i\rangle
\tag{2.3}
$$

The interaction operator $\hat{V}_I$ is given by the quantum mechanical momentum operator for the electron $\mathbf{p}$ and the vector potential $\mathbf{A}$ of the electromagnetic wave:

$$
\hat{V}_I = \frac{e}{mc}[\mathbf{A} \cdot \mathbf{p} + \mathbf{p} \cdot \mathbf{A}] + \frac{e^2}{2mc^2}\mathbf{A} \cdot \mathbf{A}
\tag{2.4}
$$

This interaction operator describes the interaction of the electrons with incident radiation. By assuming that the $\mathbf{p}\cdot\mathbf{A} = 0$ and neglecting the therm $\mathbf{A}\cdot\mathbf{A}$, which represent two-photon process [40–42], above equation can be reduced in dipole approximation:

$$
\hat{V}_I \propto \frac{e}{mc}\mathbf{A_0} \cdot \mathbf{p}
\tag{2.5}
$$

In experiments, photoelectrons can be characterized according to the parallel momentum distribution $p_{||}$ (or wave vector $k_{||} = p_{||}/\hbar$) which can be measured from the angle resolved photoemission spectroscopy (ARPES). ARPES allows to measure and analyse

the solid state band dispersion, giving information about binding energy and effective mass of an electron in the specific electronic state. In the experiment by recording the kinetic energy versus the emission angle $\theta$ we determine band dispersion. The relation between the kinetic energy and the momentum of the electrons outside the sample is defined by Eqn. 2.6.

$$E_{kin} = \frac{p^2}{2m} = \frac{\hbar^2 k_\parallel^2}{2m} + \frac{\hbar^2 k_\perp^2}{2m}. \tag{2.6}$$

Taking into consideration Eqn. 2.6 and the fact that the linear momentum parallel to the surface is conserved as schematically shown in Fig. 2.1, the angle dependence can be converted to $k_\parallel$ by Eqn. 2.7.

$$k_\parallel = \frac{\sqrt{2mE_{kin}}}{\hbar} sin\theta. \tag{2.7}$$

In general the dispersion ($E_{kin}$ versus $k_\parallel$) obtained in the experiment is described by Eqn. 2.8.

$$E_{kin} = E_B + \frac{\hbar^2 k_\parallel^2}{m_{eff}}. \tag{2.8}$$

where $E_B$ is the binding energy and $m_{eff}$ is the effective mass of an electron in a specific electronic band. By fitting the dispersion obtained from experiments with a quadratic function of the form $y = a + bx^2$ we can obtain the parameters $E_B$ and $m_{eff}$ in Eqn. 2.8.
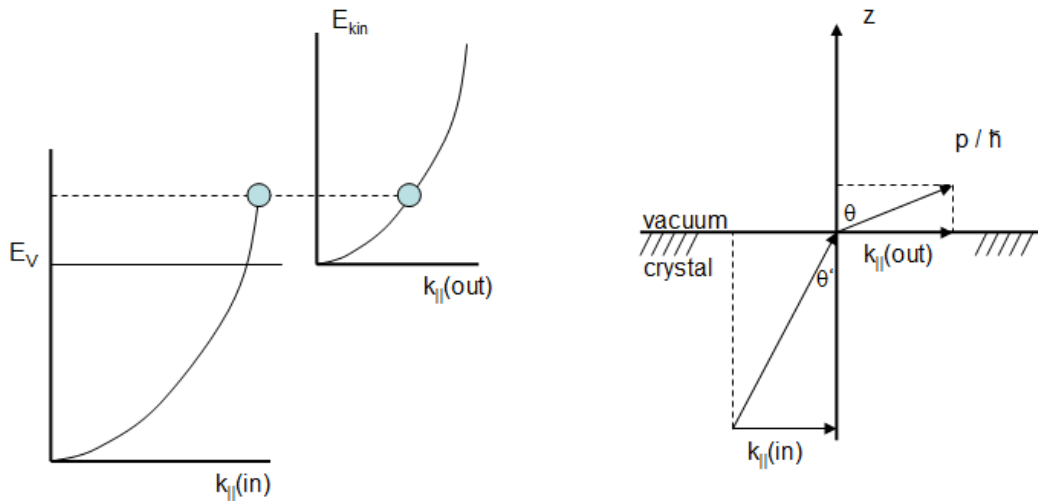


Figure 2.1:   Conservation of linear momentum parallel to the surface

The photoemission as described above does not resolve the perpendicular momentum $k \perp$

due to existence of surface with broken symmetry perpendicular to the film which causes that $k \perp$ is not conserved in this direction. The formation of set of discrete states - quantum well states in a thin film as it will be shown in Sec. 5.2 is giving a possibility to resolve $k \perp$ for those states.

### 2.1.2   Spin-resolved photoemission

To explore magnetic proprieties and phenomena in low dimensional systems, experimental techniques that allow us to investigate the electronic structure with spin resolution are important. The spin-resolved photoemission has developed into a versatile tool for study of surface and thin film magnetism. In this thesis the spin-resolved photoemission, is realised by use of electron spin polarization analyzer described in Sec. 3.4. The spin analysis takes place after energy analyser Fig. 3.1 in Ch. 3 and is based on spin dependent scattering from a ferromagnetic surface. In the electron spin polarization analyzer described in Sec. 3.4, the exchange interaction in the ferromagnetic iron thin film is responsible for spin-dependent cross section in the electron-electron scattering. Spin-dependent reflectivity of a ferromagnetic surface originates from two effects: **first** the elastic scattering between the spin-polarized incident electrons and electrons in ferromagnetic target, **second** the inealastic electron-electron collisions due to the spin-dependent inelastic mean free path (IMFP). To understand the scattering process we consider spin-split band structure in a ferromagnet as shown in Fig. 2.2 a).

Considering the elastic scattering process, the incident electron can penetrate into crystal only if unoccupied states at the specific energy of incident electron are available. For an incident beam with energy in the range between $E_1 - E_2$, as schematically shown in Fig. 2.2 a), electrons whose spin is parallel to minority-spin electrons enter the crystal, while electrons whose spin is parallel to majority-spin electrons are reflected due to lack of available states. The reflectivity shown in Fig. 2.2 b) increases starting from energy $E_1$, for one spin channel and extends up to energy $E_2$. Spin dependent reflectivity in the energy range between $E_1$ and $E_2$ leads to detectable spin-dependent scattering asymmetry as shown in Fig. 2.2 c). Beside the elastic scattering the inelastic electron-electron collisions take a part in the spin dependent scattering process Sec. 3.4 and contribute to spin-resolved photoemission signal. The inelastic mean free path (IMFP) of the electrons depends from material and in case of ferromagnet it is spin-dependent. The density of states of ferromagnetic metal in Fig. 2.3 shows larger number of unoccupied states in which the electron can fall in, more for minority-spin electrons, then for majority-spin electrons. The spin-dependent density of states above the Fermi energy for the two spin directions results in a spin-dependent inelastic mean free path (IMFP). The minority electrons in
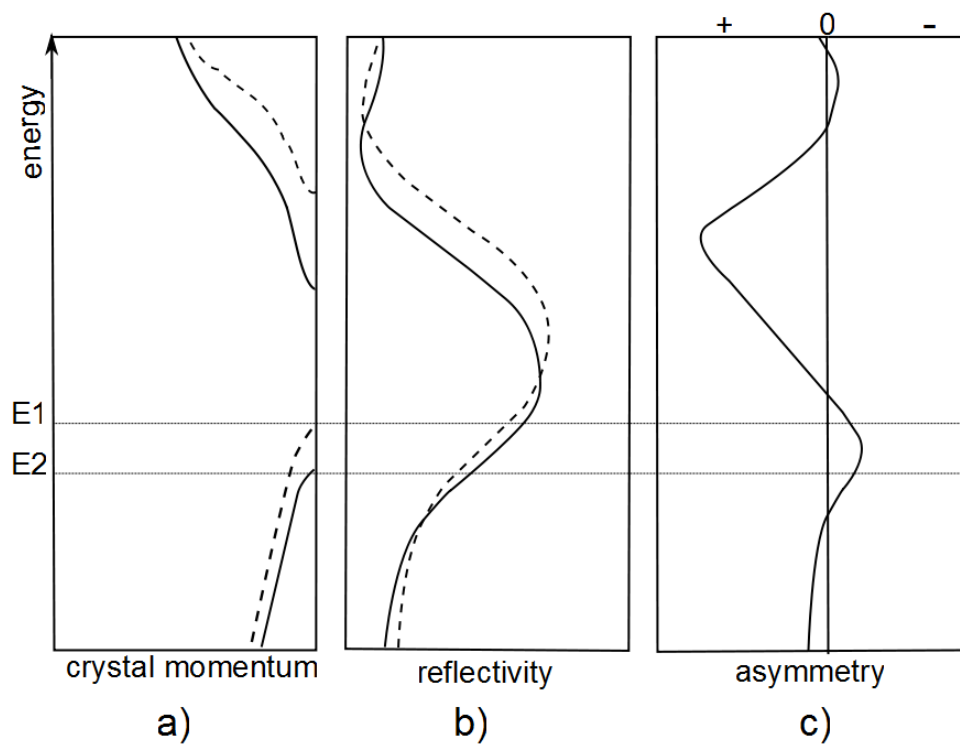
Figure 2.2:   Schematic of spin-dependent reflectivity and asymmetry in electron scattering from spin-split band structure.

Fig. 2.3 are scattered more effectively than the majority electrons and consequently the reflectivity for the majority electrons is higher. In the spin detector described in Sec. 3.4 both, the inelastically and elastically scattered electrons are included in the spin analysis [43].
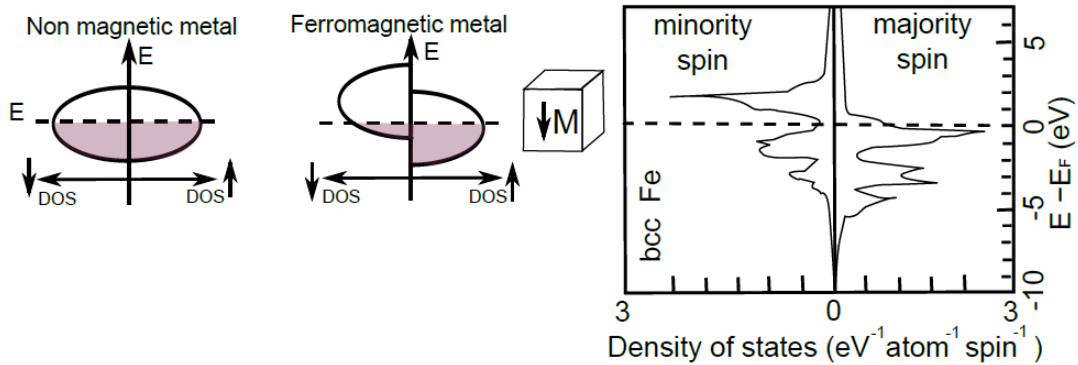


Figure 2.3:   Density of states in ferromagnetic bulk iron, adapted from Ref. [44]

### 2.1.3   Nonlinear photoemission

The possibility that processes in which not only a single photon, but at the same time two or more quanta are exchanged, was described by M. Goeppert-Mayer [45, 46] in 1930. The so called multiphoton-processes are known to be less probable processes which require high radiation intensities. The invention of lasers, which provides coherent short pulses of light with high intensity, makes it possible to experimentally observe multiphoton processes. The first measurements of nonlinear photoemission were reported by Teich [47]. Since the development of the femtosecond lasers in the 1980, the time scale of chemical reactions between 10 fs and 10 ps become accessible for experimental investigations [48]. Nowadays the development of lasers systems allows to shorten the laser pulses to few optical cycles [49]. With progress in the field of nonlinear optics even shorter attosecond $(10^{-18}\,\mathrm{s})$ pulses can be soon applied in the photoemission spectroscopy for study of the fundamental physics of the electron dynamics in atoms and solids [50]. Thanks to the strong femtosecond pulses in the THz frequency range the direct coherent control over magnetic excitations became possible [51].

In nonlinear photoemission process the coupling due to the ultra-short, high-intensity optical pulses between occupied initial states, the initially unoccupied intermediate states and the final states plays a decisive role. Implementation of a controllable time delay between laser pulses allows investigation of the temporal behaviour of the excited system as discussed in Sec. 2.1.4. The investigations of image potential states on the metal surfaces

are a good example with use of nonlinear photoemission. The clear physical mechanism of formation [52] and relative long lifetimes of those states make them an important model systems for electron dynamics investigations at magnetic and non-magnetic solid surfaces [53–58].

The graphical presentation of the multi-photon photoemission process is schematically shown in Fig. 2.4. It includes the linear one photon process, the nonlinear two- and three-photon photoemission processes.
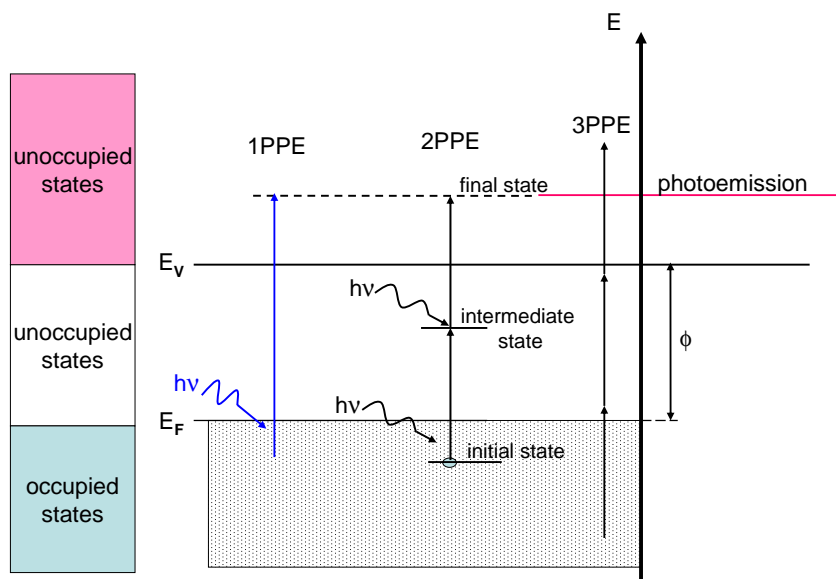


Figure 2.4:   The schematic of the multi-photon photoemission process.

The one photon photoemission described by Eqn. 2.1 and shown in Fig. 2.4 is a first order, linear process in which an electron with a binding energy $E_B$ after absorption of a photon $h\nu$ is excited above vacuum level $E_V$ with detectable non-zero kinetic energy $E_{kin}$. The two-photon photoemission is a second order, non-linear process Fig. 2.4 in which within one laser pulse the electron absorbs one-photon and it is excited into an unoccupied state between $E_F$ and $E_V$, where after adsorption of another photon, the electron is emitted above the vacuum level. The number of photoelectrons emitted in a 2PPE process is proportional to square of incoming light intensity. The simplest description of the 2PPE process is given by Eqn. 2.9 which is a modification of Eqn. 2.1:

$$2h\nu = \phi + E_B + E_K. \tag{2.9}$$

The higher order photoemission processes involve more transition steps until the electron emission occurs. To describe them the Eqn. 2.1 is modified dependent on the number of transition steps similarly as in the 2PPE for 2 step process Eqn. 2.9. Thanks to the energy and the parallel momentum conservation, described in more detail in the previous section, the multiphoton photoemission provides a unique method to study the unoccupied electronic band structure.

In strong contrast to the linear one-photon photoemission, in the multi-photon photoemission process, the intermediate states play a decisive role. Moreover, the optical excitation with short laser pulses enable the possibility of time-resolved studies of the electron dynamics in an originally unoccupied electronic state. We can observe there many interesting dynamic phenomena. The description of the above processes concerning the propagation of quantum-mechanical system is generally formulated by a density matrix formalism [59–62]. With the use of density matrix formalism it is possible to take into account the coupling between the electronic states and the optical excitation field as well as the time-dependent interactions within the system [55, 63–68]. A semiclassical approach is applied to describe the photoemission, in which the electronic states are described quantum mechanically but the radiation is considered as a classical electric field.

A basic model of the 2PPE process is based on the density matrix formalism. Lets consider a system composed of three orthonormal states: the initial state $|i\rangle$, the intermediate state $|m\rangle$ and the final state $|f\rangle$ with corresponding energies $\epsilon_i$, $\epsilon_m$, $\epsilon_f$ respectively. The density matrix operator $\hat{\rho}$ of above described system can be expressed as:

$$\hat{\rho} = \begin{pmatrix} \rho_{ii} & |i\rangle\langle i| & \rho_{im} & |i\rangle\langle m| & \rho_{if} & |i\rangle\langle f| \\ \rho_{mi} & |m\rangle\langle i| & \rho_{mm} & |m\rangle\langle m| & \rho_{mf} & |m\rangle\langle f| \\ \rho_{fi} & |f\rangle\langle i| & \rho_{fm} & |f\rangle\langle m| & \rho_{ff} & |f\rangle\langle f| \end{pmatrix} \tag{2.10}$$

$$\rho_{ii}(t = -\infty) = 1$$

The diagonal elements in form of $(\rho_{aa})$ in the matrix $\hat{\rho}$, describe the populations of the involved states, while the off-diagonal elements in form of $(\rho_{ab})$, represent the coherences between the states [59]. An application to the three-photon photoemission (3PPE) process is presented in [69]. The matrix element $\rho_{ii}$ is the only non-zero element in the ground state at time $t = -\infty$, representing the initial population of the relevant state. The photoelectrons $N(\epsilon_f)$observed in the experiment for a given energy of the final state are

described in the density matrix formalism as:

$$N(E_f) = \int_{-\infty}^{+\infty} dt \, \mathrm{Tr}\{\hat{F}\hat{\rho}(t, E_f)\} \tag{2.11}$$

where $\hat{F}$ is an operator defined simply as $\hat{F} = |f\rangle \langle f|$ in order to receive the population in final state $\rho_{ff}$. The matrix element $\rho_{ff}$ determines the quantity we measure in experiment: the very small population that is transferred to the final state by ultra-short optical pulse. Starting at $t = -\infty$ in the Eqn. 2.11 from initial state $\rho_{ii}$, the coupling provided by the laser electric field $E(t)$ via intermediate state allows to develop a finite values in the matrix elements during time evolution of density operator. This time evolution is described by the equation of motion for the density matrix (Liouville - von Neumann equation) [55, 60, 64, 65, 67]:

$$\frac{d\rho_{ab}}{dt} = -\frac{i}{\hbar} \langle a| \left[\hat{H}_S + \hat{V}_I, \hat{\rho}\right] |b\rangle - \Gamma_{ab}\rho_{ab}(a, b = i, m, f) \tag{2.12}$$

where $\hat{H}_S$ is the hamiltonian of unperturbed system, $\hat{V}_I$ is the interaction operator describing the coupling between relevant states. The dipole approximation of $\hat{V}_I$ discussed in Sec. 2.1.1, leads to a dipole matrix element $\mu_{ab}$ which describes the relative strength of coupling between states $|a\rangle$ and $|b\rangle$. The complete description of the time dependent response of the system under influence of an electric field from optical pulse is given in Ref. [70]. The elements $\Gamma_{ab}$ in Eqn. 2.12 are phenomenological parameters which are introduced to account for the relaxation of the system back to equilibrium. In a simplified picture those elements are assumed to be constant. The off-diagonal elements $\rho_{ab}$ decay due to the influence of the population loss of the population loss rates $\Gamma_{aa}$, $\Gamma_{bb}$ of both involved levels and in addition due to the dephasing $\Gamma_{ab}$ between states $|a\rangle$ and $|b\rangle$. In general the coherences $\rho_{ab}$ accounting for interference effects will be washed out when the phase correlation of the oscillating dipole between the interactions with electric field, decays to zero [69]. The perturbative expansion of the $\hat{\rho}$ with respect to interactions with electric field allows for a transparent physical interpretation. Such a perturbative expansion allows us to visualise the induction of non-zero matrix elements $\rho_{ab}$ as a sequence of steps in which the commutators $\left[\hat{H}_S + \hat{V}_I, \hat{\rho}\right]$ in Eqn. 2.12 are expanded up to a specified order [71]. This expansion can be represented by double-sided Feynman diagrams which keep track of both time development of the populations in the involved states as well as the induced coherency between those states [69]. Another related visualisation (Liouville space pathways described in [69]) allows us to show the possible coupling of two generic elements $\rho_{ab}$ and $\rho_{cd}$ of the density matrix.

The electronic structures in band structures in real solids can be approximated by the

three level system only in rare cases. A generalisation of band alike states [72], can be made by introduction of **k** dependent three or more level systems. In such systems the coupling between states by various $E$ and **k** elastic and inelastic scattering processes must be additionally considered. This is the reason responsible for an extreme complexity of the $ab-initio$ calculations of the non-linear photoemission.

The above description does not take into account the spin influence on the discussed states which can affect the spin dependent interaction operator $\hat{V}_I$, spin dependent matrix elements $\langle a| V_I |b\rangle$ or spin dependent scattering processes. In general, a coupling between spins must be considered since the existence of the spin-flip scattering processes [73, 74]. Additionally the occupation of a state $|a\rangle$ through an inelastically spin dependent scattering process from another state $|b\rangle$ is possible. This allows the dynamics of populations with different spin to be coupled together in a complex way, and introduces a need of a proper theoretical description.

### 2.1.4   Time-resolved photoemission

Interferometric time-resolved two-photon photoemission (ITR-2PPE) is a suitable non-linear optical method for probing phase and energy relaxation of excited electrons [56, 75–77]. By means of the ITR-2PPE spectroscopy it is possible to measure with extremely high (about 1fs) resolution the carrier dynamics processes [75]. In the interferometric photoemission two pulses with identical polarization and frequency $\omega$ are collinearly overlapped on the sample and the photoemission signal is recorded as function of the pump-probe delay. As electrons are excited, the pump pulse induces on the sample linear and nonlinear polarization at laser frequency and its second harmonic, which decays into an incoherent non-equilibrium distribution of hot electrons [78]. The linear polarization due to coupling of the initial state $E_0$ with the intermediate state $E_1$ and with the final state $E_2$, oscillates at the excitation frequency $\omega$, while the nonlinear polarization between the initial $E_0$ and the final state $E_2$, oscillates at frequency $2\omega$. The probe pulse interacts coherently with the induced polarization and incoherently with the hot electron population. The interaction of the probe pulse with the pump pulse excitation can occur in three different ways as illustrated in Fig. 2.5.

In Fig. 2.5 a) an excited electron adsorbs another photon and if its total energy is higher than the vacuum level, the electron can be detected at a given kinetic energy. This process gives information about the energy relaxation time of the intermediate state, $T_1$. In the Fig. 2.5 b) depending on the relative phase between the pump and the probe pulse an interference of linear polarization results in enhanced adsorption or simulated emission. The oscillation of polarization with frequency $\omega$ between the states $E_0$ and $E_1$, and be-
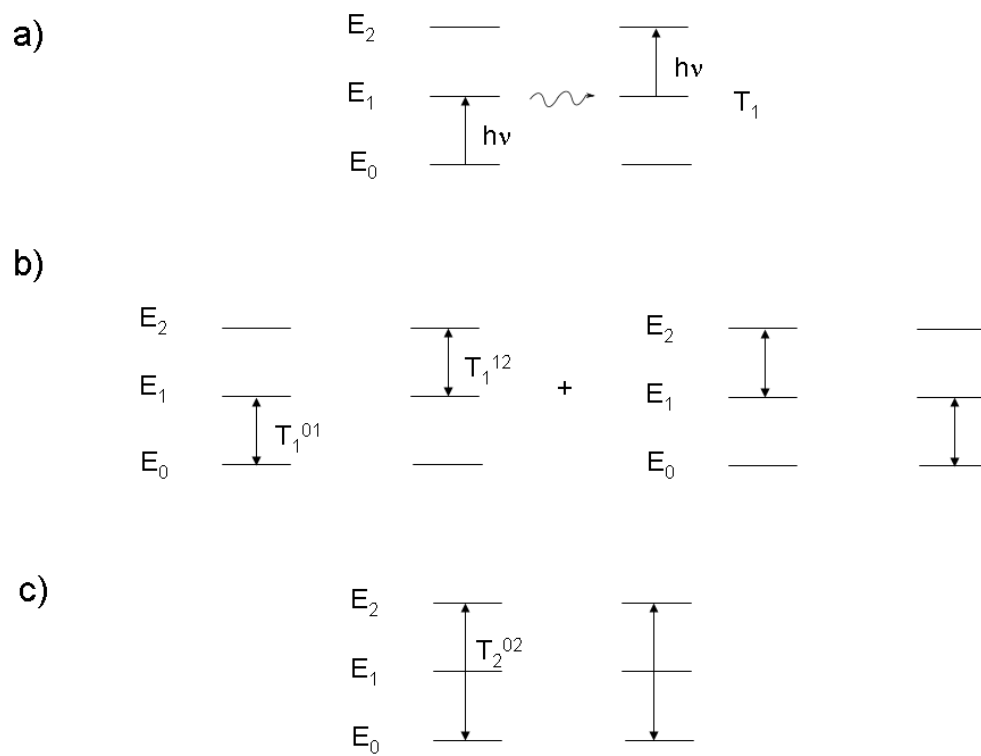
Figure 2.5:   Schematic of two-photon photo-excitation processes by coherent laser pulses. a) energy relaxation time $T_1$, b) phase relaxation time $T_2^{01}$ and $T_2^{12}$, c) dephasing of nonlinear polarization $T_2^{02}$ [79]

.

tween $E_1$ and $E_2$, decays with the phase relaxation time $T_2^{01}$ and $T_2^{12}$ respectively as shown in Fig. 2.5 b). The two pulse excitation induces the nonlinear polarization Fig. 2.5 c) between the $E_0$ and the $E_2$ states, which decays with a time constant $T_2^{02}$. The ITR-2PPE signal can be decomposed approximately by Fourier analysis into components consisting of: a slowly varying phase-averaged envelope of equal pulse correlation measurement denoted as $0\omega$, - envelopes of the fast oscillations at approximately the excitation frequency denoted as $1\omega$, - its second harmonic denoted as $2\omega$. This decomposition allows to determine the hot electron lifetimes $T_1$ from $0\omega$ envelope, to estimate the phase relaxation times $T_2^{01}$, $T_2^{12}$ of the linear polarization from $1\omega$ envelope and dephasing time $T_2^{02}$ of the nonlinear polarization from $2\omega$ envelope. The figure Fig. 2.6 shows an example of time-resolved two-photon autocorrelation spectrum from Cu(001) and its decomposition into mentioned above $0\omega$, $1\omega$, $2\omega$ components:
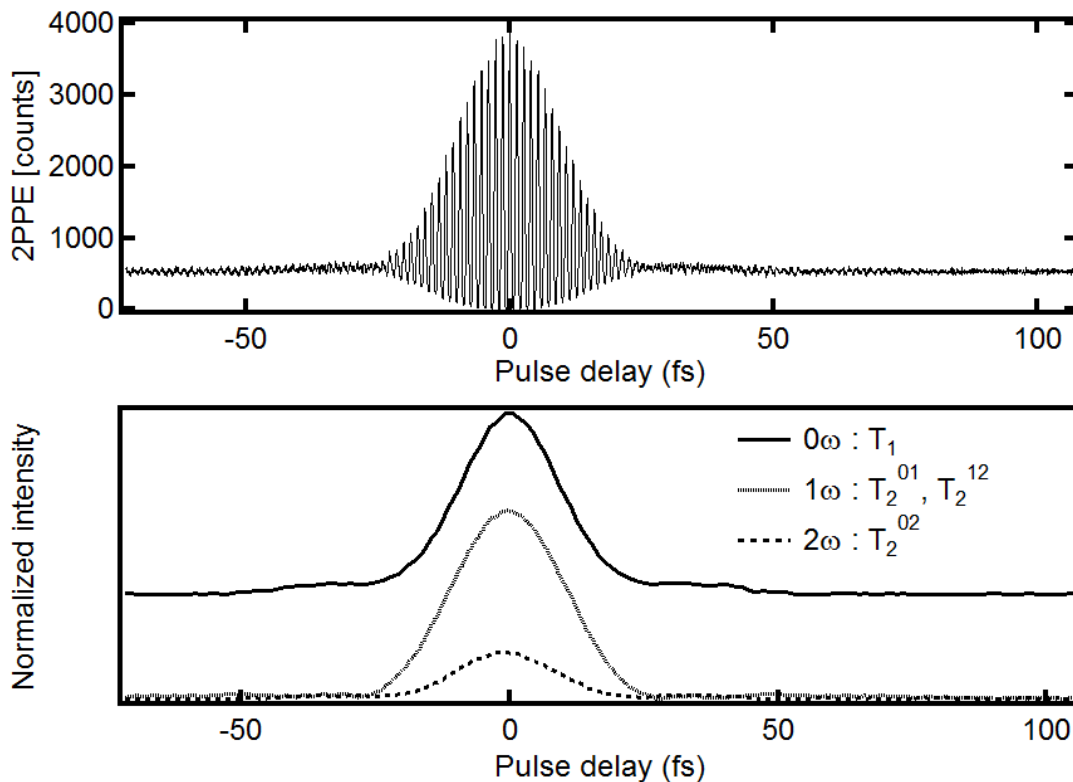


Figure 2.6:  Interferometric time-resolved two-photon correlation curve from Cu(001) and its decomposition into $0\omega$, $1\omega$ and $2\omega$ envelopes.

## 2.2  Second harmonic generation

The physics of nonlinear optics started with the invention of the laser by Maiman in 1960. Access to very high light intensities made it clear that the response of a medium to

light can be nonlinear. This discovery led to development of researches regarding various intriguing phenomena such as second harmonic generation. To understand the physics of SHG process one can consider a light with incident field $E$ at frequency $\omega$. This light can induce a dipole oscillation of each molecule in the medium. The nature of this oscillation is anharmonic and has higher order frequencies $2\omega, 3\omega$ and so on. Oscillating dipoles emit radiation from the medium and because of anharmonic character, one expects the output radiation at higher frequencies [80]. The surface second harmonic generation process is based on the fact that the inversion symmetry at the interface of a medium is broken[61, 80, 81]. The incident electric field $E_\perp$ of a laser light oscillating in a direction normal to the surface is interacting with surface charge $\sigma$ expressed by Eqn. 2.13. It is distributed in a thin region close to the surface of a conductor.

$$\sigma = -e \cdot \int dz \delta n(z). \tag{2.13}$$

The incident light electric field induces time-dependent perturbation and draws the electrons from the metal to a region in distance $d$ from surface where they accumulate with a certain distribution $\delta n(z)$. This give a rise to a linear surface polarization $P_\perp = \sigma d$ as shown in Fig. 2.7 a).

A stronger field produces a larger surface charge and deforms its distribution as shown in Fig. 2.7 b), displacing it by a distance $\Delta d$ and giving rise to extra surface polarization $P_\perp^{(2)} = \sigma \Delta d$. When the fundamental field reverses direction after half of period the electrons are strongly pushed onto the surface instead of being strongly pulled. The extra surface polarization $P^{(2)}$ which arises from deformed charge distribution responds nonlinearly to the field reversion and oscillates in case of second harmonic with frequency $2\omega$ as expressed by Eqn. 2.14.

$$P^{(2)}(2\omega) = \chi^2 E(\omega)E(\omega). \tag{2.14}$$

where $\chi^2$ is known as the nonlinear susceptibility, a characteristic coefficient of the medium. The induced $P^{(2)}$ polarization according to Maxwell's equations radiates an optical field $E^{(2)}$ at optical frequency $2\omega$. The polarization $\vec{P}$ can be expressed also in the scope of density matrix formalism as $\vec{P} = \text{Tr}[\hat{\mu}\hat{\rho}]$. The relevant elements of density matrix type $|b\rangle \langle a|$ possess the non-diagonal elements describing the non-linear optics phenomena[60]. There is an advantage of the density matrix formalism, namely that the both the photo-emission and the non-linear optical signal from the observed system can be described in a unified picture with the use of common parameters [60, 82]. Combined
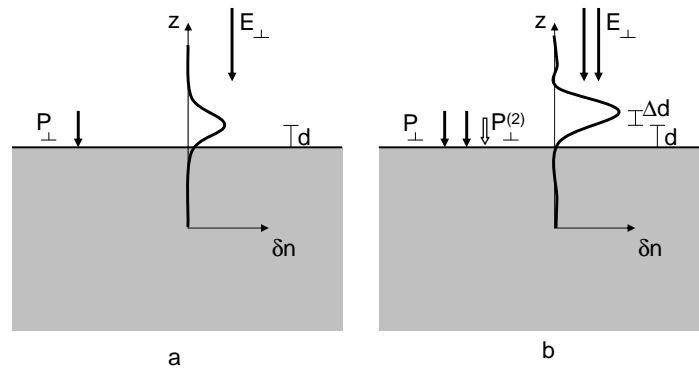
Figure 2.7: The schematic of induced surface a) linear dipole per unit volume, b) second-harmonic dipole per unit volume.

experiments with use of photoemission and non-linear optics can provide an additional information as it is shown in the further part of this thesis.

The second harmonic generation as a technique is a powerful instrument in surface analysis due to its high surface sensitivity and applicability which allows to use it where the electron spectroscopy can not be applied. SHG in comparison the angle resolved photoemission can not obtain the information about the relevant initial and final state energies or the momentum of an electron. The only information which is known are the photon energies of optical transitions and the output intensity of frequency doubled light.

# 3 Experimental setup

The experimental results presented in this thesis, were obtained with an apparatus as shown on Fig. 3.1. The laser light source produces 12fs, 800nm pulses which are then frequency doubled (400nm) and used in photoemission investigations. The Mach-Zehnder interferometer control pump probe delay used in time-resolved photoemission. Photoelectrons emitted from sample are analysed both by the electron energy analyser and the electron spin polarization analyser. Light reflected from the sample is investigated by surface second harmonic generation detector. Sample is prepared and held in ultra high vacuum (UHV) condition. The main elements in Fig. 3.1 are described in detail in the following sections.
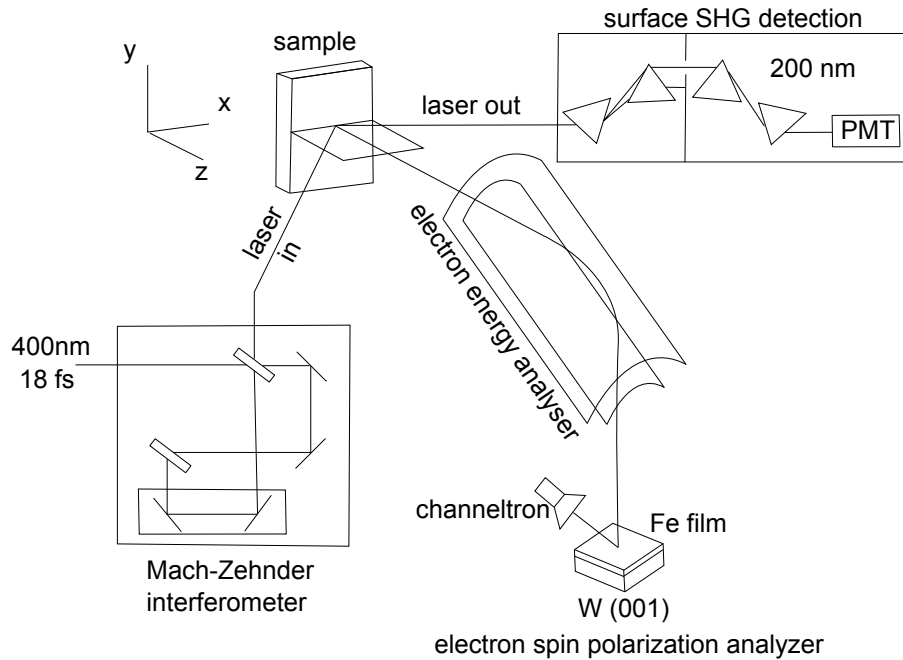


Figure 3.1: Experimental setup for interferometric control of spin polarized electron populations in multiphoton photoemission [83].

## 3.1 Laser system

The light source used in the experiment ("Fusion" laser from Femto Optics) is a Ti:sapphire oscillator as shown in Fig. 3.2, pumped by a 6W, 532nm CW "Finesse" laser from Laser Quantum. The green light from "Finesse" pump laser is directed by a piezo-controlled mirror into the lens L showed in Fig. 3.2, which focuses the light on the
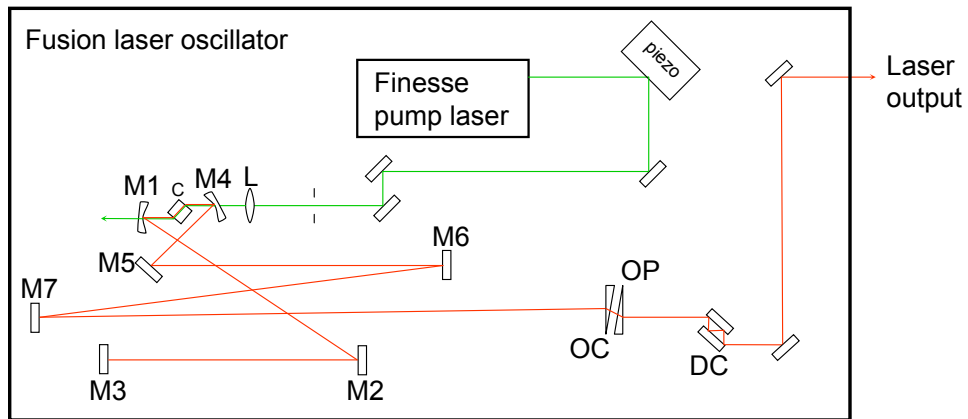
Figure 3.2:   Fusion oscillator: Optical Schematic. M1-M6 dielectric mirrors, L - lens, DC - dispersion compensation mirrors, OC - output coupler. OP - compensation plate

Ti:sapphire crystal. Ti:Sa crystal as gain medium emits in the process of spontaneous emission near infra red light which is trapped in the cavity with a short (M1 to M3) and a long arm (M5 to M7 then OC). After the output coupler (OC) the beam is directed towards a pair of mirrors (DC) with special coating for dispersion compensation. The mode-lock operation can be started by moving the M3 end mirror, which in process of
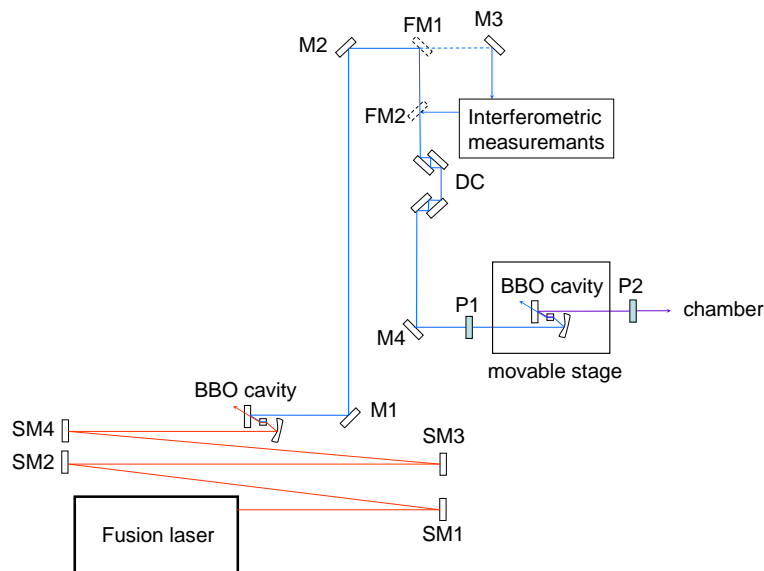


Figure 3.3:   The optical setup guiding the laser beam into the photoemission chamber. S1 - S4 silver mirrors, M1 - M4 dielectric mirrors, FM1 - FM2 flippable dielectric mirrors, DC - dispersion compensation mirrors, P1 - P2 polarizer

constructive interference, creates periodical pulses of light with femtosecond duration time. The 800 nm pulsed light from fusion laser is directed through set of silver mirrors SM1 - SM2 - SM3 - SM4 as shown in Fig. 3.3 to a Beta Barium Borate (BBO) crystal cavity where in the second harmonic generation process, 400 nm light is produced. The 400 nm UV light is then directed by set of dielectric mirrors M1 - M2 - M2 - FM1 through the DC mirrors for dispersion compensation and the P1 polarizer to the chamber. By switching between flip mirrors FM1, FM2 we are able to provide interferometric measurements described in one of next subsections. The second BBO cavity in the movable stage doubles frequency to 200 nm light used in one photon photoemission (1PPE) measurements.

## 3.2   Surface second harmonic generation setup

In Fig. 3.1 the light is reflected from the sample surface towards the surface second harmonic generation detector. Together with the reflected light there is second harmonic light generated at the surface of the sample. Both the reflected 400 nm and the generated 200 nm light from the sample, enter the detector as shown in Fig. 3.4. The L1 and L2 lenses focus the beam, which is guided by the silver mirrors SM1 - SM2, on the Brewster CaF2 prism P1. The P1 prism separates the main 400 nm beam from the generated second harmonic 200 nm light. After passing the iris i2 on which part of the remaining 400 nm
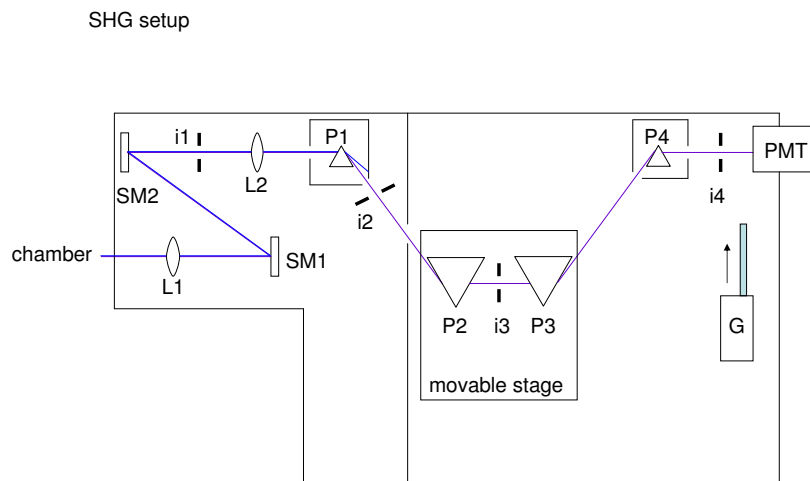


Figure 3.4:   Schematics of second harmonic generation detector. L1 - L2 lenses, SM1-SM2 silver mirrors, i1-i4 irises, P1 - P4 prisms, G - glass filter, PMT - photomultiplier tube

light is stopped, the 200 nm light goes through prism P2 and P3. Finally the 200 nm light goes through the last P4 prism to the PMT -photomultiplier tube. The movable glass filter is used to check the signal to background ratio. The 200 nm light will be absorbed whereas the stray light from the surrounding is allowed through. The detected intensity ratio of 200 nm light to background light is better then $10^4$.

## 3.3 Interferometric measurements

The time-resolved photoemission investigations are based on the pump-probe delay control provided by a Mach-Zehnder interferometer shown in Fig. 3.6. The 400 nm light enters the interferometer from the mirror M1 side and is split into two beams by BS1 and BS2 beam splitters. The delay stage shown in Fig. 3.6, allows the optical path adjustment and the fine tuning T of the pulse overlap in the time domain. The time delay between the two beams, provided by the delay stage, is achieved during the light propagation through two different optical paths. One output beam reflected from the flipped mirror FM2 is directed through dispersion compensation mirrors to the chamber. The other output beam, reflected from mirror M2, is directed through the lens L, to the grating G. It is finally measured by a photodiode PD as a reference. The reference output beam serves as a monitor and control mechanism of the delay between the pulses.
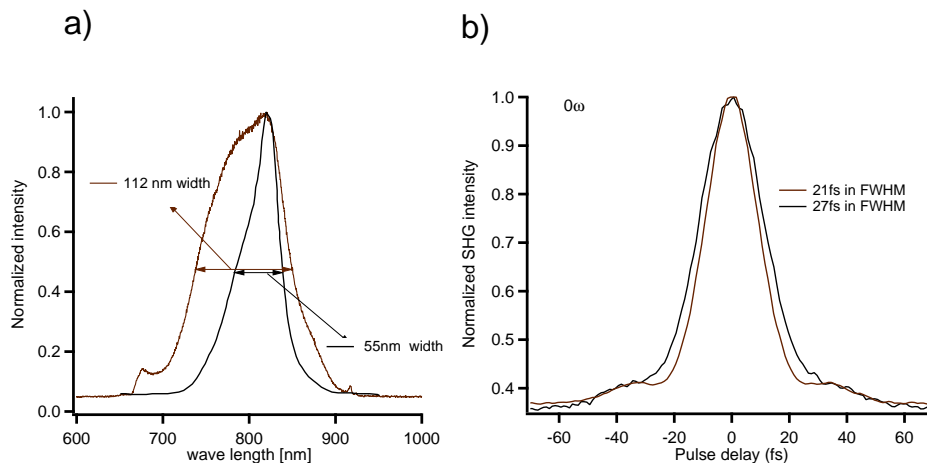


Figure 3.5:   a) Laser mode-lock spectra obtained by fine adjustment of the cavity, b) corresponding change in the pulse shape measured by the phase-averaged autocorrelation ($0\omega$ envelope). FWHM - full width at half maximum.

As it is shown in the Fig. 3.5 a) we have a possibility to manipulate the shape of our laser mode-lock spectrum. This however has a direct impact on the laser pulse. In the figure Fig. 3.5 b) we clearly see the influence of changed mode-lock spectrum on the phase averaged autocorrelation envelope at FWHM and in general on the shape of the envelope.
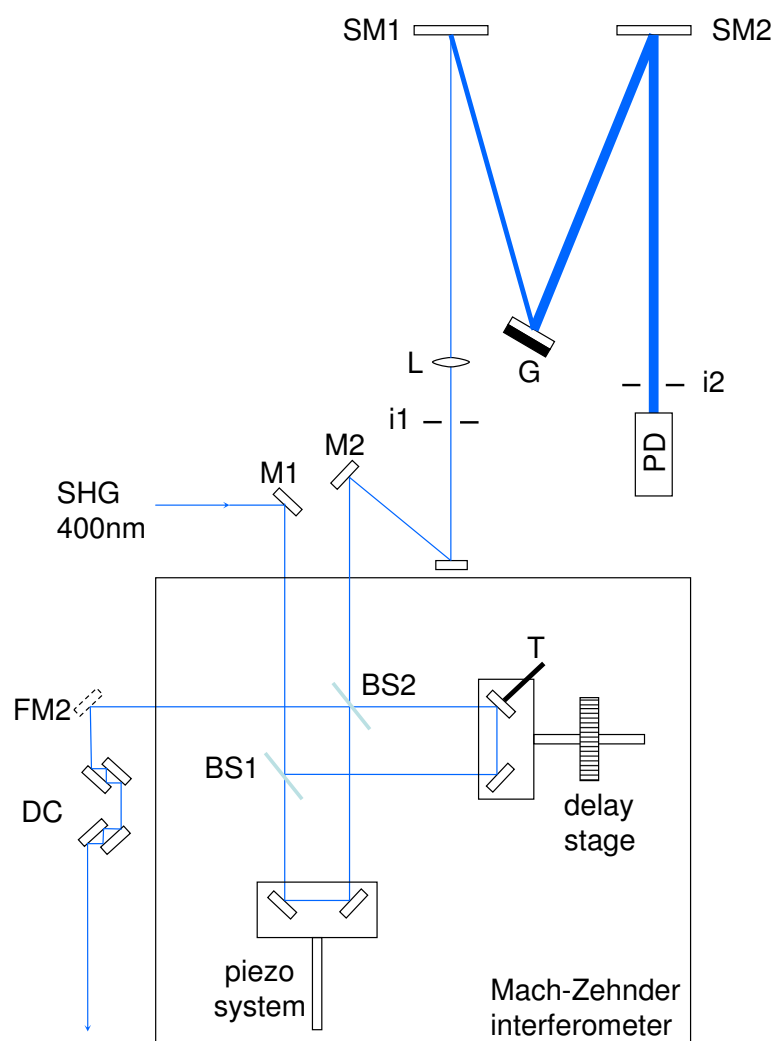
Figure 3.6:   Mach-Zehnder interferometer. DC - dispersion compensation mirrors, FM2 - flippable dielectric mirror, M1 - M2 dielectric mirrors, BS1 - BS2 beam splitters, L - lens, i1 - i2 irises, G - grating, PD - photodiode, T - fine tuning controller

The previously mentioned changes in the laser pulse are directly connected with changes in the envelope shape. The manipulation of the mode-lock spectrum can be used in experiments in order to obtain an advantage of a control over the laser pulse conditions. Ultra short 10 fs laser pulses are known to be affected by quantities like group delay

dispersion (GDD) and third order dispersion (TOD). The analysis of GDD and TOD, will be discussed later together with the lifetime measurements of the unoccupied quantum well state.

## 3.4   Electron spin polarization analyzer

Devices with spin sensitivity used in spin-resolved photoemission experiments are based on spin-dependent scattering of electrons. The physical basis for the spin-dependent scattering are spin-orbit and exchange-splitting interaction [43, 84, 85]. The electron spin analyser presented in Fig. 3.7 exploits the exchange interaction phenomena [43]. The main part of the detector is the iron film about $\approx 40\,\mathrm{ML}$ thick on W(001) with chemisorbed oxygen. The presence of spin dependent band gap in the iron film causes the spin-dependent reflectivity, namely the reflectivity depends on the relative orientation between the electron spin and the magnetization of the iron film. The chemisorbed oxygen on the top of the film is preventing from residual gas adsorption. In the basic setup of our spin detector the electron beam is focused on the W(001) scattering target which is surrounded by an electromagnet M. After reflection from the Fe film on W(001) the electrons are collected by the channeltron Ch B. The spin asymmetry is measured with alternating Fe film magnetization using the electromagnet M. The projection of the spin quantization axis onto the magnetization direction can be chosen by the rotation of the holder H. In the 'evaporation position' the holder H points toward the Fe source rod. In this position the 2PPE measurements without spin-resolution are performed by detecting the photoelectrons with the channeltron Ch D.

The switching between two opposite magnetization directions of the iron film allows to measure the number of reflected spin-up and spin-down electrons $I_{-M}, I_{+M}$, which are used to derive the asymmetry $A$, defined as $A = (I_{+M} - I_{-M})/(I_{+M} + I_{-M})$. The asymmetry is proportional to the spin-polarization of the incident electron beam $P$ by $P = A/S$. The constant $S$ (Sherman function) depends strongly on the incident electron kinetic energy and the scattering potential on the Fe film target, therefore it is necessary to calibrate the Sherman function by using a known spin-polarized electron beam. The value of $S$ corresponds to the reflected intensity asymmetry ($A$) upon magnetization reversal of the iron film when a completely spin-polarized electron beam is analysed ($P = 1$). The Sherman function was estimated to $0.24 \pm 0.03$, as calibrated in [43]. The projection of the spin-polarization ($P$) along the magnetization direction of the iron film (along $+M$) can be obtained by:

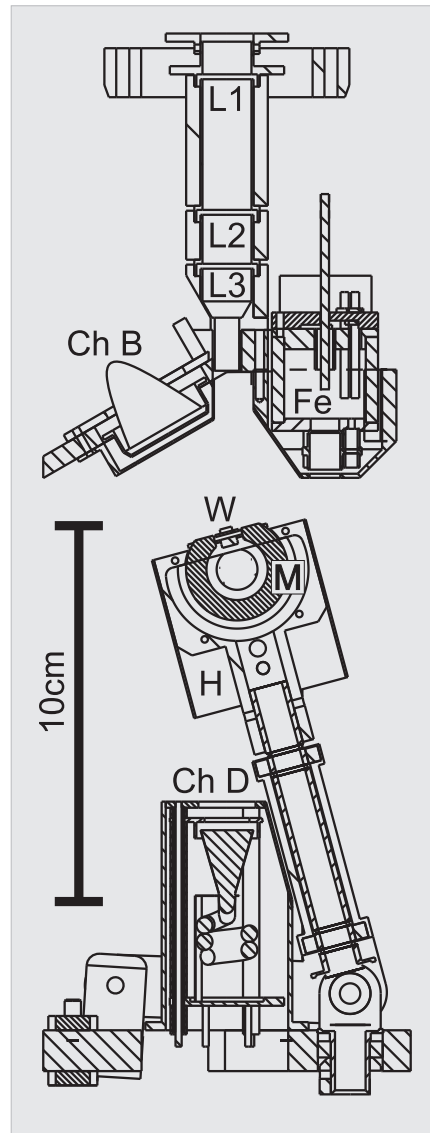$$P = \frac{1}{S}\frac{I_{+M} - I_{-M}}{I_{+M} + I_{-M}}. \tag{3.1}$$

Figure 3.7: Drawing of main parts of the electron spin polarization analyzer (taken from [43]): (L1,L2,L3) electrostatic transfer and focussing lenses, (W) W(001) crystal, (M) electromagnet, (H) rotatable holder for W, M and heating filament, (Ch B) the channeltron collecting the electrons reflected from W, (Ch D) the channeltron which is used for spin-integrated measurements when H is moved into the position under the Fe evaporation source (Fe).

The spin-up and spin-down intensities ($I_{\pm s}$) are derived from the total number of measured electrons [86] and the spin-polarization is :

$$I_{\pm s} = \frac{(1 \pm P)}{2}(I_{+M} + I_{-M}).\qquad(3.2)$$

The method of switching between the $\pm M$ magnetization of the iron film inside the spin-detector during experiments allows significant reduction of the extrinsic error which may come from the laser intensity fluctuation [43]. The experimental error is obtained by taking into account the statistical error of counting electrons, which is the standard deviation in Poisson statistics defined as the square root of the measured number of electrons [86]. The error indicated in the spin-polarization as well as in the partial spectra are derived by error propagation.

In the experimental results shown in this thesis the photoelectron spin is analyzed in the direction along the sample magnetization. The spin-up (-down) photoelectrons are defined to have their spin with component $-\hbar/2$ ($+\hbar/2$) along the quantization direction which is parallel to sample magnetization. The electrons in the sample are called majority (minority) electrons if they have spin component $-\hbar/2$ ($+\hbar/2$) along the sample magnetization.

## 3.5   Sample preparation

All substrates were cleaned by cycles of argon ion bombardment at ($2\,\mathrm{keV}$, $2\times10^{-8}\,\mathrm{mbar}$) followed by 10 minutes annealing at $700\,\mathrm{K}$ for Ag(001) or $900\,\mathrm{K}$ for Cu(001) and Cu(111). The surface quality was verified by Auger electron spectroscopy, the low-energy-electron diffraction (LEED) and the nonlinear photoemission signal coming from the surface states [87]. The experiments were performed at a base pressure of $2\times10^{-10}\,\mathrm{mbar}$. The samples were cooled in the process of heat exchange through contact with the manipulator cooled with liquid nitrogen flow. The thin films: Cs on Cu(111), Fe on Ag(001) and Co on Cu(001) investigated in the frame of this thesis are prepared as described below:

**Cs on Cu(111).**   The Cs was deposited from a current-heated getter source (SAES Getters, www.saesgetters.com) at a pressure of $5\times10^{-10}\,\mathrm{mbar}$. Cs was deposited on the Cu(111) surface at $140\,\mathrm{K}$ or alternatively at $300\,\mathrm{K}$. The Cs coverage was estimated on the resulting work function change induced by Cs adsorption [88].

**Fe on Ag(001).**   Iron films were deposited on Ag(001) single crystal by an electron beam evaporator at pressures of $5\times10^{-10}\,\mathrm{mbar}$. The iron film thickness was estimated

by medium energy electron diffraction (MEED). The deposition in case of continuous measurement during film growth was done at 140 K in order to avoid silver segregation. The image potential state dispersion measurements where performed on the film whose growth was optimized [89]. To avoid silver segregation the first 10 ML of the film were evaporated at 140K, the last 10 ML where deposited at 570K in order to take advantage of a good homoepitaxial growth. The oxidation process was performed with the pressure of $1.5 \times 10^{-8}$ mbar for 10 minutes. Then the sample was annealed at 570 K for 5 minutes. The amount of oxygen was estimated as: 100 seconds exposure at $1.33 \times 10^{-8}$ mbar is equal to one Langmuir.

**Co on Cu(001).** Cobalt was deposited on Cu(001) single crystal by an electron beam evaporator at pressure $2 \times 10^{-9}$ mbar. The Co film was deposited in 300 K and in 140 K. The averaged 2PPE signal during film growth shows oscillations of one monolayer period [90], used for film thickness calibration. At the desired film thickness, the deposition was stopped and the film was cooled down to 140 K for the photoemission measurements.

# 4 Results

This chapter contains the results of Cs on Cu(111), Fe on Ag(001) and Co on Cu(001) studies. The measurements presented in the following subsections are obtained by one and two-photon photoemission, second harmonic generation and time- and angle-resolved techniques. The simultaneous use of combined photoemission and surface second harmonic generation allows more precise insight into the investigated systems. The $p-$ and $s-$ polarised light and the electron spin-polarization analyzer provides useful information about the symmetry and spin-polarization of probed electronic states.

## 4.1 Second harmonic generation and two-photon photoemission from Cs/Cu(111)

The two-photon photoemission spectrum (2PPE) from the clean Cu(111) in Fig. 4.1 a) shows two peak features. The work function gives rise to a cut off which is located at around 1.8 eV on the intermediate state energy scale. The first (1.9 eV) peak on intermediate energy scale comes from the bulk transitions near the L-points in the band structure [91]. The second peak (2.8 eV) is identified as the feature due to photoemission
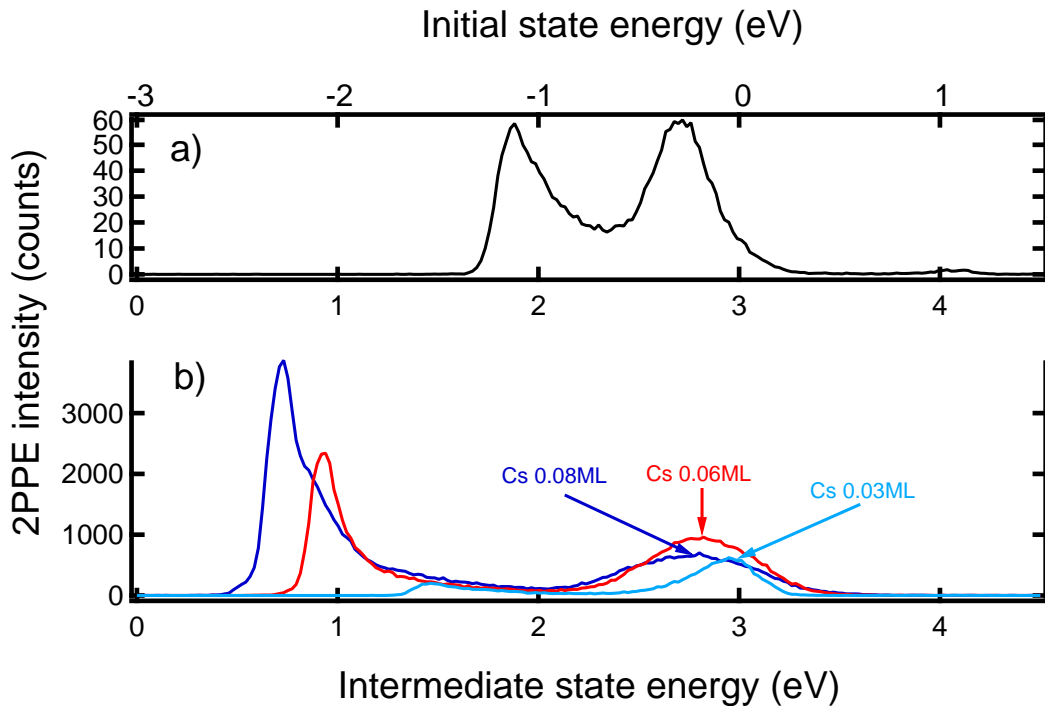


Figure 4.1: a) Two-photon photoemission (2PPE) spectra (h$\nu$=3.1 eV) measured with $p$-polarized light in normal emission from clean Cu(111) and b) from Cs on Cu(111).

from the Shockley surface state. The small feature near (4.2 eV) is attributed to three-photon photoemission (3PPE) through the n=1 image potential state. In Fig. 4.1 b) the 2PPE spectra from Cs on Cu(111) are shown. For increasing amount of Cs there is lowering of work function which is shown in the spectra as the work function cut off shifts to lower energy values. For Cs coverage above 0.06 ML we observe a clear peak coming from 2PPE through the unoccupied Cs state at around 2.9 eV. With increasing Cs coverage this peak shifts to lower energy and its intensity grows due to resonant transition from Shockley state via unoccupied Cs state.
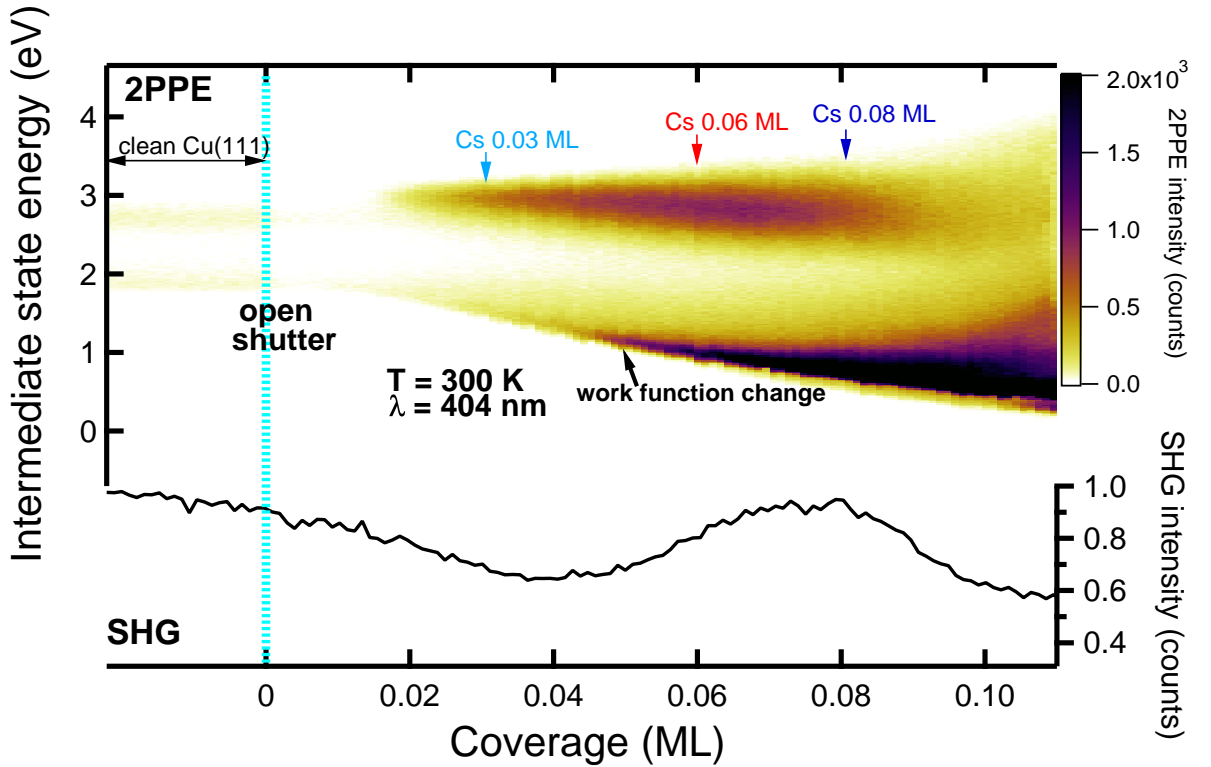


Figure 4.2: 2PPE spectra and SHG intensity, measured during the deposition of the Cs on Cu(111) at 300 K.

The 2PPE spectra presented in Fig. 4.1, are extracted from an experiment during the Cs adsorption. During the Cs deposition we measured simultaneously the 2PPE spectra and the intensity of second harmonic generation (SHG) from the Cu(111) surface. Fig. 4.2 shows the whole evolution of the 2PPE and SHG during Cs adsorption at 300 K. The upper part represents 300 individual 2PPE spectra measured in normal emission geometry, while the lower part shows the SHG intensity. In the beginning of the experiment (before the shutter was opened) we observed 2PPE and SHG signals from Cu(111). On the intermediate state energy scale around (2.8 eV), the feature from the optical transition via Shockley surface state was observed. The intensity increase around (1.9 eV) comes
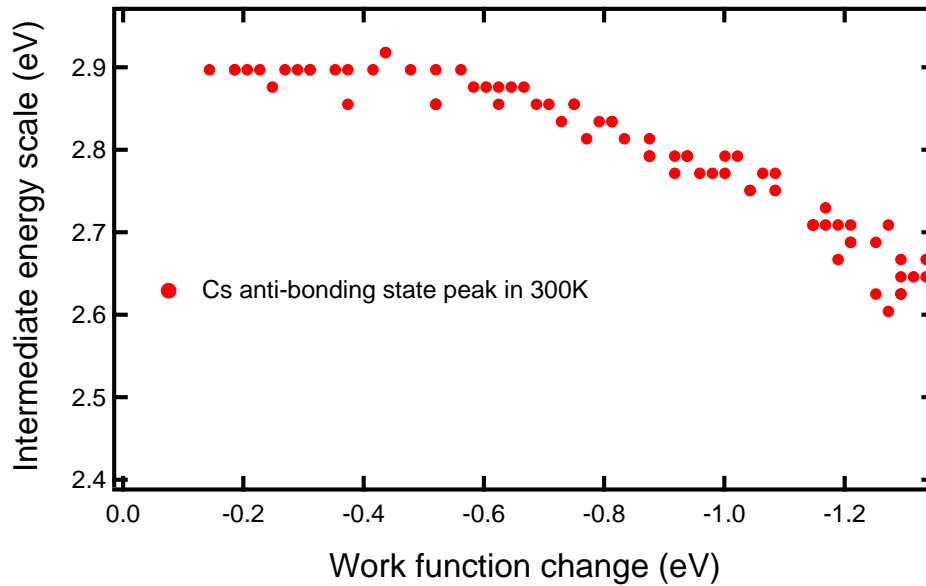
Figure 4.3: Energy position of the unoccupied Cs state extracted from 2PPE spectra in Fig.4.2 as function of the work function change.

from the bulk states in Cu(111). Marked by the black arrow there is the border between the white and coloured area indicating the work function change. For clean Cu(111) the work function is 4.9 eV. After opening the shutter, a shift of the work function to lower energy is observed. Simultaneously the signal from the Cs state appears at slightly higher
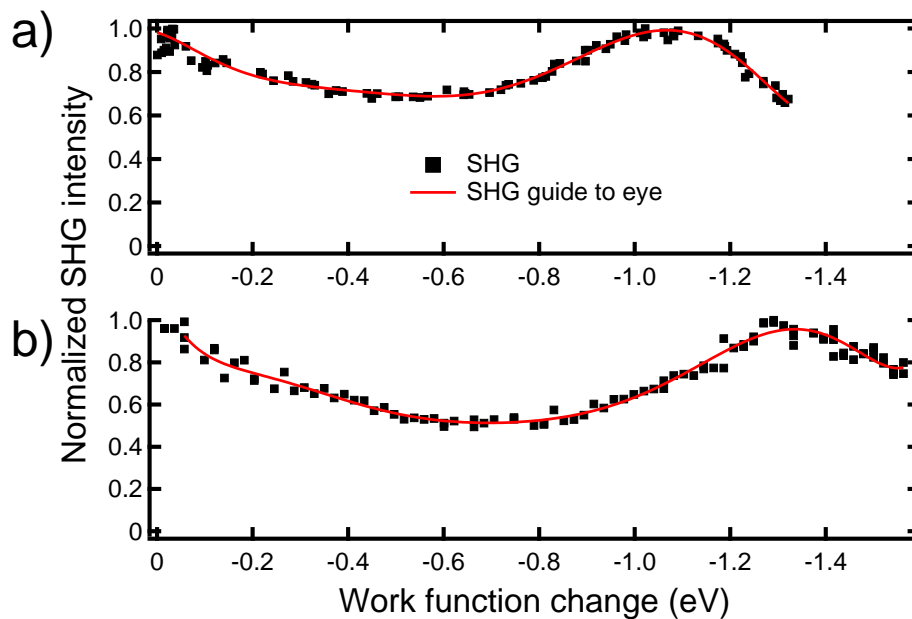


Figure 4.4: Intensity of second harmonic generation during the Cs adsorption on Cu(111) measured for different photon energies. a) 3.07 eV and b) 2.96 eV.

energy than the signal from the Shockley surface state and shifts continuously with increasing Cs coverage to lower energy. The Cs state energy extracted from the 2PPE spectra in Fig. 4.2 is presented in Fig. 4.3 as the function of measured work function change from the cutoff of the 2PPE spectra. Spectra shown in Fig. 4.1, are marked in Fig. 4.2 by arrows.
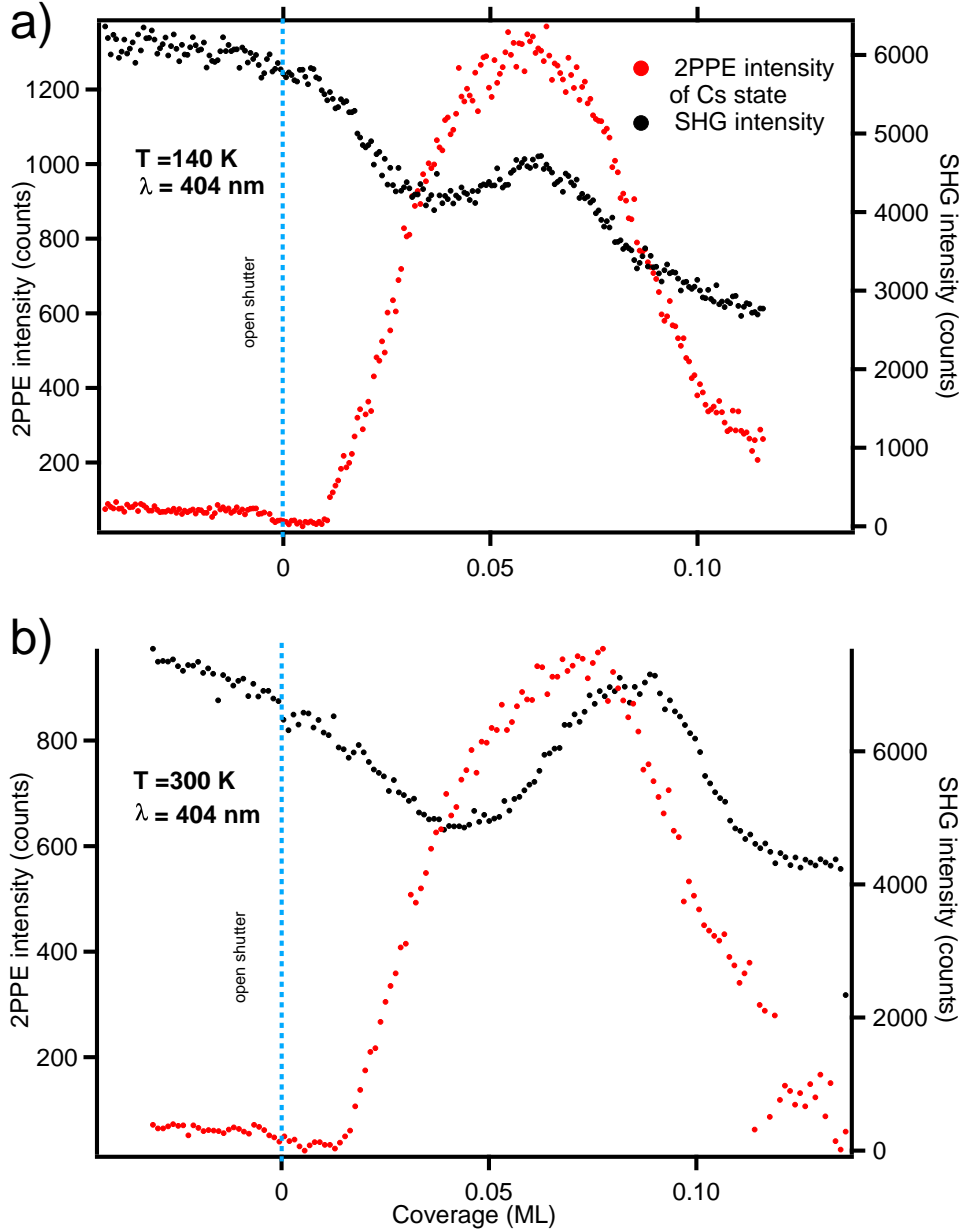


Figure 4.5: Temperature dependent behaviour of SHG and 2PPE intensity during the deposition of Cs at a) 140 K and b) 300 K.

The lower part of Fig. 4.2, shows SHG intensity modulation during the Cs adsorption. Shortly after opening the shutter we observe decrease of SHG intensity and then an

increase up to a point of maximum. The position of maximum in SHG intensity corresponds approximately to the intensity maximum position of the of the 2PPE spectra and indicates the unoccupied Cs state formation (upper part of Fig. 4.2). We investigated the SHG intensity modulation during Cs adsorption for two different (3.07 eV and 2.96 eV) photon energies as shown in Fig. 4.4. Clear shift of SHG maximum with photon energy change is observed and will be explained in the discussion Sec. 5.1.1.

Furthermore we studied the temperature dependent 2PPE together with SHG during the Cs adsorption on Cu(111). 2PPE and SHG intensity is plotted against the Cs coverage in Fig. 4.5 for a) 140 K and b) 300 K. The visible temperature dependence of 2PPE and SHG analysis will be explained in the discussion Sec. 5.1.2.

## 4.2 One- and two-photon photoemission from Fe/Ag(001)

In Fig. 4.6 the one-photon photoemission (1PPE) spectra measured during the Fe film growth on Ag(001) at 150 K are shown in a two-dimension color plot. This measurement was performed with $p$-polarized light and photon energy h$\nu$=6.2 eV. The final energy for photoelectrons is displayed on the vertical axis on the left side. The intensity of 1PPE spectrum which corresponds to count of measured photoelectrons is shown by the colour
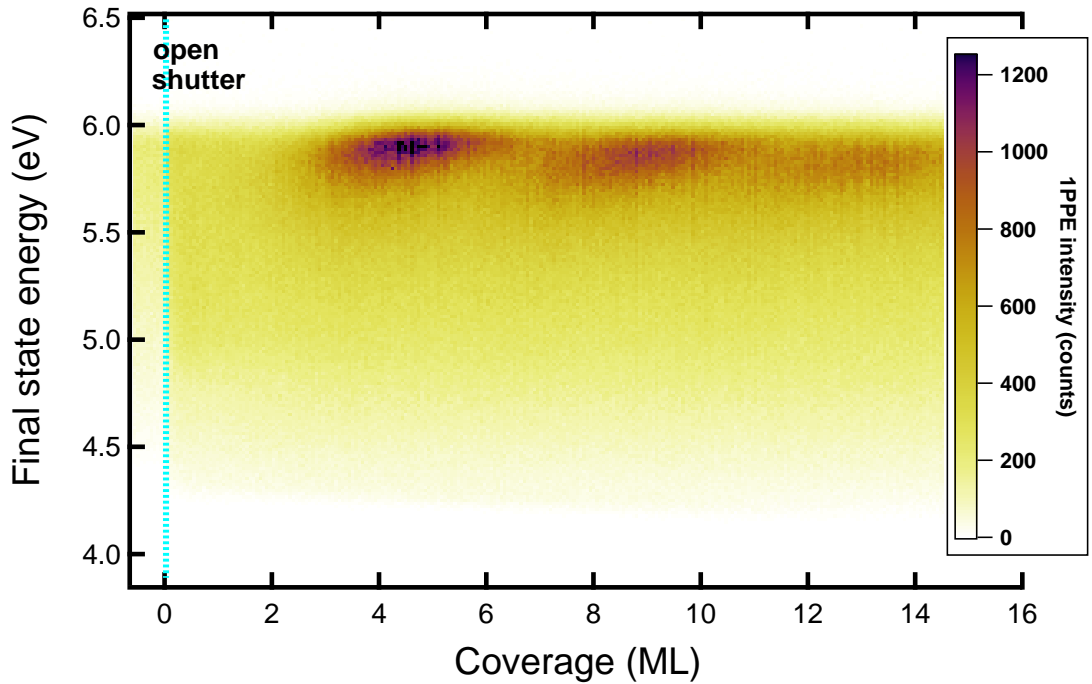


Figure 4.6: One-photon photoemission (1PPE) spectra measured with $p$-polarized light in normal emission during the deposition of Fe on Ag(001). The experiment was preformed at T=160 K with photon energy h$\nu$=6.2 eV.

scale in box. We estimated the work function of Ag(001) for 4.4 eV. After opening the shutter the intensity increase due to Fe deposition is observed. Starting from coverage around 4.5 ML, the 1PPE intensity oscillates at 5.9 eV with period of 4.5 ML. This intensity oscillation indicates a formation of occupied quantum well states derived from a Fe d-band and will be discussed in detail in discussion Sec. 5.2.
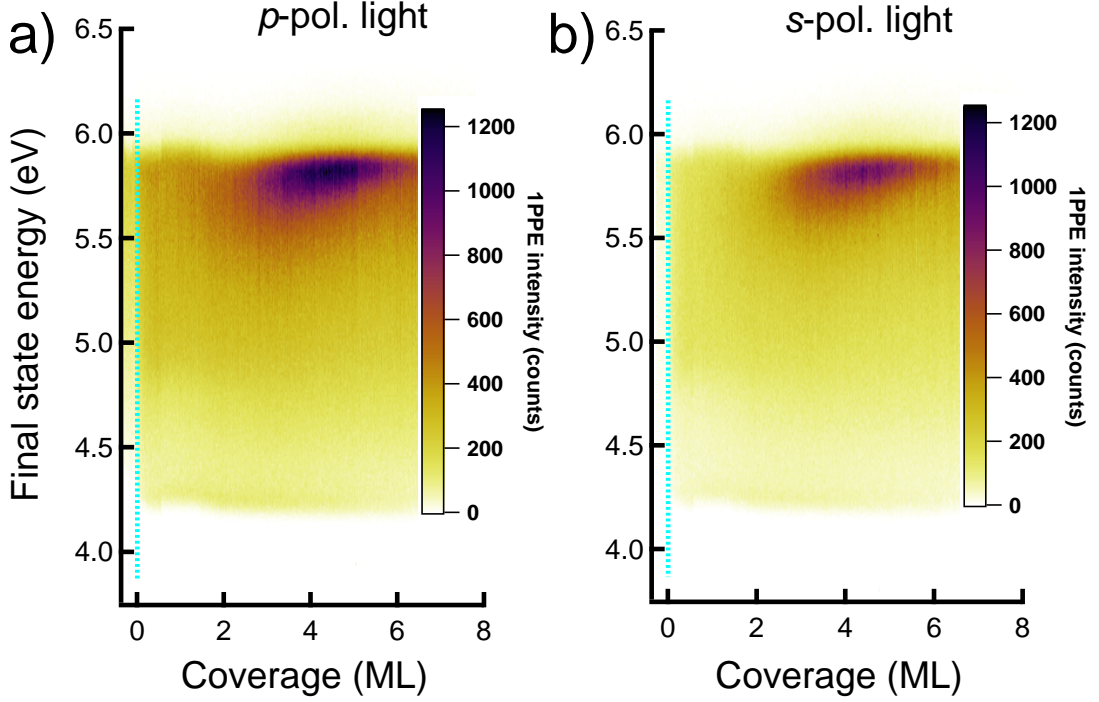


Figure 4.7:    One-photon photoemission (1PPE) spectra measured with a) *p*-polarized and b) *s*-polarized light in normal emission during the deposition of Fe on Ag(001). The experiment was preformed at T=150 K with photon energy h$\nu$=6.2 eV.

The 1PPE measurements shown in Fig. 4.7 were performed with *p*-polarized and *s*-polarized light. The experimental conditions where comparable to those in Fig. 4.6 except of a much slower deposition rate. The slow deposition rate (129 s per ML) allowed us to take simultaneously the 1PPE spectra for both *s* and *p* polarizations. Switching between the light polarization took place every 13 seconds. Both a) and b) spectra in Fig. 4.7 contain 300 spectra within a coverage of 7.8 ML. The spectra in Fig. 4.7 a) and Fig. 4.7 b) show an intensity increase around 4,5 ML in agreement with the result presented in Fig. 4.6.

Fig. 4.8 shows the two-photon photoemission (2PPE) spectra and the intensity of second harmonic generation (SHG) measured with incident *p* and *s*-polarized light during the deposition of Fe on Ag(001). The deposition rate is the same as described in the measurements shown in Fig. 4.7. In Fig. 4.8 a) at energy around 5.9 eV we observe an intensity increase in 2PPE spectra from 2.5 ML coverage to 5 ML . In Fig. 4.8 b) at around
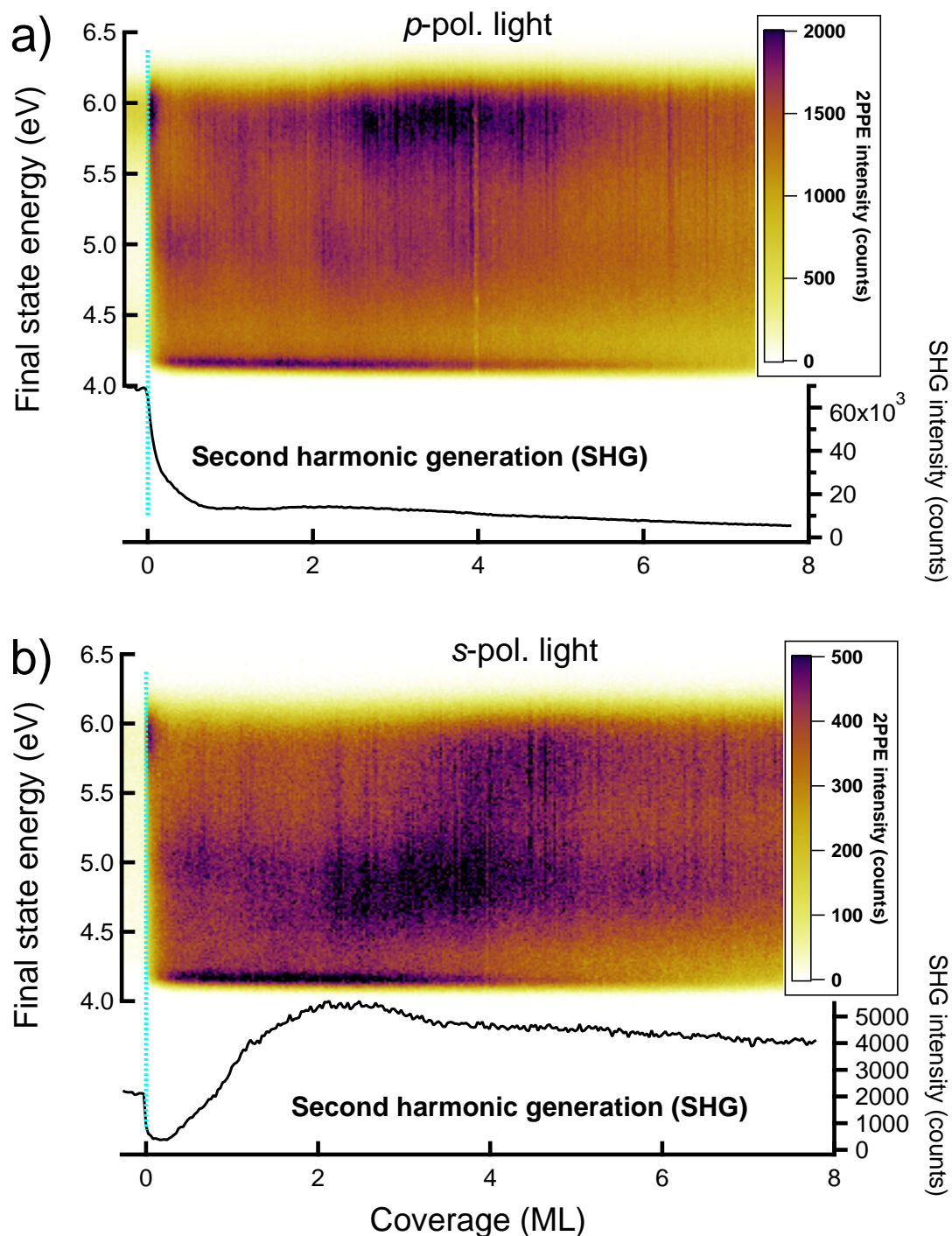
Figure 4.8: Two-photon photoemission (2PPE) spectra in normal emission and second harmonic generation (SHG) intensity measured with a) $p$-polarized and b) $s$-polarized light during deposition of Fe on Ag(001). Measurements were preformed at T=150 K with photon energy h$\nu$=3.1 eV.

5.9 eV we see intensity increase starting from 3.5 ML to 5 ML in 2PPE spectra. This intensity increase agrees well with the intensity increase shown in Fig. 4.6 and Fig. 4.7 for 1PPE. A detailed comparison of 1PPE and 2PPE spectra with calculated band structure will be discussed in Sec. 5.2.
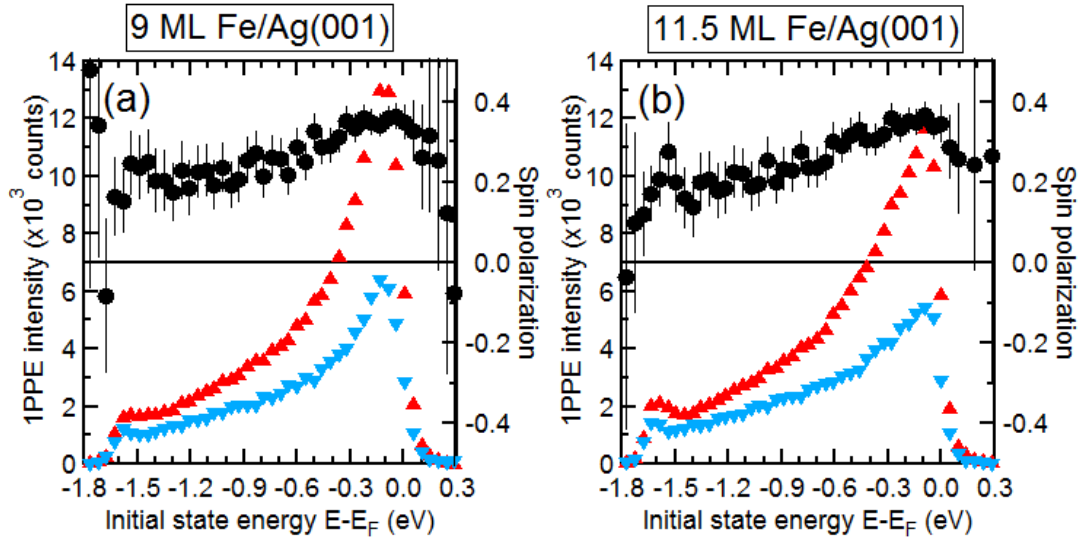


Figure 4.9: Spin-polarized one-photon photoemission spectra measured for a) 9 ML and b) 11.5 ML of Fe/Ag(001). The experiment was preformed at T=135 K) with photon energy hν=6.22 eV.

The measurements presented in Fig. 4.9 show the spin-polarized photoemission spectra for a) 9 ML and b) 11.5 ML of Fe film on Ag(001). The measurements were performed at T=135 K with photon energy hν=6.2 eV. The 1PPE spin-polarized spectra are plotted against the initial state energy. The spin-polarization of photoelectrons is shown with a scale on the right axis in Fig. 4.9. These spin-resolved data provide insight into the spin-dependent electronic states of the ultrathin Fe films and will be further discussed in detail in Sec. 5.2.

## 4.3 Angle-dependent multiphoton photoemission from Ag(001), Fe/Ag(100) and O/Fe/Ag(001)

In Fig. 4.10, Fig. 4.11 and Fig. 4.12 angle-resolved multi-photon photoemmision spectra from Ag(001), 20 ML Fe/Ag(001) and oxygen covered 20 ML Fe/Ag(001) are shown. Each figure consist from 2PPE and 3PPE parts displayed with the final state energy scale. The 2PPE part with a linear intensity scale on the left side, and the 3PPE part is shown with a logarithmic intensity scale on the right side. Due to the lower intensity the 3PPE part

Figure 4.10:    Angle-resolved multi-photon photoemission from Ag(001) measured at 150 K. The emission angle is from 24° to 15° with a 3° step. Measurements are performed with $p$-polarized light and 3.1 eV photon energy. The 2PPE and 3PPE spectra are shifted vertically for clarity. 3PPE spectra were measured 10 times longer than 2PPE.
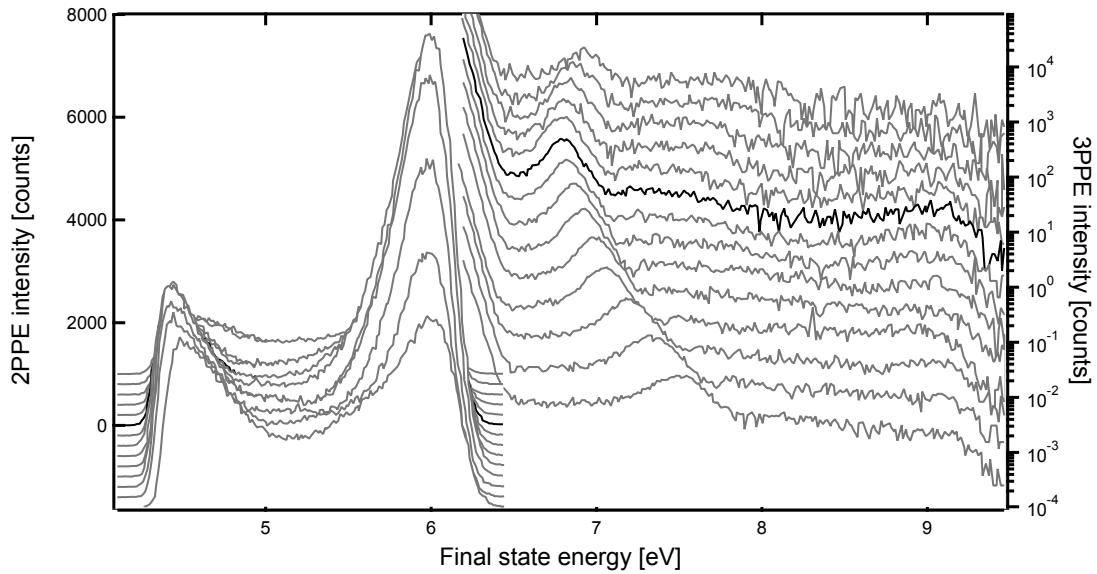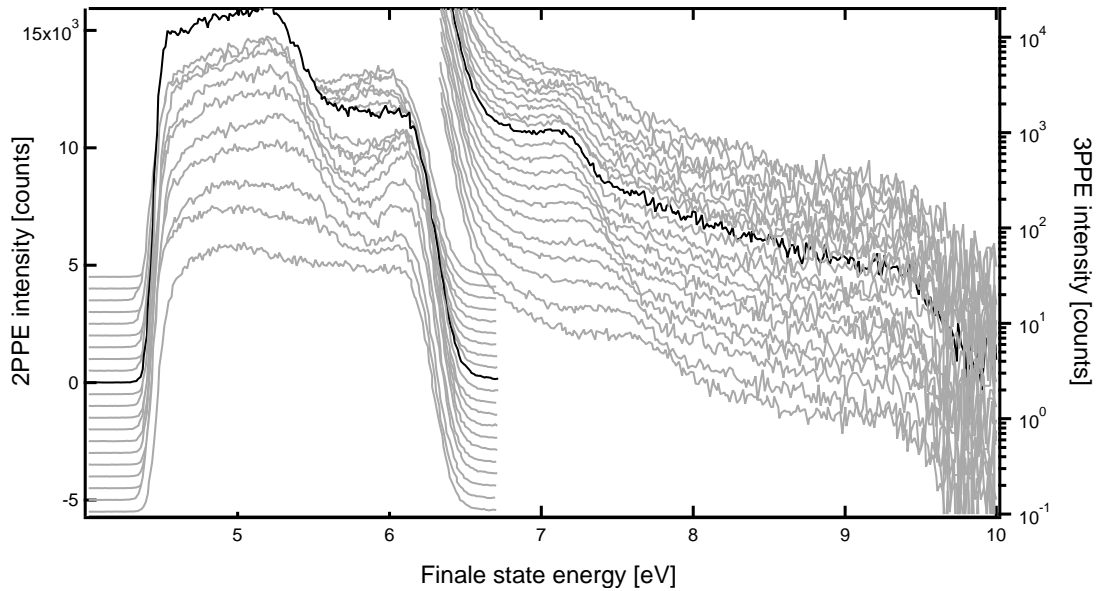


Figure 4.11:    Angle-resolved multi-photon photoemission from 20 ML Fe/Ag(001) measured at 160 K. The emission angle is from 22° to 18° with a 2° step. Measurements are performed with $p$-polarized light and 3.1 eV photon energy. The 2PPE and 3PPE spectra are shifted vertically for clarity. 3PPE spectra were measured 8 times longer than 2PPE.

Figure 4.12: Angle-resolved multi-photon photoemission from oxygen covered 20 ML Fe/Ag(001) measured at 150 K. The emission angle is from 18° to 12° with a 2° step. Measurements are performed with *p*-polarized light and 3.1 eV photon energy. The 2PPE and 3PPE spectra are shifted vertically for clarity. 3PPE spectra were measured 8 times longer than 2PPE.
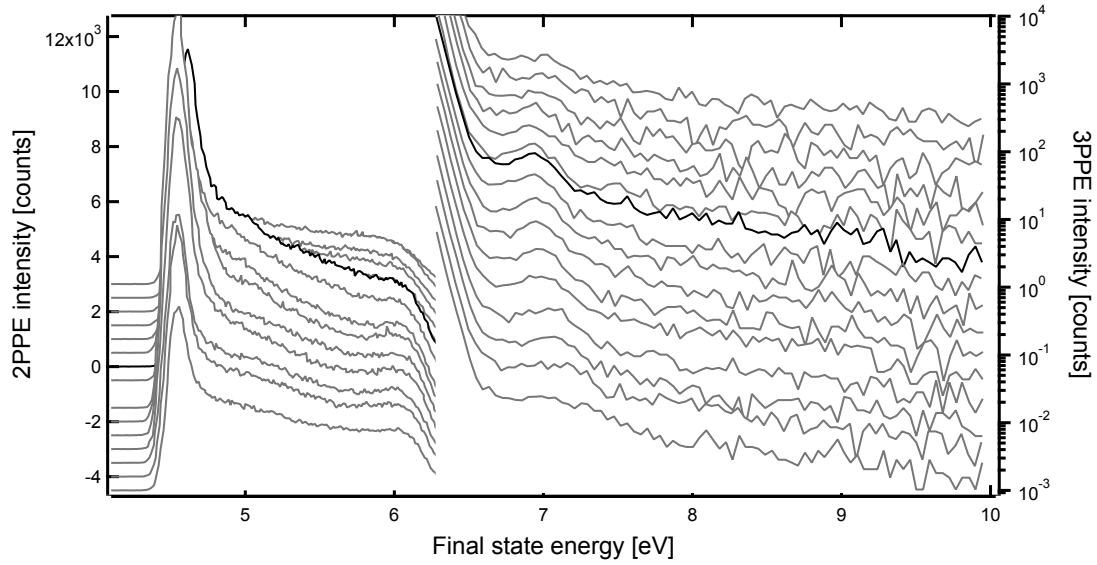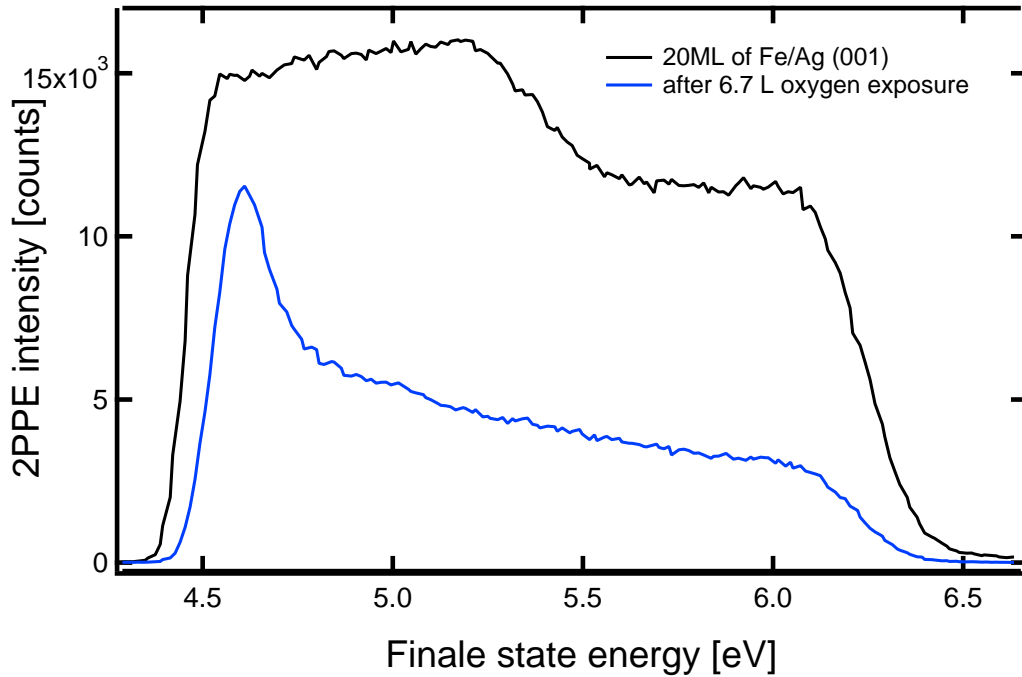


Figure 4.13: Two-photon photoemission spectrum from 20 ML of Fe on Ag(001) at room temperature before (black solid line) and after exposure of 6.7 L oxygen (blue solid line).

is measured 10 times longer then the 2PPE part. For the clarity the spectra are shifted vertically in the waterfall plot. Zero on the vertical axis corresponds to spectrum measured in normal emission geometry, which is shown as the thicker black curve. In the 3PPE part we observe image potential state dispersion in the energy range from 7 to 8 eV with characteristic dispersion in Fig. 4.10 and Fig. 4.11. However, significantly less dispersion is observed on the oxygen covered Fe/Ag(001) surface as shown in Fig. 4.12. The detailed analysis of the dispersion will be discussed in detail in Sec. 5.3. Two-photon photoemision spectrum from 20 ML Fe film on Ag(001) was oxidized up to 6.7 L and is presented in Fig. 4.13. The oxygen exposure details are described in Sec. 3.5.

## 4.4     Time-resolved two-photon photomission through the unoccupied quantum well state in Co/Cu(001)

Fig. 4.14 shows the 2PPE and SHG intensities during cobalt deposition on Cu(001). The integrated 2PPE intensity oscillates with of one monolayer period. The SHG intensity decreases with increasing coverage.

Fig. 4.15 shows time-resolved 2PPE data from 7 ML Co/Cu(001) measured at 150 K. Fig. 4.15 a) presents the result of the room temperature cobalt film grow whereas Fig. 4.15 b) the result of the low temperature film grow.
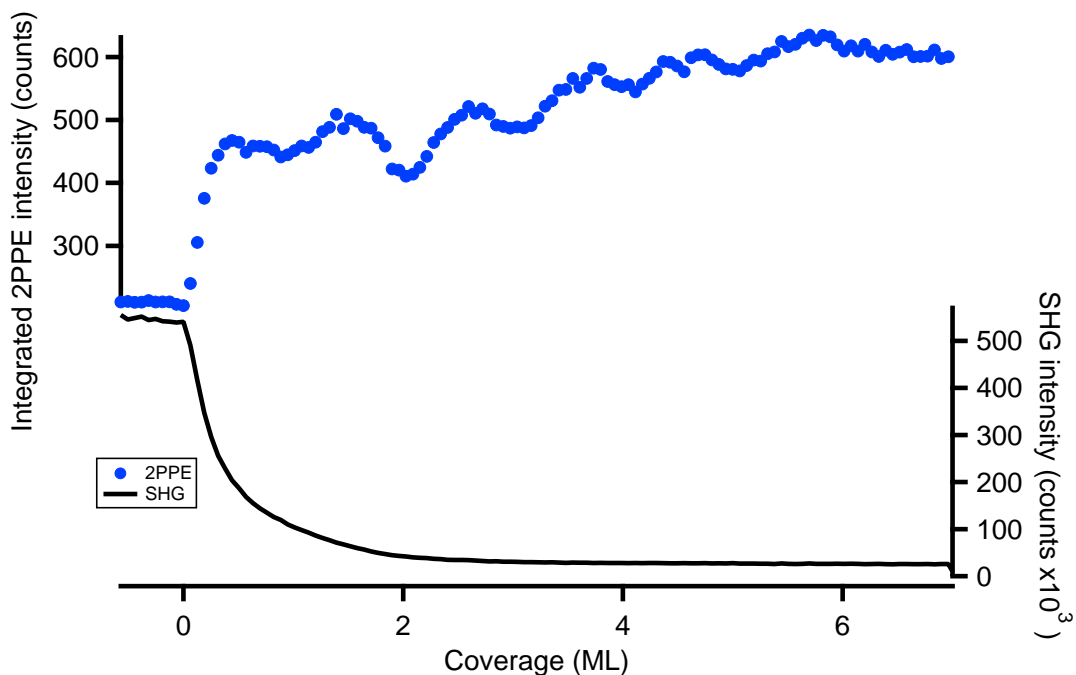


Figure 4.14:   2PPE and SHG intensities during cobalt deposition on Cu(001).
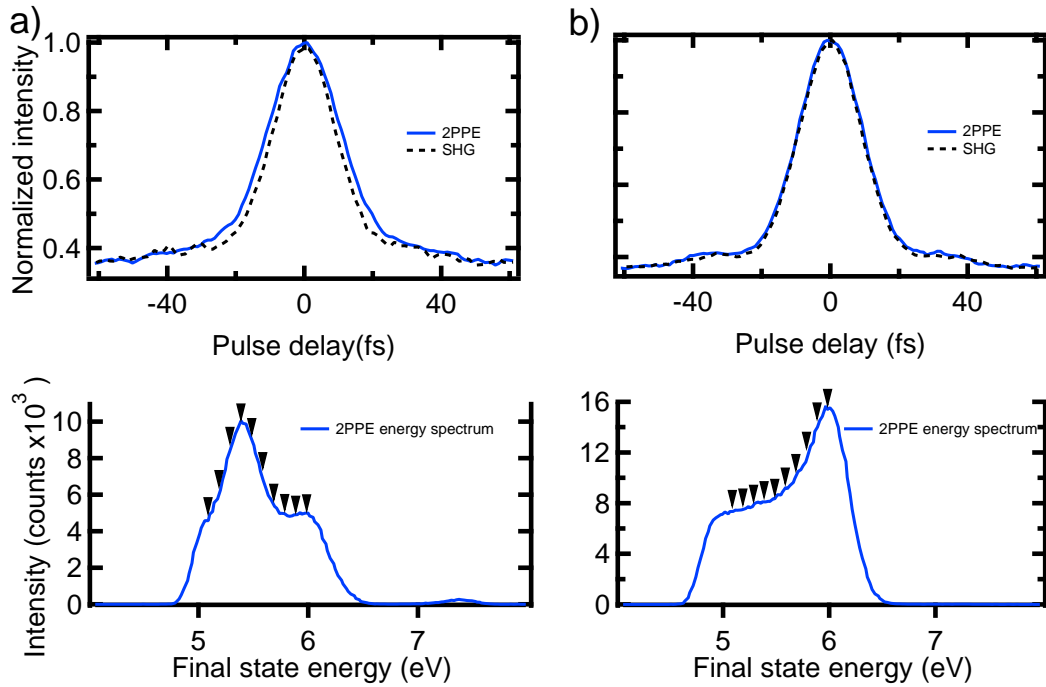
Figure 4.15:   Time-resolved 2PPE data from 7 ML Co/Cu(001) measured at 150 K. In
the upper part, the $0\omega$ envelopes of the 2PPE cross-correlation measured at 5.4 eV are
shown. In the lower part, the 2PPE spectra with the arrows marking all energies at which
the cross-correlation was measured, are shown. a) film grown at 300 K, b) film grown at
150 K.
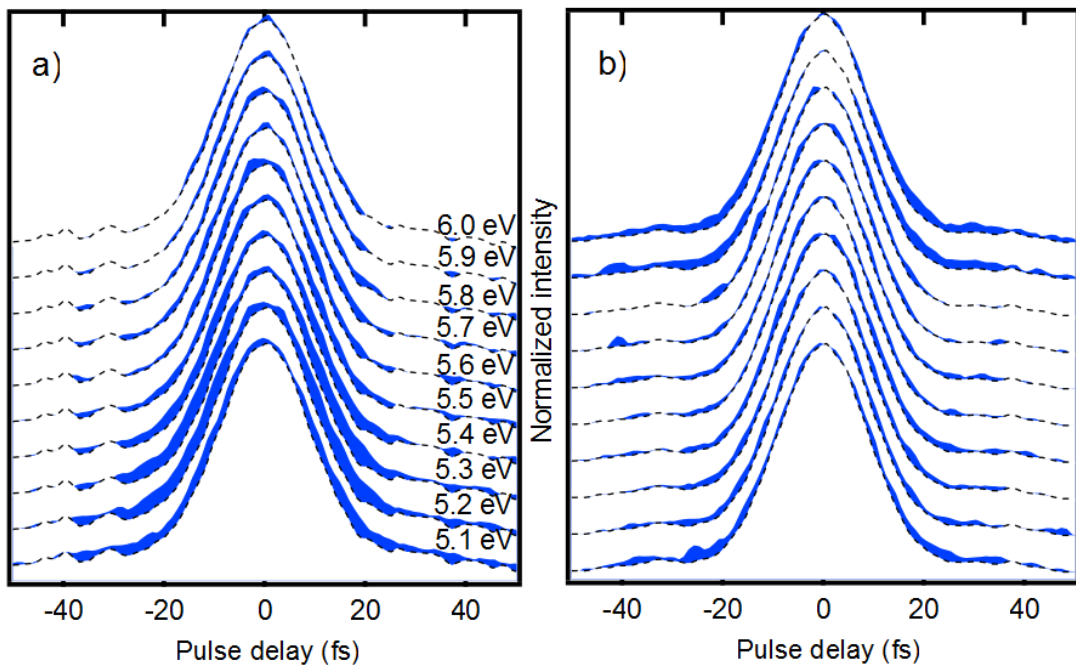


Figure 4.16:   Comparison of the $0\omega$ envelopes of the 2PPE cross-correlation measured at
energies indicated by arrows in Fig. 4.15. a) film grown at 300 K, b) film grown at 150 K.

The 2PPE spectrum in the bottom panel of Fig. 4.15 a), shows a feature at 5.4 eV specified as the well-known unoccupied quantum well state in the cobalt film [92]. Fig. 4.15 b) doesn't show the clear feature of the quantum well state at 5.4 eV. In the upper part of Fig. 4.15, we see the $0\omega$ envelopes of the 2PPE and the SHG interferometric correlation curves measured at 5.4 eV.

Fig. 4.16 shows the $0\omega$ envelopes of the 2PPE cross-correlation measured at energies marked by arrows in Fig. 4.15. The $0\omega$ envelopes are shifted vertically for clarity. The blue colour indicates a difference in width between the envelopes of the 2PPE and the SHG interferometric correlation curves. The FWHM of the $0\omega$ envelope of the 2PPE cross-correlation is showed in Fig. 4.17.



Figure 4.17:   The FWHM of the $0\omega$ envelope of the 2PPE cross-correlation for a cobalt film grown at room temperature.

The time-resolved 2PPE results can give information about the dynamics of optically excited electrons in the unoccupied quantum well state. A discussion about the life time broadening due to quantum well formation is presented in Sec. 5.4.

# 5 Discussion

In this chapter I'm going to discuss the experimental results presented previously. In Sec. 5.1 the electronic states in Cs on Cu(111) responsible f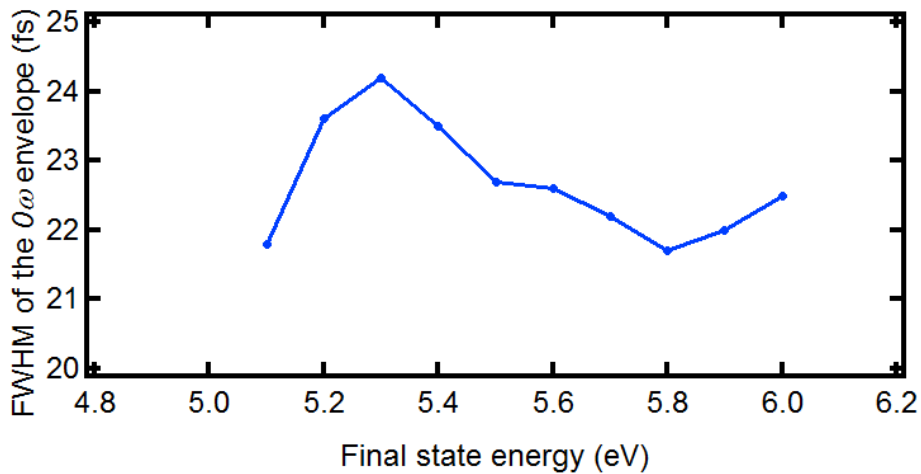or the observed resonant transitions are discussed and identified by combined two-photon photoemission (2PPE) and second harmonic generation (SHG) techniques. Sec. 5.1 contains two subsections: Sec. 5.1.1 and Sec. 5.1.2. In Sec. 5.1.1 the simultaneous 2PPE and SHG experiments during Cs adsorption on Cu(111) at low temperature and the photon energy dependence are discussed. The optical transition from the occupied Shockley surface state (SS) to the unoccupied Cs state is concluded to be responsible for the observed intensity maximum in SHG and 2PPE. In Sec. 5.1.2 the experiments at room temperature and its relation to the low temperature are discussed. There the additional contribution in SHG from other optical transition such as SS to the image potential (IP) state is considered. In Sec. 5.2 the origin of the oscillations observed in Fe on Ag(001) is discussed based on the symmetry selection rules. In Sec. 5.3 the dispersion of the image potential state on clean Ag(001), Fe on Ag(001) and oxidized Fe on Ag(001) as well as the binding energy and effective mass are discussed. In Sec. 5.4 the analysis of time-resolved studies of Co on Cu(001) and the lifetime of the unoccupied quantum well state are presented.

## 5.1 Similarities and differences in SHG and 2PPE from Cs/Cu(111)

### 5.1.1 Surface state to Cs-state resonance in SHG

The 2PPE investigation of Cs/Cu(111) has been reported in literature [93–95]. Schema in Fig. 5.1 explains the mechanism of resonant transition through the unoccupied Cs state during adsorption. The Cs state is formed in the initial stage of deposition around 2.9 eV. As coverage increases the Cs state shifts from non-resonant to a resonant position. This allows the resonant optical transition from the occupied Cu(111) surface state (SS) to the Cs state. This resonant transition can be seen in experiment as the 2PPE intensity increases as shown in Fig. 4.1 and Fig. 4.2. Upon further deposition the Cs state shifts more toward lower energy to a non-resonant position as shown in Fig. 5.1.

In Fig. 4.2 a direct comparison between the SHG and the 2PPE signals measured during Cs adsorption is shown. In SHG intensity we observe a maxima at nearly the same Cs coverage where the maximum occurs in the 2PPE. This observation agrees with the simplified model shown in Fig. 5.1 since the 2PPE is also expected to show the maximum
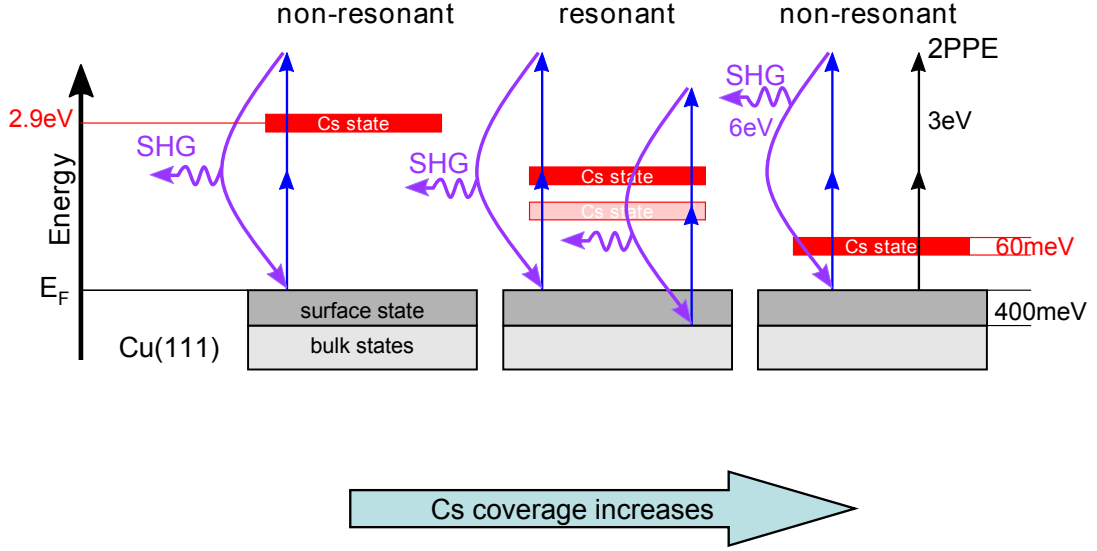
Figure 5.1: Schematic showing the second harmonic generation (SHG) and two-photon photoemission (2PPE) on Cs/Cu(111) with the energy shift of the Cs state during the deposition. At certain Cs state energy positions a resonant optical transition through the Cs state occurs.

due to the resonant transition [93–95]. The SHG intensity variations described in literature for monolayer coverages [96, 97] has been associated with transitions involving the Cu(111) surface state. In our investigation we were able to precisely assign the dominant parts in the experimentally observed SHG signal to a specific optical transitions. The literature concerning SHG measurements from Cu(111) surface [98, 99] provides an investigation with different photon energies in order to understand better the origin of the SHG intensity change. In our experiments we changed the photon energy from 3.07 eV to 2.96 eV to check possible characteristic features from optical transitions responsible for SHG. By such photon energy change we influence our resonance condition and as a consequence we observed its direct impact on SHG signal as shown in Fig. 5.2.

In Fig. 5.2 the SHG intensity is plotted as a function of the work function change due to Cs adsorption. The maximum observed in Fig. 5.2 a) has a full-width-at-half-maximum (FWHM) of 0.4 eV. This value corresponds nicely to the energy range of the Shockley surface state dispersion presented in Fig. 5.2 b) which is 0.4 eV in the occupied region. The SHG peak position shifts by 0.27 eV on the work function energy scale when we change the photon energy by 0.11 eV as shown in Fig. 5.2 a). From these two numbers
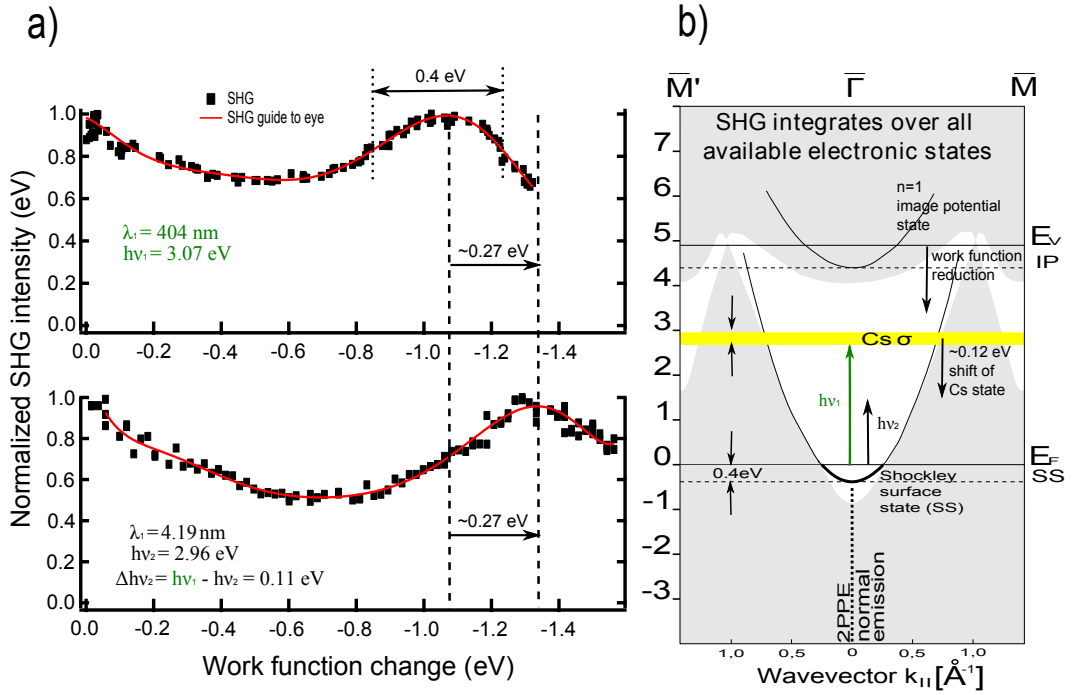
Figure 5.2: a) SHG during Cs adsorption on Cu(111) for different photon energies, b) surface projected bulk band structure of Cu(111) with the unoccupied anti-bonding Cs state.[100]

we could derive a phenomenological ratio defined as:

$$\frac{\text{change in photon energy}}{\text{change in work function}} = \frac{0.11\,eV}{0.27\,eV} = 0.4. \tag{5.1}$$

According to the simplified picture in Fig. 5.1, the SHG intensity reaches maximum when the Cs state moves into resonance with the Shockley surface state at the given photon energy. It is therefore important to have a quantitative estimation of the energy shift of the Cs state as a function of the Cs coverage or the corresponding work function change. The change of work function caused by Cs adsorption [88, 93–95] is summarized in Fig. 5.3 together with the experimental data points from Fig. 4.2. From Fig. 5.3 we can get a quantitative estimation of the energy shift of the Cs state during the adsorption. For the two different values of Cs coverage at which we observed the intensity maximum in Fig. 4.4, the values of work function are 1.08 eV and 1.35 eV and the Cs state is located at 2.65 eV and 2.53 eV as indicated by the filled area in Fig. 5.3. The resonance conditions at these two different Cs coverage can be expressed in terms of a similar phenomenological ratio defined previously:

$$\frac{\text{change in Cs state energy position}}{\text{change in work function}} = \frac{0.12\,eV}{0.27\,eV} = 0.44. \qquad (5.2)$$

Comparing the numbers in Eqn. 5.1 and Eqn. 5.2 indicates that the SHG maximum in Fig. 4.4 can be quantitatively explained by a resonant optical transition between the Shockley surface state and the unoccupied Cs state. Moreover, the SHG peak width of 0.4 eV indicates that the whole occupied part of the surface state with different parallel momentum plays an important role contributing to the SHG intensity.
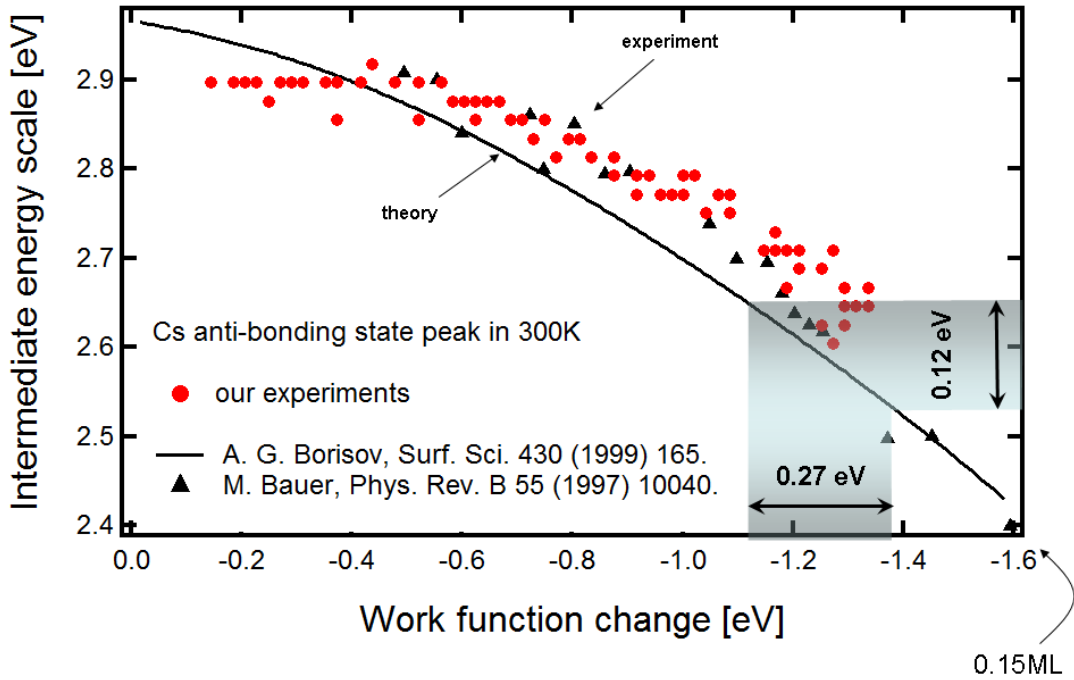


Figure 5.3: Excited Cs state energy positions in normal emission 2PPE for Cs on Cu(111) as a function of work function change during Cs adsorption. Red circles - our data; Black triangles - Ref. [95]; Solid black line - Ref. [101]

## 5.1.2 Temperature influence on SHG and 2PPE.

In the previous subsection it was shown that the origin of the SHG maximum can be attributed to resonant optical transitions between the occupied Shockley surface state (SS) on Cu(111) and the unoccupied Cs state. The low temperature investigation in Fig. 4.5 a) shows a clear agreement of the 2PPE and SHG peak position at the same Cs

coverage as expected from the simplified model in Fig. 5.1. In contrast, in the experiment performed at room temperature the 2PPE and SHG have maxima at different Cs coverage as shown in Fig. 4.5 b). The shift between 2PPE and SHG maximum position corresponds to a difference in the Cs coverage that leads to a work function difference of 0.14 eV. This result is very surprising since it neither agrees with the simple model shown in Fig. 5.1 nor the results from the low temperature measurement. Since the SS to Cs state transition should give the same maximum position in SHG and 2PPE, we include in this section other additional optical transitions to discuss the observed temperature dependent deviation of the maximum position in SHG from 2PPE. The electronic states that play a role in the SHG process will be considered in a numerical model.

As discussed in the previous section, the 2PPE maximum comes from the well-defined transition between the Cs state and the Shockley surface state (SS), therefore the shift between the maximum of the SHG and 2PPE intensity implies that some other optical transitions contribute to the SHG signal and they might be responsible for the shift observed in Fig. 4.5 b) at room temperature. Consideration of this temperature dependent shifts of the surface electronic structure as a function of the Cs coverage in Ref. [96] allows to model available optical transitions for our photon energy in order to find possible resonances in SHG. In Fig. 5.4 the data form Ref. [96] is presented.

The arrows marked in Fig. 5.4 indicate possible optical transitions from the SS to n=1 image potential (IP) state, from the Cu $d$-bands through a virtual state to the n=1 IP state or to the n=2 IP state. In the first step we will concentrate on the SS to n=1 IP state transition which occurs in the range of Cs coverage between 0.06 ML and 0.1 ML. In order to simulate the SHG intensity contribution from the SS to n=1 IP transition we will use the theoretical model [102–105]:

$$I^{2\omega}(\omega, T, \theta) = I_0(\omega, T) \left[ \int dk_{\parallel} \frac{F_a(k_{\parallel}, T, \theta)}{\sqrt{[\hbar\omega - E_{ba}(k_{\parallel}, T, \theta)]^2 + [\Gamma(T, \theta)]^2}} \right]^2 , \qquad (5.3)$$

where $F_a$ is the Fermi-Dirac distribution function, $\hbar\omega$ is the incident photon energy, $E_{ba}$ is the energy separation between a given pair of occupied state $a$ and unoccupied state $b$, and $\Gamma$ is the linewidth of the transition. Fig. 5.5 shows the numerical results of Eqn. 5.3.

The values of $E_{ba}$ are directly taken from Ref. [96], the $F_a$ is calculated for the SS as initial state, the photon energy $\hbar\omega$=3.06 eV, and the $\Gamma$ value in Eqn. 5.3 is set to an assumed constant value of 30 meV for all range of thickness $\theta$. The $I_0$ is set to a constant value in order to fit the experimental data. In Fig. 5.5 a) we see a reasonable agreement of the modelled SHG intensity maximum with the experimental data maximum. That confirms that the SS state to n=1 IP state transition plays an important role and should
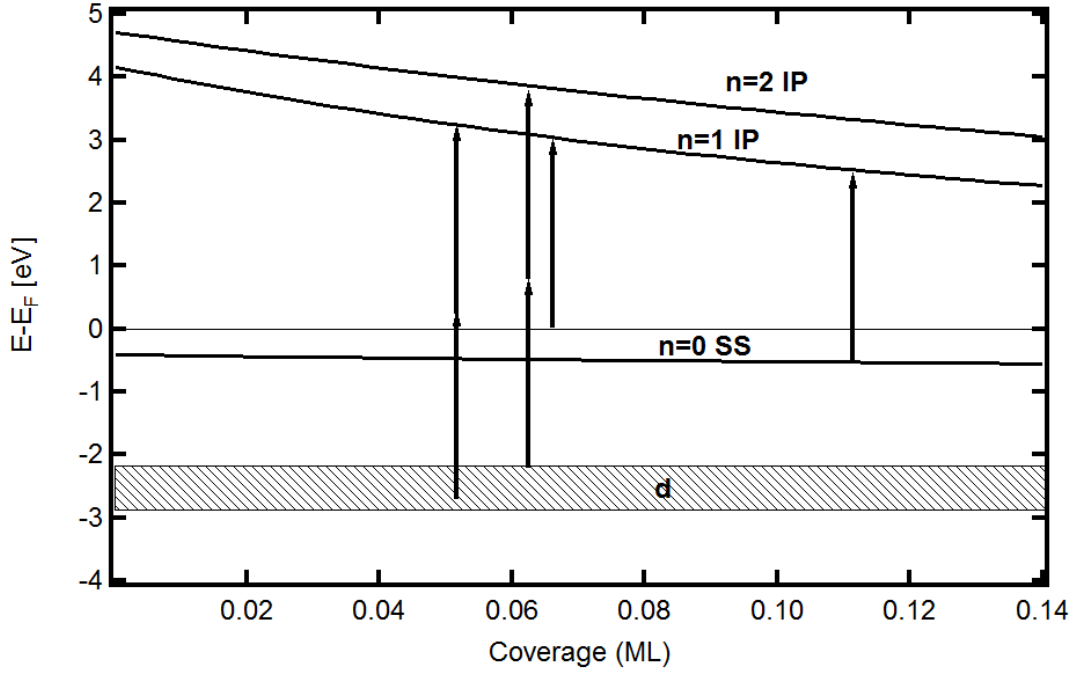
Figure 5.4:   Energy shifts of surface electronic structure as a function of the Cs coverage [96].

therefore be also responsible for the discrepancy between the 2PPE and the SHG intensity maxima observed at room temperature in Fig. 4.5 b).

At low temperature the 2PPE and SHG maxima overlap. The influence of temperature effects can be clearly seen at room temperature by the deviation of SHG maximum from the 2PPE maximum. For both SHG and 2PPE from Cs/Cu(111), there are several temperature dependent effects coming from the electronic states. One of which is the temperature dependent shift of the Shockley surface state toward the Fermi level [106–109]. In our range of temperature this shift is estimated to be 0.03 eV toward the Fermi level. In Ref. [110] for 0.10 ML Cs coverage a shift of 0.1 eV of the Cs state peak position between 2PPE spectra measured at 300 K and 100 K is reported and attributed to temperature and photodesorption shifts. In Ref. [98] concerning the SHG from Cu(111) surface during molecular adsorption the shift of main peak upon increasing the temperature is reported and attributed to temperature dependent SS state shift towards the Fermi level. Other processes which have influence on the dynamics of Cs adsorption are the adsorption sites of Cs atoms [95, 110, 111]. The change of the relative proportion between atop and hollow site adsorption at 300 K and 140 K influences the Cs surface dipole and can change in principle the averaged Cs state energy position with respect to the Fermi level. Moreover the different Cs adsorption sites can contribute to the apparent width of the Cs state [101]. In addition, there is a thermal broadening of the Shockley
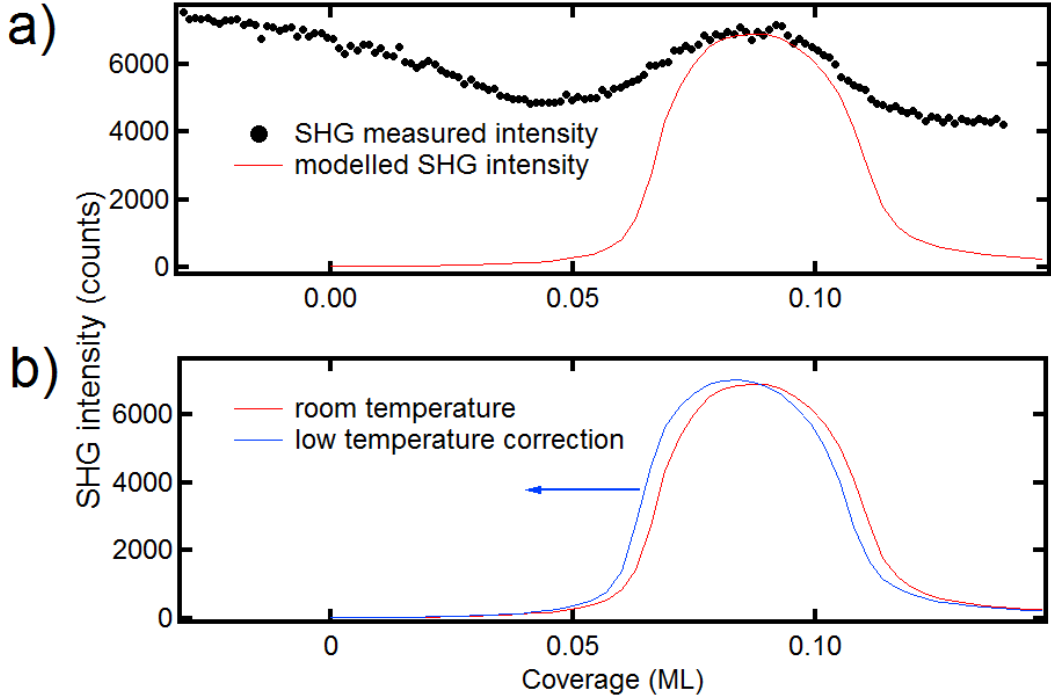
Figure 5.5:    a) Comparison of experimental data with result of a model calculation integrating all vertical optical transitions between the occupied SS state and the unoccupied n=1 IP state, b) calculated SHG intensity behaviour including the temperature dependence of the surface state energy positions.

surface state [108]. To model the behaviour of SHG intensity showed in Fig. 5.5 b) we used the temperature dependent binding energy of SS by applying a shift of 0.03 eV. Due to lack of measurements concerning energy positions of the surface states in Fig. 5.4 we use in the model the data from Ref. [96]. The result of the model shown in Fig. 5.5 b) agrees qualitatively with the observed behaviour in Fig. 4.5 that at low temperature the SHG intensity rises at an earlier coverage than at room temperature. The model calculation of SS to Cs state transition at room temperature gives a broad contribution to SHG intensity with maximum at 0.07 ML which corresponds to the maximum in the 2PPE data in Fig. 4.5 b). For more precise modelling concerning the width of the Cs state, the results in Ref. [101] should be taken into account.

   In the following the contribution in SHG from optical transitions from the d-bands to the n=1 IP state and to n=2 IP state are considered. The optical transitions through a virtual intermediate state at low temperature are negligible because the lifetime of an electron in the virtual state is extremely short and consequently the transition probability through such state is low. In other words we do not expect a contribution to SHG intensity at low temperature for the data presented in Fig. 4.5 a). The situation can be significantly

different at room temperature since indirect transitions start to play a noticeable role for the data shown in Fig. 4.5 b). Such indirect transitions as reported in Ref. [112] mediated by electron-phonon interaction can change the final-state electron wave vector from $\Gamma$ point to anywhere with in the Brillouin zone. Therefore indirect transitions from the $d$-bands to the n=1 or n=2 IP state could contribute to the SHG signals. From the energy schema in Fig. 5.4 the relevant Cs coverage range for different optical transitions is shown in Fig. 5.6.
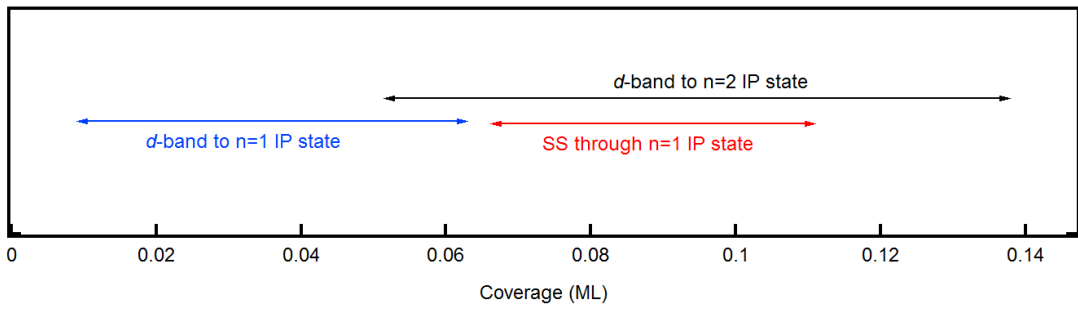


Figure 5.6:   The relevant Cs coverage range for optical transitions presented in Fig. 5.4.

On the surface of Cs/Cu(111), the high mobility of Cs atoms on the surface [110, 113] is supporting an increase of phonon mediated indirect transitions with increasing Cs coverage. From that point of view the transition marked as $d$-band to n=2 IP in Fig. 5.6 should give detectable contribution to the SHG intensity. A model calculation of the electron-phonon coupling in Cs/Cu(111) [114] shows phonon dispersion and clearly for the high $k_\parallel$ in Cu(111) at low temperature the phonon mediated indirect transitions is not supported in comparison to room temperature. Additionally the increase of phonon density of states of Cs/Cu(111) in comparison to Cu(111) is shown.

To conclude the deviation between the 2PPE and SHG as shown in Fig. 4.5 leads to investigation of possible contributions from the surface states in Fig. 5.4 to the SHG intensity. A calculation based on the model described in Eqn. 5.3 suggests that the SS to n=1 IP state optical transition is responsible for the observed discrepancy between 2PPE and SHG maximum position. Temperature dependent shift of the Cu(111) Shockley surface state in energy toward the Fermi level [106–109] is included in the model and gives rise to a clear shift of the maximum in the SHG signal toward the lower Cs thickness as shown in Fig. 5.5 b). This result is in qualitative agreement with the experimental results shown in Fig. 4.5. In addition, temperature induced indirect optical transitions at high $k_\parallel$ are suggested to give additional contribution to the SHG intensity.

## 5.2   QW states in Fe film on Ag(001)

### 5.2.1   Electronic structure of the surface region via 2PPE and SHG

The combination of 2PPE spectroscopy together with SHG as shown in previous section provides detailed information about the electronic structure near the surface region. In Fig. 4.8 simultaneously recorded 2PPE and SHG spectra during iron deposition show the adsorbate induced response of the system. The investigations of iron films grown on silver surfaces [115, 116] have shown an intriguing thickness-dependent oscillatory magnetic anisotropy. This behaviour was attributed to the formation of quantum well states. In this section we will analyse the 2PPE and SHG in an attempt to probe those quantum well states and to understand the early stage of iron deposition.

Before going into the details of quantum well state formation and the physics behind of this process let us consider the surface analysis provided by SHG and 2PPR spectra. The sub-monolayer sensitivity of SHG allows to understand the very first stage of adsorption process. In Fig. 4.8 a) and b) we see a strong decrease of SHG intensity, next to the line marking the beginning of deposition. The signal from surface decreases as surface exposure to the adsorbate increases. This can be qualitatively understood in terms of the fact that the nearly free electrons of metal substrate dominate the surface nonlinearity Sec. 2.2 and the adsorption tends to localize the free electrons in the chemisorption bond reducing the nonlinearity [80, 117]. The response of surface states to the presence of adsorbate can provide an information of a adsorbate-surface interaction. In Ag(001) the occupied surface at $\bar{\mathrm{X}}$ point and the image potential states supposed to play considerable role in the process of surface second harmonic generation. Taking into consideration Eqn. 5.3 we can immediately get insight of the physics of the SHG signal decrease in Fig. 4.8 a). The model predicts that SHG intensity will decrease if the occupied surface state moves upward in energy or if the separation energy between states $a$ and $b$ moves away from resonance with photon energy. In Fig. 4.8 we see sharp change of work function in the very early deposition stage between 0 and 0.5 ML. The value of this change is estimated to be 0.2 eV. The change of work function is combined with lowering of vacuum level and in result the energy down shift of image potential states. This will definitely influence the above mentioned resonant condition in Eqn. 5.3 and as a result lead to decrease of SHG intensity observed in Fig. 4.8 a). The values of work function for clean silver are estimated to be 4.35 eV which corresponds well to literature values [118]. An additional process that causes the intensity drop of SHG in the beginning of the deposition is proposed to be the surface state upward shift during iron adsorption. This SS upward shift as proposed in [103] can

be explained by lateral confinement of the surface state electrons. Such effect can be caused by introducing abrupt barriers in the surface potential reported in Ref. [119, 120]. In the literature [121–124] the formation of Fe clusters and three dimensional islands in low coverage region up to one monolayer support the process of abrupt barriers formation.

Lack of clear oscillatory behaviour in the SHG signal during iron deposition as well as no clear oscillatory behaviour in the 2PPE intensity (Fig. 4.8) leads to the obvious conclusion that the only quantum well state formation takes place in the initial state region as observed in Fig. 4.6 and is discussed in the following section.

## 5.2.2   Origin of QW states via 1PPE

As described in result chapter Sec. 4.2 at around 4 ML thickness in Fig. 4.8 there is an increase in both $p$ and $s$-polarized 2PPE intensity. To understand the origin of this intensity increase as shown in Fig. 4.6 we performed one-photon photoemission (1PPE) experiments on Fe films grown on Ag(001). In Fig. 4.6 we observe intensity oscillations near the Fermi level at around 5.9 eV on the final state energy scale. According to the literature [125] such intensity oscillations with repeatable period are attributed to the quantum well state formation (QWS). More detailed discussion about origin of the oscillations in 1PPE intensity assigned to the formation of QWS in iron film overlayer, will be presented in the further part of this chapter. In contrast to 2PPE we do not observe in 1PPE the intensity increase around 4.9 eV which is attributed to the inter-band transition from the initial state 1 eV below the Fermi level to the unoccupied intermediate state. As shown in Fig. 4.8 b), the increased intensity in SHG in the thickness range starting from 2 ML we connect directly to the 2PPE inter-band transition mentioned above. The absence of clear oscillatory 2PPE intensity implies that the quantum well state formation takes place only in the initial state region observed in 1PPE as shown in Fig. 4.6 and is analyzed in more detail in Fig. 5.7.

In Fig. 5.7 we see the intensity oscillations by the thickness line profiles at 5.9 eV and 5.8 eV. The period of oscillation $\approx$4.5 ML provides insight into the formation of the QWS, namely the quantization of the crystal momentum $k \perp$ that is perpendicular to the interfaces of the film.

The wave function of a quantum well state, as described in Ref. [92, 126], consists of a rapidly oscillating Bloch function, which is modulated by an envelope function. The Bloch function is derived from the bulk band whereas the envelope function comes from the boundary conditions due to the interfaces. Since the envelope function is simply a beating pattern between the Bloch function and the period of the lattice planes perpendicular to the interfaces, we can derive the Bloch wave vector ($k_{t}ot$) of the Bloch function by:
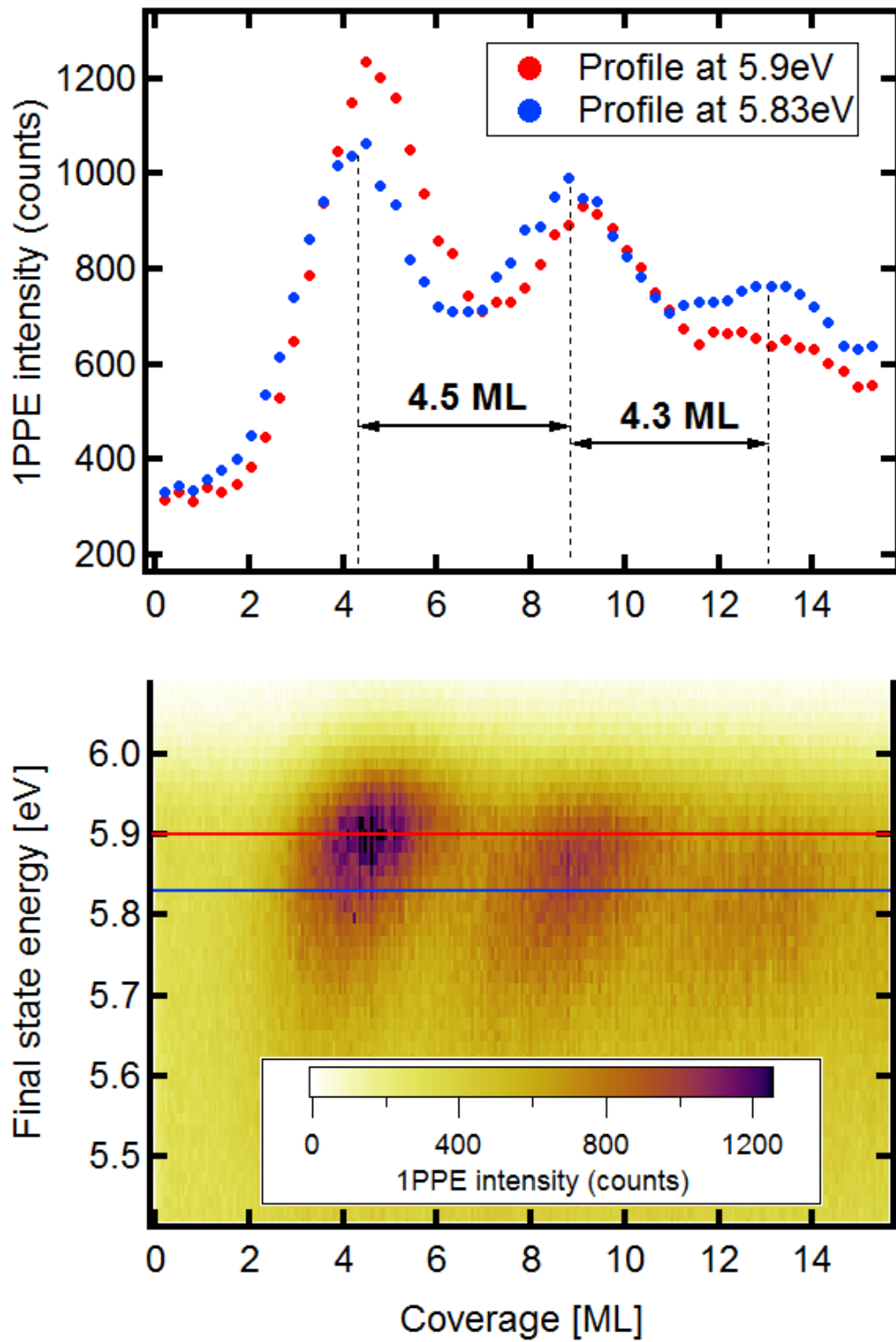
Figure 5.7: The line profile at 5.9 eV and 5.83 eV shows the oscillatory behaviour of 1PPE intensity as a function of Fe coverage.

$$k_{tot} = k_{edge} \pm k_{env}. \tag{5.4}$$

The interfaces confining the quantum well state are expected to cause interference of the electron wave functions with period $p = \lambda_{env}/2$. Thus, one obtains $k_{env} = 2\pi/\lambda_{env} = \pi/p$. This allows us to determine the wave vector $k_{env}$ of the envelope function from the period of intensity oscillations. The band-edge wave vector $k_{edge}$ corresponds to the zone-boundary wave vector $k_{ZB} = \pi/d$ where $d$ is the layer spacing in the iron thin film. The simple relation between the oscillation period and band wave vector k is expressed by Eqn 5.5.

$$k = 1 - 1/p. \tag{5.5}$$

with $k$ in units of $k_{ZB}$ and $p$ in monolayers. This simple relation allows to calculate the Bloch wave vector of the band that is quantized into the quantum well state at the Fermi level and we obtain a value of $k = k_F/k_{ZB} = 0.78$ and the Fermi wave vector of this band is $k_F =$1.7 Å$^{-1}$, representing the value of $k \perp$ at which we expect the quantum well state to cross the Fermi level. In Fig. 5.8 the electronic band structures of bulk iron and silver are shown [127, 128]. The black arrow at the Fermi level indicates the Fermi wave vector $k_F$ derived above.

The theoretical values of the Fermi wave vector of the relevant majority $d$-bands for the QWS are summarized in Tab. 5.1.

| Band Symmetry | Schäfer [129] | Wang [130] | Yates [131] | Yao [132] | Crangle [133] |
|:---:|:---:|:---:|:---:|:---:|:---:|
| $k_F$ for $\Delta_{2'}$ | 1.9 | 1.93 | 1.94 | 1.91 | 1.77 |
| $k_F$ for $\Delta_5$ | 2.0 | 2.0 | 2.0 | 2.0 | 1.98 |

Table 5.1: The values of $k_F$ at which $\Delta_{2'}$, $\Delta_5$ bands cross the Fermi level [127, 129–133] along the $\Gamma - H$ direction. All values are in Å$^{-1}$.

As suggested in Ref. [8, 92, 126] the formation of quantum well states due to reflection of wave function at the interfaces requires presence of a gap in the electronic band structure of the substrate. The intensity oscillations observed at 0.1 eV below the Fermi level in the 1PPE as shown in Fig. 5.7, limit the energy region in the electronic band structure shown in Fig. 5.8, at which the QWS are expected to form. Absence of $\Delta_{2'}$ and $\Delta_5$ symmetry bands in silver in region beyond 4 eV below Fermi level could provide good reflectivity at the silver-iron interface for the electrons in iron $d$ states. Since in normal emission geometry the transition from $\Delta_{2'}$ is forbidden for $s$ and $p$ polarized light,-according to
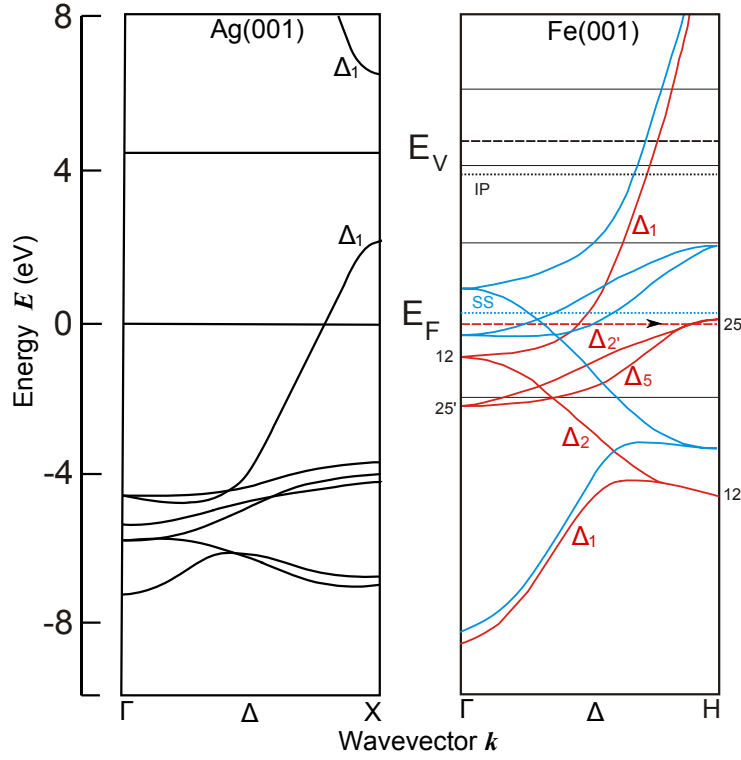
Figure 5.8:   The electronic band structure along $\Delta$ direction of silver [128] and iron [127]

the dipole selection rules [134–137], the quantum well states observed in Fig. 4.6 and in Fig. 5.7 are attributed to electrons in $\Delta_5$ symmetry band in iron. The Tab. 5.2 summarizes the discussed above dipole selection rules.

We measured the 1PPE spectra during iron deposition with $s$ and $p$ polarization light as shown in Fig. 4.7, to further support experimentally the $\Delta_5$ symmetry character of the quantum well states observed in Fig. 4.6 . Observed in both $s-$ and $p-$ polarized spectrum intensity increase near the Fermi level at around $4\,$ML, confirms the $\Delta_5$ symmetry character of the initial states in agreement to the dipole selection rules in Tab. 5.2. In Fig. 5.9 the thickness line profiles at $5.9\,$eV from Fig. 4.7 and Fig. 4.8 are shown. The direct comparison of the intensity increase at Fermi level in 2PPE and 1PPE spectra, associates the intensity increase at $5.9\,$eV in 2PPE to the same quantum well state ob-

|             | Symmetry      | Orbit         | Polarization   |
|-------------|---------------|---------------|----------------|
| Final state | $\Delta_1$    | $s$, $p_z$, $d_{z^2}$ |        |
| Initial state | $\Delta_{2'}$ | $d_{xy}$    | forb.          |
|             | $\Delta_5$    | $p_x$, $d_{xz}$ | $s(A \parallel x)$. |
|             | $\Delta_5$    | $p_y$, $d_{yz}$ | $s(A \parallel y)$. |

Table 5.2:   Non-relativistic dipole selection rules for cubic systems in normal emission [135]

served at the same thickness in 1PPE. The lower intensity of the s-polarized 2PPE can be explained that the intermediate electronic states between the Fermi and vacuum level are of $\Delta_1$ symmetry character and cannot be probed by s-polarized light according to the dipole selection rules in Tab. 5.2. The p-polarized 2PPE spectra show maximum which is shifted with respect to the 1PPE maximum. This shift can also be attributed to 2PPE transitions through the intermediate states. Moreover the 2PPE p-polarized spectrum measured at room temperature in Fig. 5.9 a) shows a broad intensity maximum between 3 to 5 ML and may be related to the silver segregation on top of the iron film during the growth [89]. Control over the segregation process is important since the segregation can have an influence on the interface which is critical for the formation of the quantum well states [138].

The damping of the intensity oscillations at Fermi level toward higher Fe coverage is observed in Fig. 4.6. This effect was observed in literature and in case of Fe on Ag(001) as reported in Ref. [92] could be attributed to the degradation of the film quality, finite energy resolution which makes it harder to separate the QWS when their spacing becomes smaller in thicker films, and the mean free path of the electrons in the QWS. The degradation of the film quality is attributed to the accumulated amount of impurities from long sequence of evaporations and to the roughness of the film [89]. The deposition at low temperature ($160\,\mathrm{K}$) was expected to drastically limit the intermixing, at the expanse of the poor morphological quality of the film [139]. The mean free path of electrons in the $d$-bands is usually short [140] due to their small group velocity of the flat energy-momentum dispersion and their short lifetime due to strong Auger decay. Consequently quantum well states derived from the $d$-bands should diminish when the film thickness becomes larger than the mean free path.

The binding energy of QWS as a function of the Fe film thickness measured in 1PPE is discussed with use of the phase accumulation model. The phase accumulation model was used extensively in the literature [138, 141–146] for the analysis and interpretation of the quantum well states. It is based on the idea of plane wave propagating inside the quantum well. As the plane wave reaches the substrate-overlayer or overlayer-vacuum interface of the film, it is reflected with the additional phase: $\Phi_C$ for the substrate-overlayer reflection and $\Phi_B$ for the overlayer-vacuum reflection. After the plane wave has been reflected at both interfaces it can undergo constructive or destructive interference with itself. For the constructive interference the total accumulated phase must be an integer multiple of $2\pi$. In this case a standing wave solution corresponding to a bound state takes place. The mathematical equation with the condition for the formation of a standing wave corresponds to the Bohr-Sommerfeld quantization rule:
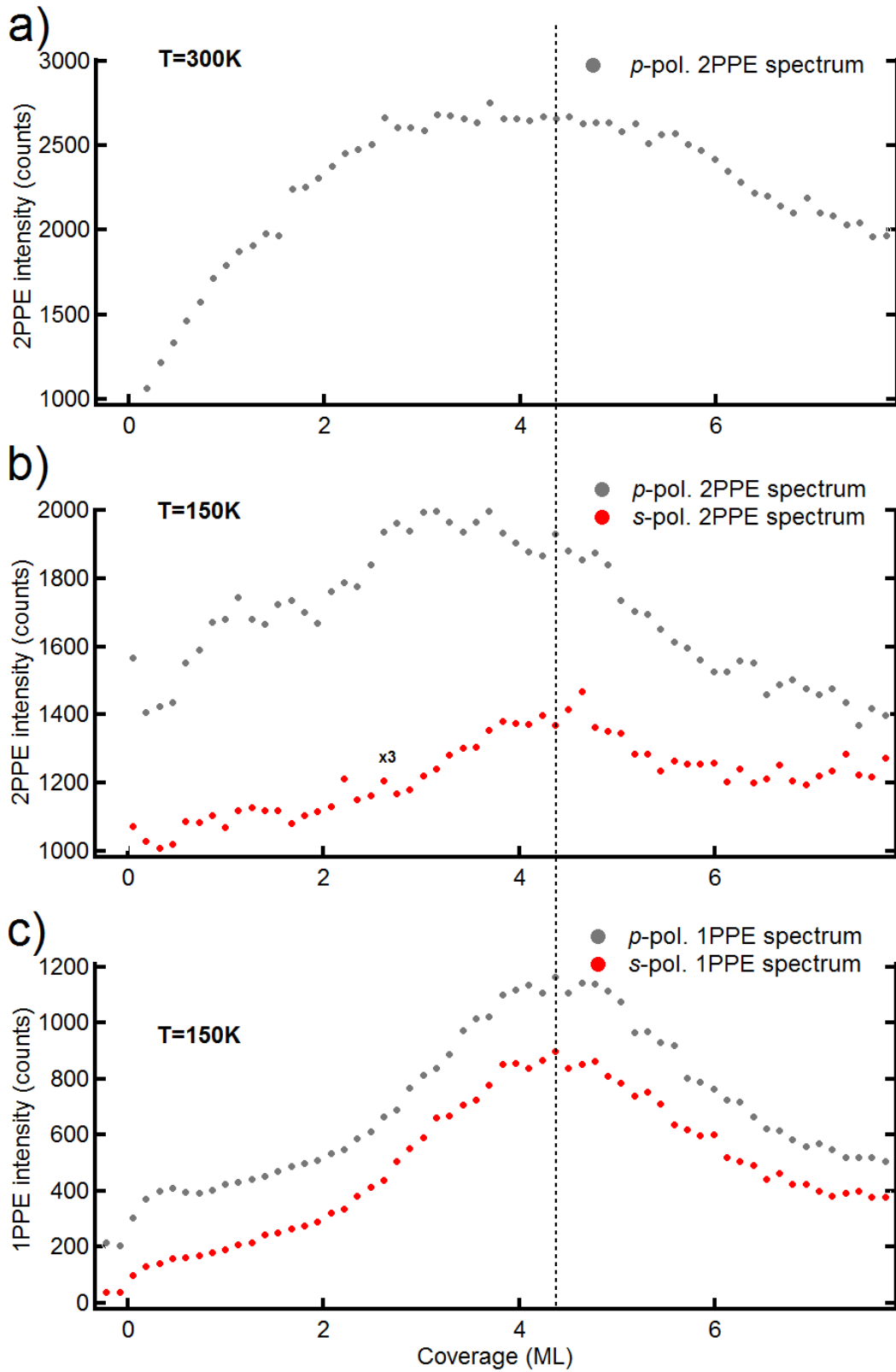
Figure 5.9: The line profiles at 5.9 eV from Fig. 4.7 and Fig. 4.8: a) *p*-polarized 2PPE at room temperature T=300 K, b) *p* and *s*-polarized 2PPE at low temperature T=150 K, c) *p* and *s*-polarized 1PPE at low temperature T=150 K

$$\Phi_B + \Phi_C + 2kd = 2\pi n. \tag{5.6}$$

where $\Phi_C$ and $\Phi_B$ are the phase shifts related to the reflections at the substrate-overlayer interface (barrier) and at the overlayer-vacuum interface respectively and $k$ is the wave vector of the electron modelled by a plane wave propagating in an overlayer of thickness $d$. To generate $\Phi_B$ an expression from Ref. [144] based on the Wentzel-Kramers-Brillouin (WKB) approximation [147] is used:

$$\Phi_B = \pi \left( \sqrt{\frac{3.4eV}{E_V^* - E}} - 1 \right). \tag{5.7}$$

where $E_V^*$ is the vacuum level of the overlayer and $E$ the electron energy measured from the bottom of inner potential. To generate $\Phi_C$ we use the empirical formula [148]:

$$\Phi_C = 2arcsin\sqrt{\frac{(E - E_L)}{(E_U - E_L)}} - \pi. \tag{5.8}$$

where $E_U$ and $E_L$ are the energies of the upper and lower edges of the band gap in the substrate. The quantum well states formed in the iron films are of $\Delta_5$ symmetry character. There is no band gap in silver in the energy region where $\Delta_5$ band in iron exists but only a symmetry gap in which bands with $\Delta_5$ symmetry are absent (Fig. 5.8). This is why the phase shift $\Phi_C$ values, the energies $E_L$ and $E_U$ are not well defined. To obtain best fit of experimental data in Fig. 4.6 we chose those quantities. The bulk band dispersion $k(E)$ dependence that enters in the term $2kd$ in Eqn. 5.6 was fitted from the calculated band structure in Ref. [127].

In addition the experimentally determined Fermi wave vector $(1.7\,\text{Å}^{-1})$ deviates considerably from the theoretically calculated values (Tab. 5.1). In Ref. [129] a combined study of angle-resolved photoemission with density functional calculations shows discrepancy between measured and the calculated $k_F$ value of $\Delta_2^{'}$ symmetry band. The experimentally obtained value in Ref. [129] is smaller than the theoretical value summarized in Tab. 5.1. To fit the experimental data in Fig. 4.6 with phase accumulation model we shift the calculated $\Delta_5$ band from Ref. [127] upwards in energy by 0.16 eV as shown in Fig. 5.10. The upward energy shift causes a decrease of $k_F$ value as shown in Fig. 5.10. The discrepancy in Ref. [129] disscussed above is a major reason justifying band energy shift presented in Fig. 5.10.
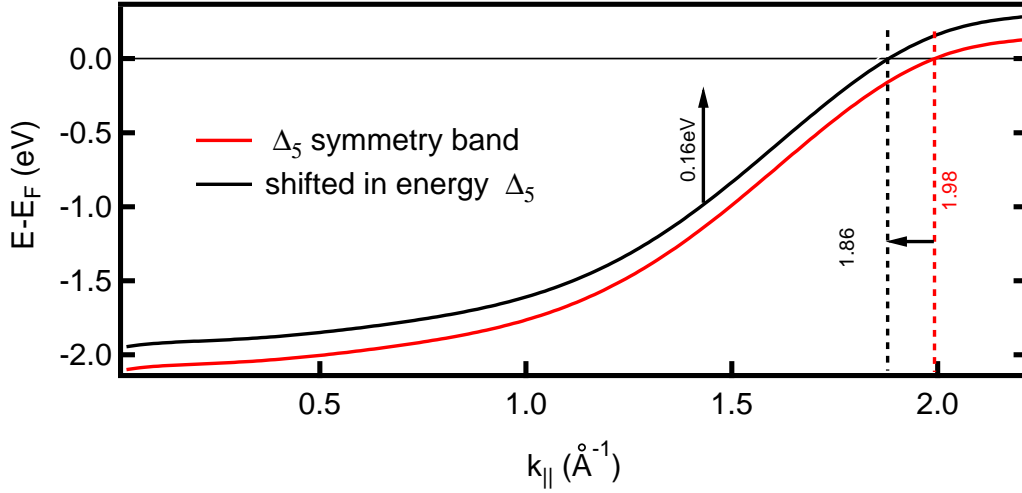
Figure 5.10:   Artificial shift of the majority $\Delta_5$ band from the theoretical calculation in Ref. [127] in order to fit the experimentally observed data in Fig. 5.11

This energy shift is related to the binding energy shift. The binding energy shifts due to the different structure of the thin film as compared to the bulk. It is known [149, 150] that the bulk interlayer spacing compared to the surface interlayer spacing is contracted. For (001) surface this contraction is generally estimated to be in range of 3%. It is known that the increased roughness of the film is caused by the low temperature growth [89]. The increased roughness as reported in Ref. [151] is causing the increased interlayer distance compression in the direction perpendicular to the surface. If the interlayer distance of the iron film is compressed compared to iron bulk interlayer distance. We can expect a shift in binding energy of all states in the film in comparison to a bulk case. The perpendicular to surface contraction is connected with in-plane expansion. When the lattice is expanded parallel to the surface, the overlap between the $d$ electrons on neighbouring metal atoms become smaller, the bandwidth decreases and to keep the $d$ occupancy fixed, the d states move upwards in energy [152]. This additionally supports the observed upward energy shift. However because of the small 0.8% lattice misfit the above argument should be treated with caution.

The solution of phase accumulation model calculation is presented in Fig. 5.11. The red solid points represent the estimated dispersion of the quantum well states in iron film. The values of subsequent variables used in phase accumulation model are: $E_V^*$ is set to 4.1 eV (vacuum level in experiment), $E_U$ is set to 2 eV and $E_L$ is set to -4 eV according to the top and bottom edges of the $sp$- band in silver. In comparison to previous photoemission studies of Fe film grown on Ag(001) [115], the quantum well states exist only in the region near the Fermi level and disappear for electron energy below 0.1 eV. Our
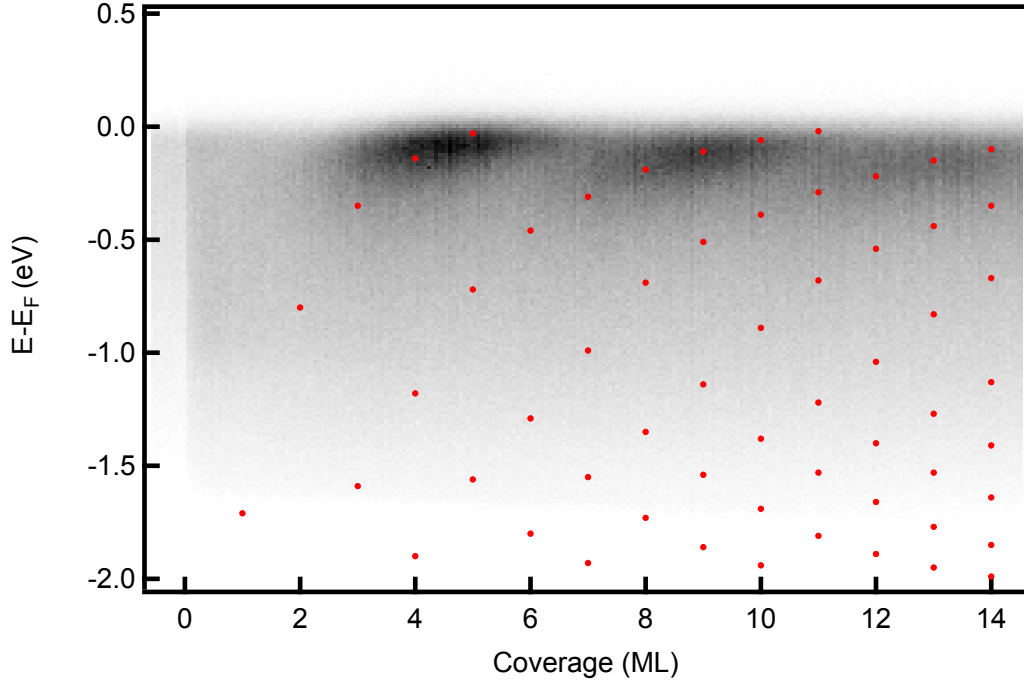
Figure 5.11:   The 2PPE spectrum with the corresponding estimation of the dispersion of quantum well states on the basis of the phase accumulation model (red points).

measurements performed during low temperature iron film growth provide very similar observation described in Ref. [115]. The phase accumulation model allows to predict the model dispersion of quantum well states in a single particle picture.

Furthermore, we would like to identify the spin-polarization that could be related to the QWS. Fig. 4.9 shows the spin-polarized 1PPE spectra for 9 ML and 11.5 ML of iron film. The average spin-polarization in the 1PPE spectra is about 37%, what is in agreement with the literature values for bulk iron [153, 154]. Both 9 ML and 11.5 ML thickness shown in Fig. 5.12 are above the spin reorientation transition [155, 156]. Form spin-polarized 1PPE spectra we are able to identify the majority character of the quantum well state.

At 9 ML coverage shown is Fig. 4.9 a), corresponding to the thickness where quantum well state is formed, we measure the in-plane spin-polarization of the 1PPE spectrum and compare it to the in-plane spin polarization of the 1PPE spectrum for 11.5 ML where the quantum well state is not formed Fig. 4.9b). Although we can observe a clear difference in 1PPE intensities at the Fermi level due to the QWS formation, no significant change in the spin-polarization is found within the statistical uncertainty of about 5%.

Conclusion: We observe oscillatory photoemission intensity at the Fermi level in 1PPE and attribute it to the formation of quantum well states from the occupied majority $\Delta_5$ band in the iron film. From spin-resolved photoemission we identify the majority character
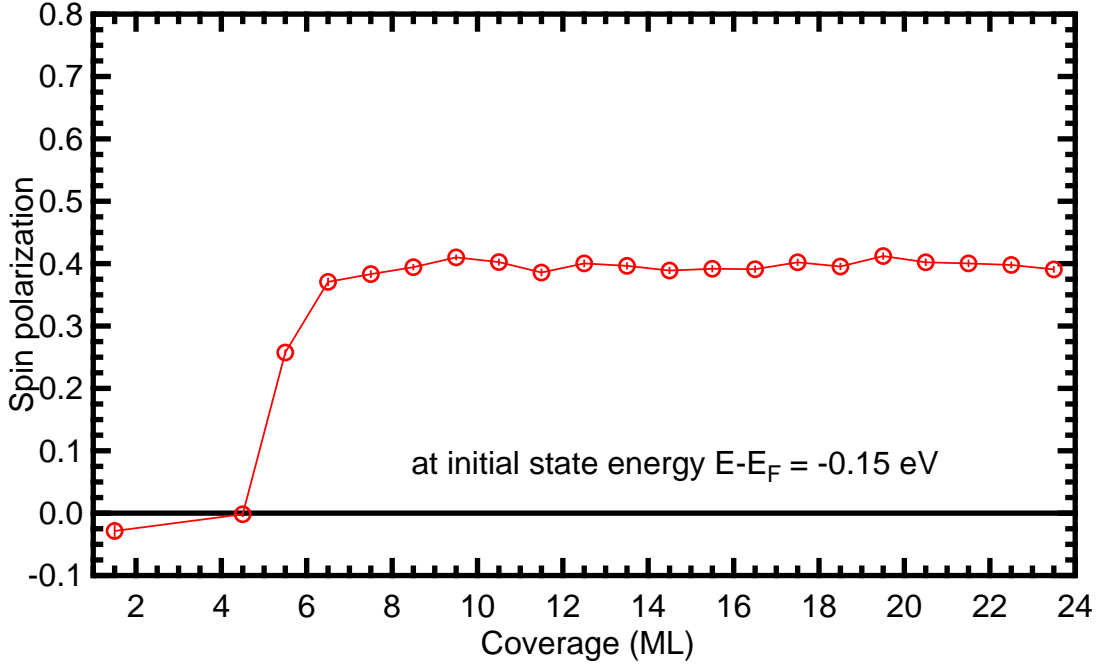
Figure 5.12:   Thickness dependence of the in-plane spin-polarization measured in 1PPE at initial state energy 0.15 eV below the Fermi level.

of the quantum well state. However no significant change in spin-polarization related to the formation of the quantum well states could be detected within the accuracy of our experiment. We used phase accumulation model to explain the observed oscillation and to predict the model dispersion of quantum well states in the single particle picture.

## 5.3   Image potential resonance on clean and oxidized Fe/Ag(001)

In the previous subsection we mentioned the influence of sample preparation on the film quality which can affect the surface electronic structure of the Fe film on Ag(001). This is especially important for the well-known image potential (IP) states [157–159], originating from electrons near the vacuum level, trapped in front of the metal surface where the gap of the projected bulk bands occurs. In this case the reflectivity for energies within the band gap prevents electrons from decaying into the bulk, and the long-range bounding potential is formed by Coulombic attraction between the electron in the vacuum and its image charge in the solid [160]. As the IP states have their dominant part of wave function near and in front of the surface, they are sensitive to any change at the surface [87] like e. g. the gas adsorption. The formation of the IP state can be well explained by the phase accumulation model that we used in Sec. 5.2 for the quantum well states [161]. In

Fig. 5.13 the graphical solution of the phase accumulation model for the clean Ag(001) surface gives an estimation of the binding energy of the $n = 1$ image potential state with respect to the vacuum level. The binding energy estimated from Fig. 5.13 is equal to $E - E_V = $ -0.52 eV and matches the literature values in Tab. 5.3.
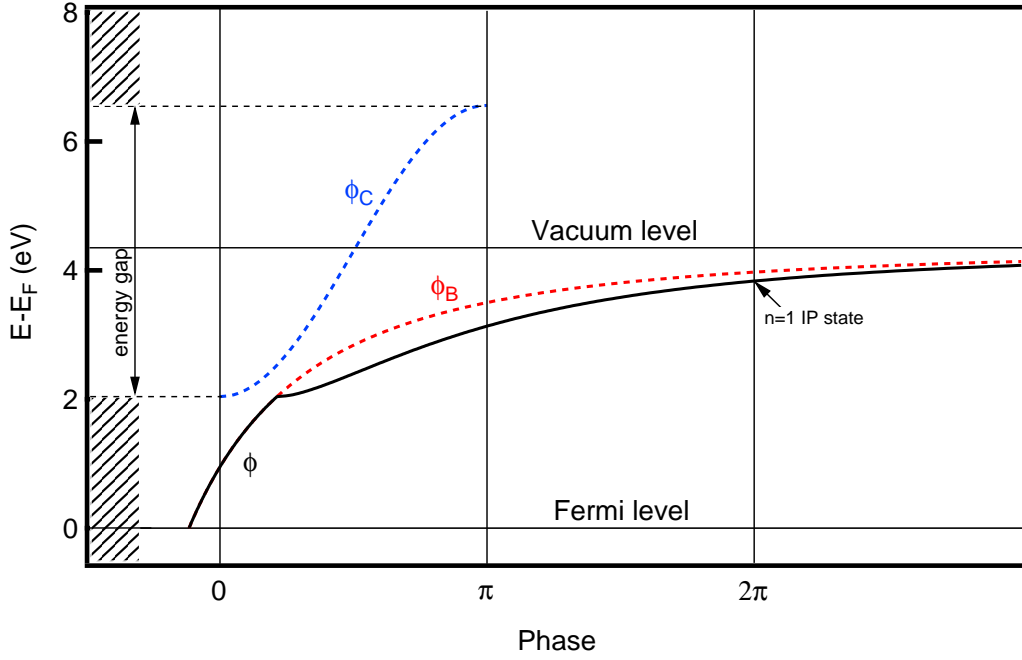


Figure 5.13:   The graphical solution of the phase accumulation model for Ag(001). The phase shifts upon reflection on the surface barrier ($\Phi_B$), the Ag bulk crystal ($\Phi_C$) and the total phase $\Phi$ showing the $n = 1$ image potential state (IP) binding energy.

The phases from the reflection at the IP barrier and at the crystal side $\Phi_B$ and $\Phi_C$ in Fig. 5.13 are introduced in Sec 5.2. The value of work function is estimated from our photoemission spectrum of clean Ag(001) as 4.35 eV. The lower edge of the Ag(001) band gap taken from Ref. [128] is 2.04 eV and the upper band gap edge is 6.56 eV.

The electron in the IP state is trapped in the direction perpendicular to the surface, but in the direction parallel to the surface its motion is close to the near-free electron and its energy-momentum dispersion can be described by equation Eqn. 2.8.

| Calculated values | Giesen [162] | Z. Li [163] | Fauster [164] | this work |
|---|---|---|---|---|
| Effective mass | 0.95 | 1.03 | 1.0 | 0.96 |
| Binding energy | -0.53 | -0.548 | -0.529 | -0.52 |

Table 5.3:   Calculated electron effective masses (in free electron mass units $m^*/m$) and binding energies (in respect to vacuum level in $eV$) for the $n = 1$ image potential state on Ag(001)

The free electron-like behaviour in direction parallel to the surface requires an introduction of a a single parameter called effective mass $m^*$, which can differ from the value of the rest mass of an electron $m_e$. The important point here is that the electron in a periodic potential is accelerated relative to the lattice in applied electric or magnetic field as if its mass is equal to an effective mass $m^*$. The effective mass of IP state can depend strongly on its relative position to the substrate band gap [165, 166].

Image potential states near the top edge of the gap have an effective mass $m^*/m_e > 1$ and states near to the bottom of the gap have $m^*/m_e < 1$. Whereas image potential states near the middle of the gap, have $m^*/m_e \cong 1$. In case of Ag(001) the vacuum level is close in energy to the middle of the energy gap. The image potential states which are formed in the vicinity of vacuum level should have an effective mass close to the free electron value $m_e$. To estimate the effective mass $(m^*)$ of the $n = 1$ image potential state on Ag(001) we will apply the method presented for Cu(001) in Ref. [162].

The Rydberg-series-like IP states predicted for $n \geqq 1$ span only in a very narrow range of energy [167]. The binding energy of individual IP state $E_B$ can be derived from:

$$E_B = 0.85 eV/(n + a)^2 \tag{5.9}$$
$$a = \frac{1}{2}(1 - \Phi_C/\pi).$$

where $a$ is a parameter called quantum defect, related to phase shift in the reflection of an electron in the IP state from the substrate band gap [168]. The $\Phi_C$ varies from 0 to $\pi$ in the whole energy range within the band gap as shown in Fig. 5.13, leading to a possible value of binding energy $(E_B)$ of the $n = 1$ IP state from -0.38 eV to -0.85 eV in respect to the vacuum level. The solution closest to the vacuum level will lay in energy near to the middle of the energy gap and such IP state should obey free electron dispersion with effective mass $m^*/m_e \cong 1$.

As shown in Fig. 5.14 the IP state with binding energy $E_{B1}$ of -0.38 eV will disperse (red dashed line) following $m^*/m_e \cong 1$ behaviour and eventually at some point $E_C$ it will cross the extrapolated bottom band edge dispersion curve as shown in Fig. 5.14. The Ag(001) $n = 1$ image potential state binding energy estimated by use of phase accumulation model for $E_{B2}$=-0.52 eV lies below the middle of the gap and should have $m^*/m_e < 1$. To estimate the value of the effective mass of the $n = 1$ image potential state in Ag(001) we use Eqn. 5.10 introduced in Ref. [162].

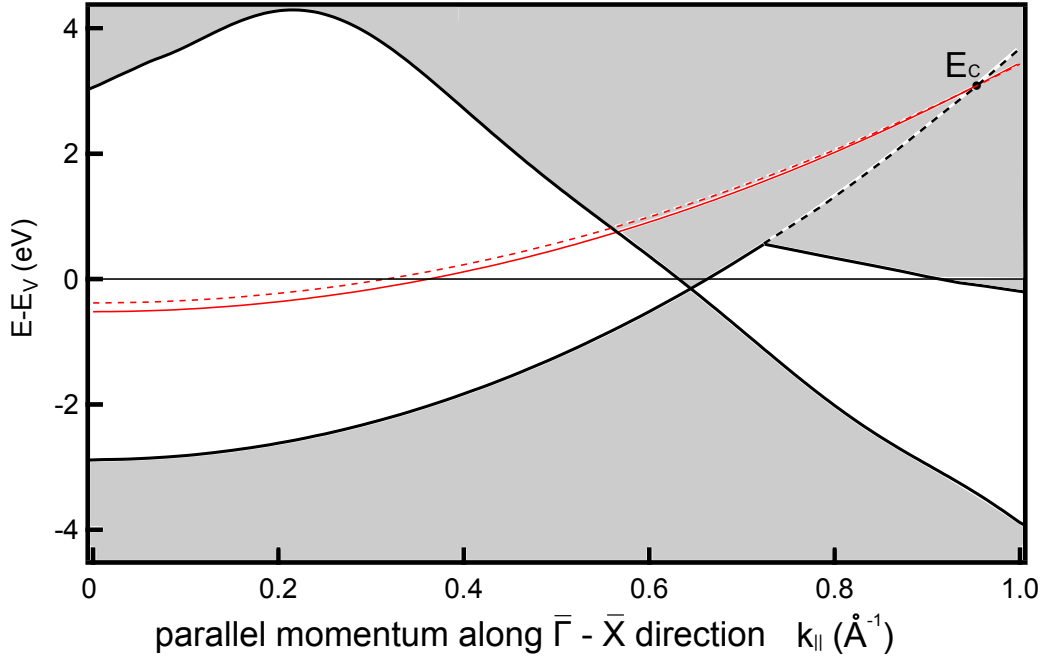$$\frac{m^*}{m_e} = \frac{E_C - E_{B1}}{E_C - E_{B2}} \tag{5.10}$$

Figure 5.14: Surface projected band structure on Ag(001) [163]. The red curve represents the estimated dispersion of the of $n = 1$ image potential resonance. The dashed line curve represents free electron dispersion (details in text).

The estimated value of effective mass for $n = 1$ image potential state in Ag(001) from Eqn. 5.10 where $E_C = 3$ eV is found to be $m^*/m_e = 0.96$.

Fig. 4.10 shows the dispersion of the IP state in the photoemission spectra on the clean Ag(001), where we obtain the energy dispersion versus the momentum parallel to the surface $E(k_{\parallel})$ of the $n = 1$ image potential state as shown in Fig. 5.15.

The experimentally measured binding energy $E_B=0.5$ eV $\pm$ 0.1 and the effective mass $m^*=0.95\,m_e\pm$ 0.15 for the $n = 1$ image potential state on Ag(001) are in good agreement with literature values recently reviewed in Ref. [169] and summarized in Tab. 5.4.

Fig. 4.11 and Fig. 4.12 shows angle-resolved photoemission spectra measured on Fe on Ag(001) and oxidized Fe on Ag(001). The dispersion of the n=1 IP state is extracted and shown in Fig. 5.15. From the dispersion of the $n = 1$ image potential state on Fe/Ag(001)

|  | Reihl [170] | Goldman [167] | Giesen [162] | Ferrini [160] | this work |
|---|---|---|---|---|---|
| Effective mass | 1.6 ± 0.3 | 1.02 ± 0.2 | 1.15 ± 0.1 | 0.97 ± 0.02 | 0.95 ± 0.15 |
| Binding energy | -0.5 ± 0.4 | -0.5 ± 0.2 | -0.53 ± 0.2 | -0.53 ± 0.1 | -0.5 ± 0.1 |

Table 5.4: Experimentally obtained values of electron effective masses (in free electron mass units $m^*/m$) and binding energies (in respect to vacuum level) in $eV$ for the Ag(001) $n = 1$ image potential state on Ag(001)
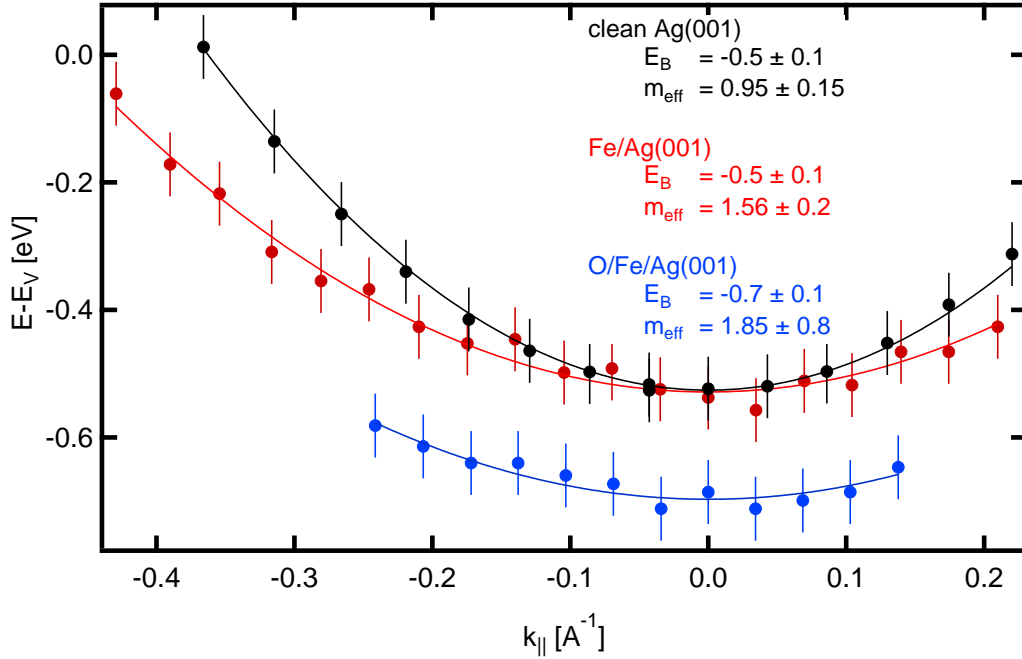
Figure 5.15: Binding energy of the n=1 IP states with respect to the vacuum level $(E - E_V)$ and its dispersion versus the parallel momentum $(k_{||})$.

in Fig. 5.15, we obtained the binding energy $E_B$=-0.5 eV $\pm$ 0.1 and the effective mass $m^*$=1.56 $m_e\pm$ 0.2. There is no data are available for the dispersion of image potential state in Fe(001). In our experiments, the binding energy of the $n = 1$ image potential state on Fe on Ag(001) and on clean Ag(001) are similar whereas the effective mass values differ significantly.

This difference is probably caused by the lack of energy gap near vacuum level in Fe(001) band structure as shown in Fig. 5.8. In the absence of the energy gap, there is no well-defined reflection as well as phase shift $(\Phi_C)$ for the electron trapped in the image potential. The electron can penetrate into the interior of the Fe film with its wave function hybridized with the sp-electrons at the same energy. This explains qualitatively the observed increase of the effective mass in comparison to the Ag(001) as shown in Fig. 5.15. Due to the absence of the energy gap in Fe(001) it is suspected that the IP state becomes IP resonance as pointed out in Ref. [171] and as such will be used in description below.

In Fig. 4.13 the 2PPE spectrum of Fe films on Ag(001) is shown with the work function change of +0.1 eV upon oxidation as shown in Fig. 4.12. This change in the work function affects the $n = 1$ image potential state dispersion [172]. The measured binding energy $E_B$=-0.7 eV $\pm$ 0.1 and effective mass $m^*$=1.85 $m_e\pm$ 0.8 Fig. 5.15 are higher than the values on Fe on Ag(001).

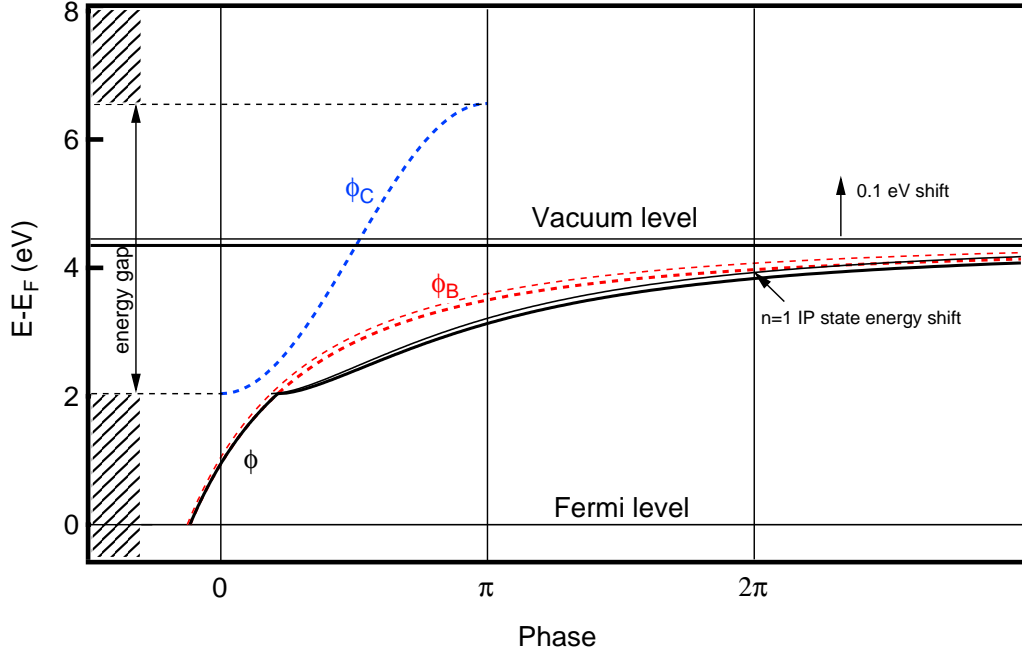The change in the binding energy might be related to the change in the work function

Figure 5.16:   Model assumption with the change of the surface potential barrier upon oxidation. Energy variation of the phases $\Phi_B$, $\Phi_C$ and $\Phi$ showing the $n = 1$ image potential state (IP) binding energy change.

of the system since the IP states are bound with respect to the vacuum level. It ise can clearly seen from the Fe bulk band structure in Fig. 5.8, that there is no band gap near the vacuum level where IP states exists. It is therefore difficult to estimate the binding energies and effective mass of the IP resonance above the iron film according to the phase accumulation model, since the $\Phi_C$ parameter is undefined. As the prediction of phase accumulation model depends strongly on the proper determination of $\Phi_C$ and $\Phi_B$, for the general behaviour examination we will apply a 0.1 eV vacuum level shift to the solution presented in Fig. 5.13.

In the following we compare the measured binding energy of IP resonance on clean and oxidized Fe/Ag(001) with the model assumption. First we estimate the binding energy shift due to the increase of surface barrier according to the phase accumulation model. In Fig. 5.16, the vacuum level is shifted upon 0.1 eV due to the oxidation of Fe on Ag(001), in consequence, the phase shift of electron wave function upon reflection from the surface barrier $\Phi_B$ is changed which creates the energy shift of the $n = 1$ image potential state towards the vacuum level (see Fig. 5.16). The estimated value of binding energy increases with respect to vacuum level from -0.52 eV to -0.54 eV and is consistent with the observed binding energy behaviour in Fig. 5.15 for oxidized Fe film on Ag(001).

In addition, modifications at the surface due to oxygen absorption can occur. The image
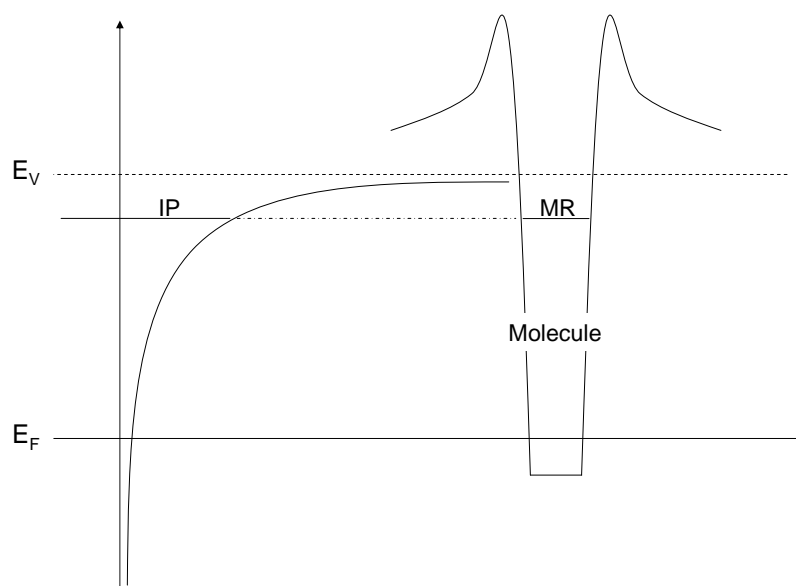
Figure 5.17:   Sketch of the image potential state (IP) in front of the surface and the molecular resonance of adsorbate (MR). To achieve the coupling between (IP) and (MR) the $2\hbar\omega$ pulse excites an electron from occupied states to unoccupied state near vacuum $E_V$.

barrier is not simply scaled to higher energy but its shape is modified. These can also contribute to the observation of different binding energy.

In general the change of the position within the energy gap is responsible for the change of image potential state effective mass due to change in the binding energy [173]. Although there is no energy gap in iron we expect that the effective mass of the image potential resonance will change upon oxidation of Fe/Ag(001) because the change in binding energy should affect the coupling (hybridization) between the electrons in IP resonance and the sp-electrons in iron.

The adsorption of oxygen on iron surfaces was extensively investigated in literature [156, 174–177]. It is well known that oxygen bonding with iron results in hybridization between the oxygen $2p$ and iron $3d$ orbitals at the surface. However we can only speculate about possible hybridization between IP resonance and the oxygen adsorbate. The idea of such hybridization is schematically shown in Fig. 5.17. A similar phenomena was reported in Ref. [178] where author proposed a coupling between the image potential state on Cu(111) and the molecular resonance of $O_2$ adsorbed on top of substrate. Such coupling could be responsible for the experimentally observed increase of the effective mass in Fig. 5.15.

To conclude the discussion in this section we described the binding energy and effective mass of the $n = 1$ image potential state on Ag(001), the image potential resonance on clean and oxidized surfaces of the Fe/Ag(001). We investigated the differences in the effective mass based on the bulk band structure of iron and silver. In addition we examined the differences in the binding energy compared to the phase accumulation model prediction.

## 5.4 Increase of electron lifetime due to QW state formation in Co/Cu(001)

The 2PPE spectra shown in Fig. 4.15 are the result of low and room temperature growth of 7 ML cobalt film on the Cu(001) substrate. The temperature dependent formation of QW states allows a time-resolved investigation at the same amount of deposited cobalt but with a different density of electronic states as shown in Fig. 4.16. The combined SHG and 2PPE measurements shown in Fig. 4.14 allow for a laser pulse shape control at the sample surface without further assumptions.

The upper part of Fig. 4.15 shows the phase-average $(0\omega)$ envelope of 2PPE cross-correlation measured on Co/Cu(001) extracted by integrating the experimental interferometric cross-correlation curves over each optical cycle as described by Nessler [78]:

$$I_{0\omega}(\delta) = \frac{\lambda}{c} \int_{\delta - \frac{\lambda}{2c}}^{\delta + \frac{\lambda}{2c}} I_{I2PC}(\delta) d\delta \qquad (5.11)$$

$$I_{1\omega}(\delta) = \frac{2\lambda}{c} \sqrt{\left( \int_{\delta - \frac{\lambda}{2c}}^{\delta + \frac{\lambda}{2c}} I_{I2PC}(\delta) cos(\omega\delta) d\delta \right)^2 + \left( \int_{\delta - \frac{\lambda}{2c}}^{\delta + \frac{\lambda}{2c}} I_{I2PC}(\delta) sin(\omega\delta) d\delta \right)^2} \qquad (5.12)$$

$$I_{2\omega}(\delta) = \frac{4\lambda}{c} \sqrt{\left( \int_{\delta - \frac{\lambda}{4c}}^{\delta + \frac{\lambda}{4c}} I_{I2PC}(\delta) cos(\omega\delta) d\delta \right)^2 + \left( \int_{\delta - \frac{\lambda}{4c}}^{\delta + \frac{\lambda}{4c}} I_{I2PC}(\delta) sin(\omega\delta) d\delta \right)^2} \qquad (5.13)$$

The increase in the full-width-at-half-maximum (FWHM) of the $0\omega$ envelope in the Fig. 4.15 a), indicates a lifetime effect in the cross-correlation and can be attributed to the lifetime of an unoccupied quantum well state in Co film on Cu(001). We compared the cross-correlation curves measured on Co/Cu(001) deposited at low temperature Fig. 4.15 b) and the FWHM of the $0\omega$ envelope had not shown any increase.

As shown in Sec. 2.1.4 the $0\omega$ envelope includes the information regarding the energy relaxation time of electrons in the unoccupied intermediate state involved in the 2PPE process. Following the analysis procedure described in Ref. [78] we assume an instantaneous response of the material and a Gaussian pulse shape given by $E(t) \propto exp(-4ln2(t/\tau)^2)$ where $\tau$ is the FWHM of the electric field envelope of the laser pulse. Under these assumptions the autocorrelation of the laser pulses on the sample surface is given directly by the interferometric second harmonic generation (SHG) curves which can be decomposed into phase-averaged envelopes by:

$$IAC_{0\omega}(t) \propto e^{-4ln2(\frac{t}{\tau})^2} \tag{5.14}$$

$$IAC_{1\omega}(t) \propto e^{-3ln2(\frac{t}{\tau})^2} \tag{5.15}$$

$$IAC_{2\omega}(t) \propto I_{0\omega} \tag{5.16}$$

In the experimental data presented in Fig. 4.15 a) the optical pulse width $\tau$ is estimated to be 10 fs. In order to quantify the lifetime of the unoccupied quantum well state according to the increase in FWHM of the $0\omega$ envelope of 2PPE, we compared the SHG envelope marked in Fig. 4.15 a) with the 2PPE envelope. To extract the lifetime from the $0\omega$ envelope of 2PPE we applied the method introduced in Ref. [78]. By means of fitting procedure based on convolution of the assumed Gaussian laser pulse with exponential decay $exp(|-t/T|)$ representing the phase and population decays with a time constant T:

$$I_{2\omega}^{fit}(\delta) = c_0^{2\omega} \cdot \int_{-\infty}^{+\infty} e^{-\left|\frac{\delta-t}{T_2^{02}}\right|} \cdot e^{-4ln2\left(\frac{t}{\tau}\right)^2} dt \tag{5.17}$$

$$I_{1\omega}^{fit}(\delta) = c_0^{1\omega} \cdot \int_{-\infty}^{+\infty} e^{-\left|\frac{\delta-t}{T_2^{01}}\right|} \cdot e^{-3ln2\left(\frac{t}{\tau}\right)^2} dt \tag{5.18}$$

$$(5.19)$$

$$I_{0\omega}^{fit}(\delta) = c_0^{0\omega}\left[1 + c_1\int_{-\infty}^{+\infty} e^{-\left|\frac{\delta-t}{T_1}\right|} \cdot e^{-4ln2\left(\frac{t}{\tau}\right)^2} dt + c_2\int_{-\infty}^{+\infty} e^{-\left|\frac{\delta-t}{T_2^{01}}\right|} \cdot e^{-4ln2\left(\frac{t}{\tau}\right)^2} dt\right]$$

we extracted from the 2PPE and SHG envelopes the energy ($T_1$) and phase relaxation times ($T_2^{01}$, $T_2^{02}$) at final state energy 5.4 eV corresponding to the unoccupied quantum well state in Fig. 4.15 a). The relaxation time parameters are: $T_1$=4 fs, $T_2^{01}$=8 fs, $T_2^{02}$=5 fs.

All the relaxation times reported above are smaller than the pulse width $\tau$=10 fs. Although above analysis of envelopes give the possibility to deduce the relaxation parameters, the experimental autocorrelation should be fitted directly by a simulation, when the relaxation parameters become less than the pulse width [179]. For the simulation we used the mathematical description of the laser pulses as given in Ref. [180]:

$$E(\omega) = E^+(\omega) + E^-(\omega) \qquad (5.20)$$
$$E^+(\omega) = |E^+(\omega)| * e^{-i\phi(\omega)}$$

where $|E(\omega)|$ is the spectral amplitude of the electric field of the laser pulse and $\phi(\omega)$ is the spectral phase component which can be expanded into a Taylor series: $\phi(\omega) = \phi(\omega_0) + \phi'(\omega_0)(\omega-\omega_0) + \frac{1}{2}\phi''(\omega_0)(\omega-\omega_0)^2 + \frac{1}{6}\phi''(\omega_0)(\omega-\omega_0)^3 + ...$ introducing the group delay dispersion (GDD) $\phi''$ and third-order dispersion (TOD) $\phi'''$. To estimate the values of GDD and TOD of the laser pulses used in experiment we iteratively compared the envelopes extracted by Fourier transforming the experimental (SHG) and simulated autocorrelation curves. To obtain the autocorrelation from our simulated pulse we use formula for quadratic interferometric autocorrelation [180] expressed by:

$$S_{int}AC(\delta) = \int_{-\infty}^{+\infty} (E(t) + E(t+\delta)^2)^2 dt \qquad (5.21)$$

Using this procedure the pulse width, group delay dispersion and third-order dispersion values are found to be: $\tau_{sim} = 13\,fs$, $GDD_{sim} = 20\,fs^2$ and $TOD_{sim} = 1000\,fs^3$. The simulated pulse is showed in Fig. 5.18.

After reconstructing the electric field we used it to simulate the cross-correlation of 2PPE in order to estimate quantitatively the relaxation time constants. We solved nu-
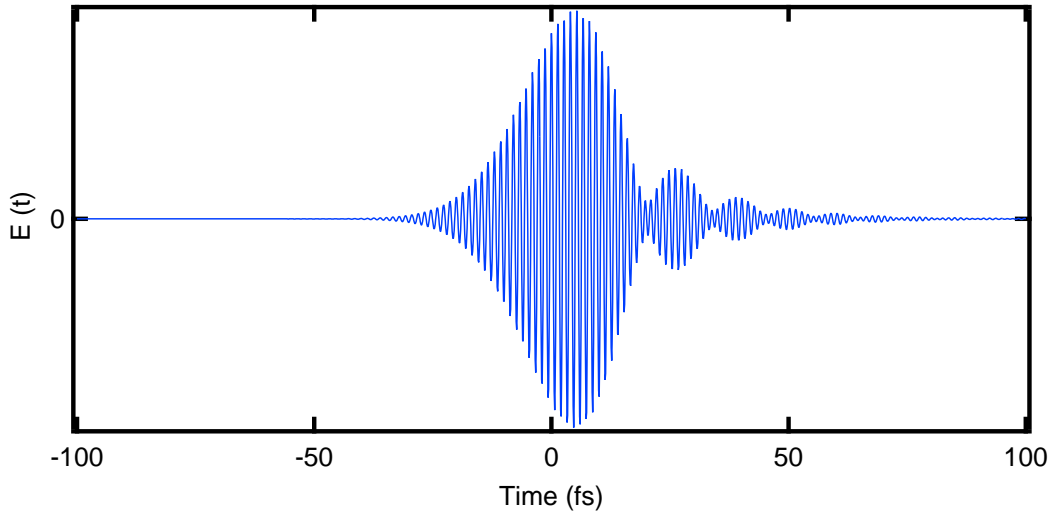
Figure 5.18:  Simulated laser pulse corresponding to the real pulse in experiment. The electric field $E(t)$ is plotted as a function of time.
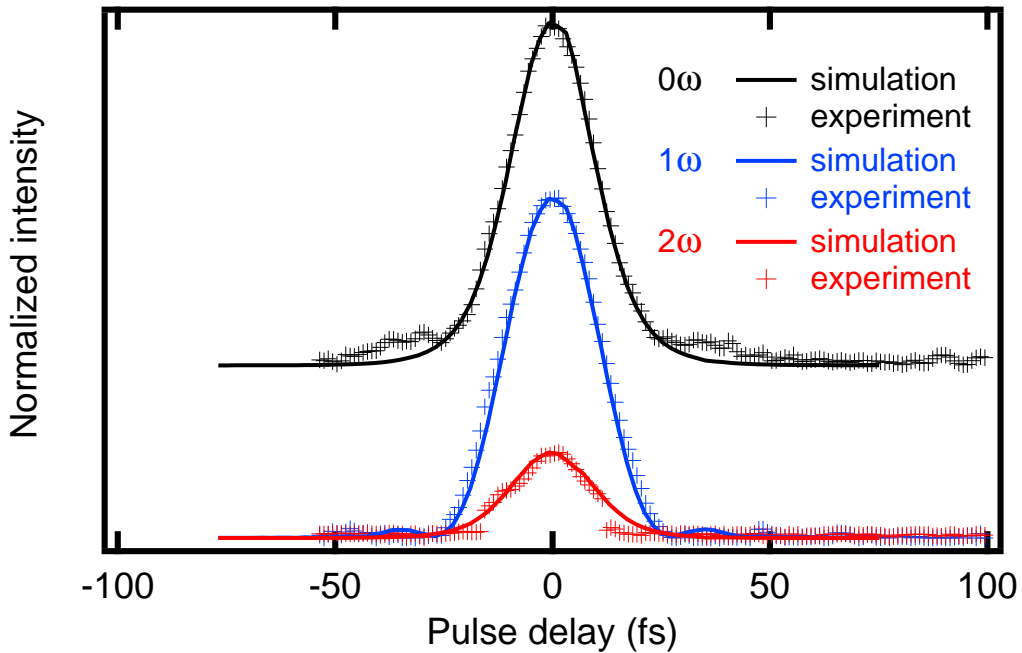


Figure 5.19:  Envelope fitting of the measured SHG autocorrelation curve with the simulated one used for determination of the laser pulse.

merically a set of differential equations arising from Liouville - von Neumann equation introduced in Sec. 2.1.3 by Eqn. 2.12. The electromagnetic field of the laser pulse is used to define the interaction operator $\hat{V}_I$ which describes the coupling between the electronic states in the presence of laser electric field. The simulated cross-correlation curves of

2PPE are decomposed by Fourier transformation into envelopes. Next we compared the obtained envelopes with the experimental ones iteratively until they matched. This procedure allowed determination of the energy relaxation time value as $T_1$=6 fs. The solution of Eqn. 2.12 for laser pulse presented in Fig. 5.18 is shown in Fig. 5.20.

By applying the above procedure to the 2PPE cross-correlation measured on the cobalt films grown at low temperature we found a lower value of the energy relaxation time $T_1$=2 fs. The 4 fs difference in the energy relaxation time is attributed to the increase of electron lifetime of optically excited electrons in the unoccupied quantum well state QW in Co/Cu(001). The longer lifetime of excited electron in the quantum well state is further in agreement with our observation, that $0\omega$ envelopes are narrower by approximately 2 fs in FWHM at energies beside the quantum well state peak position as showed in Fig. 4.17.

Conclusion: The analysis of measured interferometric time-resolved two-photon photoemission correlation curve show the increase in the width of the phase averaged $0\omega$ envelope attributed to the quantum well state formation. Two different methods were used to analyze the cross-correlation curves. The first approach proposed by the Nessler *et al.* [78], reveals that the lifetime effect is shorter than the laser pulse width and therefore the alternative method is suggested for a more precise quantitative estimation of the lifetime, as pointed by Ogawa *et al.* [179]. The second approach is suitable for shorter lifetime as compared to the laser pulse width and relies on numerical calculation using modelled laser electric field in the Liouville-von Neumann equation. As a result, the 4 fs increase in the lifetime of optically excited electrons in the unoccupied quantum well state was extracted.

Figure 5.20:   a) The simulation of interferometric two-photon photoemission correlation curve, b) the measured 2PPE interferometric correlation c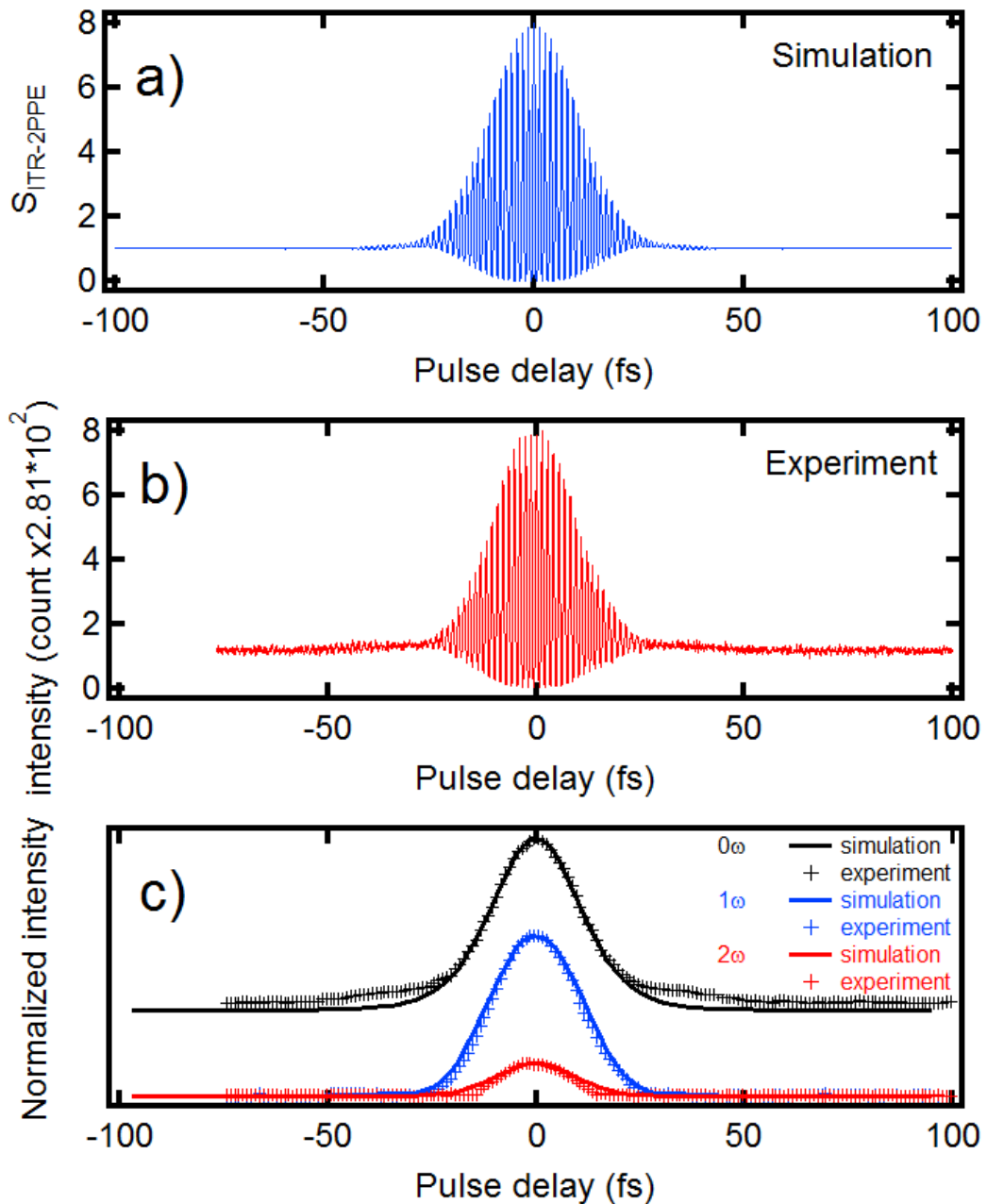urve, c) envelope fitting of the measured correlation curve with the simulated one used for estimation of the life time.

# 6 Conclusion

The electronic states of adatoms and ultrathin films on noble metal surfaces were studied by laser-based one- and two-photon photoemission spectroscopy (1PPE, 2PPE) and second harmonic generation (SHG). The electronic states under different confinement conditions were identified in 1- and 2PPE. The SHG signal provides information regarding the nonlinear optical response of studied system integrated over several electronic states and can be used to retrieve the electric field of incident laser pulses. Going from the zero dimensional atom-like unoccupied $\sigma$ state in Cs/Cu(111) to the two dimensional spin-polarized quantum well states in Fe/Ag(001) and Co/Cu(001), this work directly reveals the significant contribution from confined electronic states in the macroscopic nonlinear optical response, in the oscillation of photoemission intensity, and in the lifetime of optically excited electrons.

The spectroscopic photoemission experiments combined simultaneously with non-linear optical investigations provided information about the change of electronic structure during adsorption of cesium atoms on the Cu(111) surface. In both 2PPE and SHG signals optical resonances were observed. By systematic variation of the incident photon energy and the temperature growth, the contributions to the resonant optical transition due to the unoccupied Cs state and other surface states are assigned. The observed maximum in the SHG intensity is attributed to the resonant optical transition from the Shockley surface state to Cs state. From a model calculation, the Shockley surface state to the $n = 1$ image potential state transition is found to be responsible for the additional contribution to the SHG signal. Moreover a temperature dependent shift in the binding energy of the Shockley surface state is used in the model to explain the temperature dependence in SHG and 2PPE.

In the ultrathin iron films on Ag(001) the formation of quantum well states (QWS) derived from the $d$ bands near to the Fermi level is observed via 1PPE. By using the dipole selection rules for linearly polarized light the symmetry character of QWS is identified and compared with the bulk band structure. The QWS give rise to oscillatory photoemission intensity in 1PPE and is found to be of majority spin and $\Delta_5$ spatial symmetry character. The spin polarization of photoelectrons from the QWS is 37%. In contrast to the oscillatory photoemission intensity, no oscillations in spin polarization could be detected within the accuracy of our experiments. The Fe thickness dependence of the binding energy of QWS is understood by using the bulk band structure in combination with the phase accumulation model. We observed the image potential resonance on the iron film on Ag(001) and discussed the changes of it's binding energy and effective mass upon oxygen exposure.

Analysis of the measured interferometric time-resolved two-photon photoemission correlation curves on the ultrathin cobalt films on Cu(001), reveal the lifetime of optically excited electrons in the unoccupied QWS. Two different approaches are used to analyze the data. The first approach according to Nessler *et al.* [78] provides a rough estimation of the relaxation times by fit functions, and indicate a lifetime of QWS shorter than the laser pulse duration. The second approach is based on a simulation with optical Bloch equations using the incident laser electric field extracted from the measured SHG autocorrelation curve. The comparison between time-resolved 2PPE studies on cobalt films with different growth temperature shows significant difference in the density of electronic states and allows identification of a 4 fs increase in the lifetime of optically excited electrons due to the formation of the unoccupied QWS.

# Bibliography

[1] Roduner, E., "Size matters: why nanomaterials are different," Chem. Soc. Rev. **35**, 583 (2006)

[2] Barnham, K. & Vvedensky, D., *Low dimensional semiconductor structures* (Cambridge, 2001)

[3] Kröger, J., Becker, M., Jensen, H., von Hofe, T., Nèel, N., Limot, L., Berndt, R., Crampin, S., Pehlke, E., Corriol, C., Silkin, V. M., Sànchez-Portal, D., a: Arnau, Chulkov, E. V. & Echenique, P. M., "Dynamics of surface-localised electronic excitations studied with the scanning tunelling microscope," Progress in Surface Science **82**, 293 (2007)

[4] Gauyacq, J. P., Borisov, A. & Bauer, M., "Excited states in the alkali/noble metal surface systems: A model system for the study of charge transfer dynamics at surfaces," Proc. R. Soc. Lond. A **82**, 244 (2007)

[5] Trioni, M., Achilli, S. & Chulkov, E., "Key ingrediens of alkali atom - metal surface interaction: Chemical bonding versus spectral properties," Progress in Surface Science **88**, 160 (2013)

[6] Park, J. C., Kim, J., Kwon, H., & Song, H., "Gram-scale synthesis of $cu_2o$ nanocubes and subsequent oxidation to cuo hollow nanostructures for lithium-ion battery anode materials," Advenced Materials **21**, 803 (2008)

[7] Yang, X.-F., Wang, A., Qiao, B., Li, J., Liu, J. & Zhang, T., "Single-atom catalysts: A new frontier in heterogeneous catalysis," Accounts of chemical research **46**, 1740 (2013)

[8] Chiang, T. C., "Photoemission studies of quantum well states in thin films," Surface Science Reports **39**, 181 (2000)

[9] Meier, T., Thomas, P. & Koch, S. W., *Coherent Semiconductor Optics* (Springer, 2007)

[10] Paggel, J. J., Wei, C. M., Chou, M. Y., Luh, D. A., Miller, T. & Chiang, T. C., "Atomic-layer-resolved quantum oscillations in the work function: Theory and experiment for Ag/Fe(001)," Phys. Rev. B **66**, 233403 (2002)

[11] Valla, T., Kralj, M., Šiber, A., Milun, M., Pervan, P., Johnson, P. D. & Woodruff, D. P., "Oscillatory electron–phonon coupling in ultra-thin silver films on V(100)," J. Phys.: Condens. Matter **12**, L477 (2000)

[12] Luh, D. A., Miller, T., Paggel, J. J., Chou, Y. & Chiang, T.-C., "Large electron-phonon coupling at an interface," Phys. Rev. Lett. **88**, 256802 (2002)

[13] Mathias, S., Wiesenmayer, M., Aeschlimann, M. & Bauer, M., "Quantum-well wave-function localization and the electron-phonon interaction in thin Ag nanofilms," Phys. Rev. Lett. **97**, 236809 (2006)

[14] Aballe, L., Barinov, A., Locatelli, A., Heun, S. & Kiskinova, M., "Tuning surface reactivity via electron quantum confinement," Phys. Rev. Lett. **93**, 196103 (2004)

[15] Luh, D.-A., Miller, T., Paggel, J. J., Chou, M. Y. & Chiang, T.-C., "Quantum electronic stability of atomically uniform films," Science **292**, 1131 (2001)

[16] Otero, R., de Parga, A. L. V. & Miranda, R., "Observation of preferred heights in Pb nanoislands: A quantum size effect," Phys. Rev. B **66**, 115401 (2002)

[17] Upton, M. H., M.Wei, C., Chou, M., Miller, T. & Chiang, T.-C., "Thermal stability and electronic structure of atomically uniform Pb films on Si(111)," Phys. Rev. Lett. **93**, 026802 (2004)

[18] Li, J., Przybylski, M., Yildiz, F., Ma, X. D. & Wu, Y. Z., "Oscillatory magnetic anisotropy originating from quantum well states in Fe films," Phys. Rev. Lett. **102**, 207206 (2009)

[19] Bauer, U. & Przybylski, M., "Large amplitude oscillation of magnetic anisotropy engineered by substrate step density," Phys. Rev. B **81**, 134428 (2010)

[20] Grünberg, P., Schreiber, R. & Pang, Y., "Layered magnetic structures: Evidence for antiferromagnetic coupling of Fe layers across Cr interlayers," Phys. Rev. Lett. **57**, 2442 (1986)

[21] Bruno, P., "Theory of interlayer magnetic coupling," Phys. Rev. B **52**, 411 (1995)

[22] Hirota, E., Sakakima, H. & Inomata, K., *Giant Magneto-Resistance Devices* (Springer, 2002)

[23] Bauer, U., Przybylski, M., Kirschner, J. & Beach, G. S. D., "Magnetoelectric charge trap memory," Nano letters **12**, 1437 (2012)

[24] Reinert, F. & Hüfner, S., "Photoemission spectroscopy—from early days to recent applications," New. J. Phys. **7**, 97 (2005)

[25] *Solid-State Photoemission and Related Methods: Theory and Experiment*, edited by Schattke, W. & Van Hove, M. A. (Wiley-VCH Verlag GmbH, Weinheim, Germany, 2003)

[26] Hüfner, S., *Photoelectron Spectroscopy* (Springer Verlag, Berlin Heidelberg New York, 1995)

[27] *Photoemission and the electronic properties of surfaces*, edited by Feuerbacher, B., Fitton, B. & Willis, R. F. (John Wiley & Sons, 1978)

[28] Damascelli, A., Hussain, Z. & Shen, Z.-X., "Angle-resolved photoemission studies of the cuprate superconductors," Rev. Mod. Phys. **75**, 473 (2003)

[29] Yusof, Z., Wells, B., Valla, T., Johnson, P., Fedorov, A., Li, Q., Loureiro, S. & Cava, R., "Angle-resolved photoemission study of the metal-insulator transition in bismuth cobaltates," Phys. Rev. B **76**, 165115 (2007)

[30] Bostwick, A., Emtsev, K. V., Horn, K., Huwald, E. & Ley, L., "Photoemission Studies of Graphene on SiC : Growth , Interface , and Electronic Structure," Advances in Solid State Physics **170**, 159 (2008)

[31] Bostwick, A., Ohta, T., McChesney, J. L., Seyller, T., Horn, K. & Rotenberg, E., "Band structure and many body effects in graphene," The European Physical Journal Special Topics **148**, 5 (2007)

[32] Seyller, T., Bostwick, A., Emtsev, K. V., Horn, K., Ley, L., McChesney, J. L., Ohta, T., Riley, J. D., Rotenberg, E. & Speck, F., "Epitaxial graphene: a new material," physica status solidi (b) **245**, 1436 (2008)

[33] Hsieh, D., Xia, Y., Qian, D., Wray, L., Meier, F., Dil, J., Osterwalder, J., Patthey, L., Fedorov, A., Lin, H., Bansil, A., Grauer, D., Hor, Y., Cava, R. & Hasan, M., "Observation of time-reversal-protected single-dirac-cone topological-insulator states in bi2te3 and sb2te3," Phys. Rev. Lett. **103**, 2 (2009)

[34] Wray, L. A., Xu, S.-Y., Xia, Y., Hor, Y. S., Qian, D., Fedorov, A. V., Lin, H., Bansil, A., Cava, R. J. & Hasan, M. Z., "Observation of topological order in a superconducting doped topological insulator," Nature Physics **5**, 1 (2010)

[35] Barke, I., Zheng, F., Rügheimer, T. K. & Himpsel, F. J., "Experimental evidence for spin-split bands in a one-dimensional chain structure," Phys. Rev. Lett. **97**, 1 (2006)

[36] Crain, J. N., Kirakosian, A., Altmann, K. N., Bromberger, C., Erwin, S. C., McChesney, J. L., Lin, J.-L. & Himpsel, F. J., "Fractional band filling in an atomic chain structure," Phys. Rev. Lett. **90**, 1 (2003)

[37] Crain, J., Altmann, K., Bromberger, C. & Himpsel, F., "Fermi surfaces of surface states on si(111)-ag, au," Phys. Rev. B **66**, 1 (2002)

[38] Einstein, A., "Über einen die erzeugung und verwandlung des lichtes betreffenden heuristischen gesichtspunkt [adp 17, 132 (1905)]," Annalen der Physik **14**, 164 (2005)

[39] Pendry, J., "Theory of photoemission," Surf. Sci. **57**, 679 (1976)

[40] Band, Y. B., *Light and matter : electromagnetism, optics, spectroscopy and lasers* (Wiley, 2006) ISBN 978-0-471-89930-3

[41] Braun, J., "The theory of angle-resolved ultraviolet photoemission and its application to ordered materials," Rep. Prog. Phys. **59**, 1267 (1996)

[42] Schattke, W., Van Hove, M. A., Garcia De Abajo, F. J., Diez Muino, R. & Mannella, N., "Overview of core and valence photoemission," in *Solid-State Photoemission and Related Methods: Theory and Experiment*, edited by Schattke, W. & Van Hove, M. A. (Wiley-VCH, 2003) Chap. 2, pp. 50–115

[43] Winkelmann, A., Hartung, D., Engelhard, H., Chiang, C.-T. & Kirschner, J., "High efficiency spin polarization analyzer based on exchange scattering at Fe/W(001)," Rev. Sci. Instum. **79**, 083303 (2008)

[44] Stöhr, J. & Siegmann, H. C., *Magnetism From Fundamentals to Nanoscale Dynamics* (Springer, 2006)

[45] Göppert-Mayer, M., "Über elementarakte mit zwei quantensprüngen," Annalen der Physik **401**, 273 (1931)

[46] Göppert-Mayer, M., "Elementary processes with two quantum transitions," Annalen der Physik **18**, 466 (2009)

[47] Teich, M., Schroeer, J. & Wolga, G., "Double-quantum photoelectric emission from sodium metal," Phys. Rev. Lett. **13**, 611 (1964)

[48] Gruebele, M. & Zewail, A. H., "Ultrafast reaction dynamics," Physics Today **43**, 24 (1990)

[49] Brabec, T. & Krausz, F., "Intense few-cycle laser fields: Frontiers of nonlinear optics," Rev. Mod. Phys. **72**, 545 (2000)

[50] Krausz, F. & Ivanov, M., "Attosecond physics," Rev. Mod. Phys. **81**, 163 (2009)

[51] Kampfrath, T., Sell, A., Klatt, G., Pashkin, A., Mährlein, S., Dekorsy, T., Wolf, M., Fiebig, M., Leitenstorfer, A. & Huber, R., "Coherent terahertz control of antiferromagnetic spin waves," Nature Photonics **5**, 31 (2011)

[52] Echenique, P. M. & Pendry, J. B., "The existence and detection of rydberg states at surfaces," J. Phys. C: Solid State Physics **11**, 2065 (1978)

[53] Steinmann, W., "Two-photon photoemission spectroscopy of electronic states at metal surfaces," physica status solidi (b) **192**, 339 (1995)

[54] Höfer, U., "Time-resolved coherent photoelectron spectroscopy of quantized electronic states on metal surfaces," Science **277**, 1480 (1997)

[55] Weinelt, M., "Time-resolved two-photon photoemission from metal surfaces," J. Phys. Cond. Matter **14**, R1099 (2002)

[56] Th. Fauster, "Time Resolved Two-Photon Photoemission," in *Solid-State Photoemission and Related Methods: Theory and Experiment*, edited by Schattke, W. & van Hove, M. (Wiley-VCH, 2003) Chap. 8, p. 247

[57] Weinelt, M., Schmidt, A. B., Pickel, M. & Donath, M., "Spin-polarized image-potential-state electrons as ultrafast magnetic sensors in front of ferromagnetic surfaces," Prog. Surf. Sci. **82**, 388 (2007)

[58] Fauster, T., "Electron Dynamics in Image Potential States at Metal Surfaces," in *Dynamics at Solid State Surface and Interfaces Vol.1: Current Developments*, Vol. 1, edited by Bovensiepen, U., Petek, H. & Wolf, M. (Wiley, 2010) pp. 53–73, ISBN 978-3-527-40937-2

[59] Blum, K., *Density Matrix Theory and Applications* (Plenum Press, New York, 1996)

[60] Mukamel, S., *Principles of Nonlinear Optical Spectroscopy* (Oxford University Press, New York, 1995)

[61] Boyd, R., *Nonlinear Optics*, 3rd ed. (Academic Press, Amsterdam Boston, 2008)

[62] Loudon, R., *The Quantum Theory of Light*, 3rd ed. (Oxford University Press, Oxford, New York, 2000)

[63] Letokhov, V. S. & Chebotayev, V. P., *Nonlinear Laser Spectroscopy* (Springer Verlag, Berlin Heidelberg New York, 1977)

[64] Knoesel, E., Hotzel, A. & Wolf, M., "Temperature dependence of surface state lifetimes, dephasing rates and binding energies on cu(111) studied with time-resolved photoemission," J. Electron Spectr. Rel. Phenom. **88-91**, 577 (1998)

[65] Ueba, H. & Mii, T., "Theory of energy- and time-resolved two-photon photoemission from metal surfaces -influence of pulse duration and excitation condition," Appl. Phys. A **71**, 537 (2000)

[66] Weida, M. J., Ogawa, S., Nagano, H. & Petek, H., "Ultrafast interferometric pump - probe correlation measurements in systems with broadened bands or continua," J. Opt. Soc. Am. B **17**, 1443 (2000)

[67] Ramakrishna, S. & Seideman, T., "Coherence spectroscopy in dissipative media: a liouville space pathway approach.." J. Chem. Phys. **122**, 84502 (2005)

[68] Pontius, N., Sametoglu, V. & Petek, H., "Simulation of two-photon photoemission from the bulk sp-bands of ag(111)," Phys. Rev. B **72**, 115105 (2005)

[69] Winkelmann, A., Sametoglu, V., Zhao, J., Kubo, A. & Petek, H., "Angle-dependent study of a diret optical transition in the sp bands of Ag(111) by one- and two-photoemission," Phys. Rev. B **76**, 195428 (2007)

[70] Merschdorf, M., Kennerknecht, C. & Pfeiffer, W., "Collective and single-particle dynamics in time-resolved two-photon photoemission," Phys. Rev. B **70**, 193401 (2004)

[71] Wolf, M., Hotzel, A., Knoesel, E. & Velic, D., "Direct and indirect excitation mechanisms in two-photon photoemission spectroscopy of cu(111) and co/cu(111)," Phys. Rev. B **59**, 5926 (1999)

[72] Meier, T., Thomas, P. & Koch, S. W., *Coherent Semiconductor Optics* (Springer Berlin Heidelberg, Berlin, Heidelberg, 2007)

[73] Schmidt, A. B., Pickel, M., Donath, M., Buczek, P., Ernst, A., Zhukov, V., Echenique, P., Sandratskii, L., Chulkov, E. & Weinelt, M., "Ultrafast magnon generation in an fe film on cu(100)," Phys. Rev. Lett. **105**, 197401 (2010)

[74] Weinelt, M., Schmidt, A. B., Pickel, M. & Donath, M., "Spin-dependent relaxation of photoexcited electrons at surfaces of 3d ferromagnets," in *Dynamics at Solid State Surfaces and Interfaces: Current Developments*, Vol. 1, edited by Bovensiepen, U., Petek, H. & Wolf, M. (Wiley-VCH, Weinheim, 2010) pp. 19–22

[75] Petek, H., Nagano, H. & Ogawa, S., "Hot-electron dynamics in copper revisited: the d-band effect," Applied Physics B **68**, 369 (1999)

[76] Weinelt, M., "Time-resolved two-photon photoemission from metal surfaces," Journal of Physics: Condensed Matter **14**, R1099 (2002)

[77] Petek, H. & Ogawa, S., "Femtosecond time-resolved two-photon photoemission studies of electron dynamics in metals," Prog. Surf. Sci. **56**, 239 (1997)

[78] Nessler, W., Ogawa, S., Nagano, H., Petek, H., Shimoyama, J., Nakayama, Y. & Kishio, K., "Energy relaxation and dephasing times of excited electrons in $Bi_2Sr_2CaCu_2O_{6+\delta}$ from interferometric 2-photon time-resolved photoemission," Journal of Electron Spectroscopy and Related Phenomena **88-91**, 495 (1998)

[79] Petek, H., Nagano, H., Weida, M. & Ogawa, S., "The role of Auger decay in hot electron excitattion in copper," Chemical Phzsics **251**, 71 (2000)

[80] Shen, Y. R., "Surface properties probed by second-harmonic and sum-frequency generation," Phys. Rev. B **337**, 519 (1989)

[81] Mochán, W. L. & Maytorena, A., "Theory of surface second harmonic generation," EPIOPTICS-8. Proceedings of the 33rd Course of the International School of Solid State Physics **ISBN 9789812773869**, 17 (2006)

[82] Timm, C. & Bennemann, K. H., "Response theory for time-resolved second-harmonic generation and two-photon photoemission," Journal of Physics: Condensed Matter **16**, 661–694 (2004)

[83] Winkelmann, A., Lin, W.-C., Bisio, F., Petek, H. & Kirschner, J., "Interferometric control of spin-polarized electron populations at a metal surface observed by multiphoton photoemission," Phys. Rev. Lett **100**, 206601 (2008)

[84] Bertacco, R., Onofrio, D. & Ciccacci, F., "A novel electron spin-polarization detector with very large analyzing power," Rev. Sci. Instum. **70**, 3573 (1999)

[85] Bertacco, R. & Ciccacci, F., "Oxygen-induced enhancement of spin-dependent effects in electron spectroscopies of Fe(001)," Phys. Rev. B **59**, 4207 (1999)

[86] Kessler, J., *Polarised Electrons* (Springer, 1985)

[87] Fauster, T., Reuß, C., Shumay, I. L. & Weinelt, M., "Influence of surface morphology on surface states for Cu on Cu(111)," Phys. Rev. B **61**, 16168 (2000)

[88] Lindgren, S. A. & Waldén, L., "Structure and electronic properties of Cs adsorbed on cu(111)," Solid State Communications **25**, 13 (1978)

[89] Bürgler, D., Schmidt, C., Schaller, D., Meisinger, F., Hofer, R. & G"untherodt, H.-J., "Optimized epitaxial grownth of Fe on Ag(001)," Phys. Rev. B **56**, 4149 (1997)

[90] Chiang, C.-T., *Spin and magnetization dependent two-photon photoemission from ultrathin ferromagnetic cobalt films*, Ph.D. thesis, Der Naturwissenschaftlichen Fakultät II der Martin-Luther Universität Halle-Wittenberg (2010)

[91] Petek, H. & Ogawa, S., "Femtosecond time-resolved two-photon photoemission studies of electron dynamics in metals," Progress in Surface Science **56**, 239 (1997)

[92] Ortega, J. E. & Himpsel, F. J., "Quantum well states and magnetic coupling between ferromagnets through a noble-metal layer," Phys. Rev. B **47**, 1540 (1993)

[93] Zhao, J., Pontius, N., Winkelmann, A., Sametoglu, V., Kubo, A., Borisov, A. G., Sánchez-Portal, D., Silkin, V. M., Echenique, E. V. C. P. M. & Petek, H., "Electronic potential of a chemisorption interface," Phys. Rev. B **78**, 085419 (2008)

[94] Petek, H., Weida, M. J., Nagano, H. & Ogawa, S., "Electronic relaxation of alkali metal atoms on the Cu(111) surface," Surface Science **451**, 22 (2000)

[95] Bauer, M., Pawlik, S. & Aeschlimann, M., "Resonance lifetime and energy of an excited Cs state on Cu(111)," Phys. Rev. B **55**, 10040 (1997)

[96] Lindgren, S. A. & Waldén, L., "In terband transitions, surface-barrier photoabsorption, and charge-screening waves observed via optical second-harmonic generation of Cs-covered Cu(111)," Phys. Rev. B **45**, 6345 (1992)

[97] Hamawi, A., Lindgren, S. A. & Waldén, L., "Quantum size effects in thin metal overlayers," Physica Scripta **T39**, 339 (1991)

[98] Ishida, H., Mizoguchi, R., Onda, K., Hirose, C., Kano, S. & Wada, A., "Secon harmonic observation of Cu(111) surface: in situ measurements during molecular adsorption," Surface Science **526**, 201 (2003)

[99] Lüpke, G., "Resonant second-harmonic generation on Cu(111) by a surface-state to image-potential-state transition," Phys. Rev. B **49**, 17303 (1994)

[100] Schneider, R., Dürr, H., Fauster, T. & Dose, V., "Temperature dependence of the inverse photoemission from copper surfaces," Phys. Rev. B **42**, 1638 (1990)

[101] Borisov, A. G., Kazansky, A. K. & j. P. Gauyacq, "Stabilisation of alkali-adsorbate-induced states on cu(111) surfaces," Surface Science **430**, 165 (1999)

[102] Dounce, S. M., Yang, M. & Dai, H.-L., "Surface-state relaxation dynamics on Ag(110) probed by temperature-dependent resonantly enhanced second-harmonic generation," Phys. Rev. B **67**, 205410 (2003)

[103] Dounce, S. M., Yang, M. & Dai, H.-L., "Physisorption on a metal surface probed by surface state resonant second harmonic generation," Surface Science **565**, 27 (2004)

[104] Schwab, C., Meister, G., Goldmann, A. & Bertell, E., "Second-harmonic generation from Na-covered Cu(110): intensity enhancement by inter-surface-state transitions?." Surface Science **469**, 93 (2000)

[105] Dounce, S. M. & Dai, H.-L., "The effect of adsorption of Na on Cu(110) surface states probed by second harmonic generation," Surface Science **583**, 310 (2005)

[106] Knoesel, E., Hotzel, A. & Wolf, M., "Temperature dependence of surface state lifetimes, dephasing rates and binding energies on Cu(111) studied with time-resolved photoemission," JOURNAL OF ELECTRON SPECTROSCOPY and Related Phenomena **88-91**, 577 (1998)

[107] Knapp, J. A., Himpsel, F. J., Wil1iams, A. R. & Eastman, D. E., "Temperature dependence of bulk and surface energy bands in copper using angle-resolved photoemission," Phys. Rev. B **19**, 2844 (1979)

[108] Matzdorf, R., Meister, G. & Goldmann, A., "Temperature-dependent photoemission spectra from Cu(100) and Cu(111) surfaces," Surface Science **286**, 56 (1993)

[109] Paniago, R., Matzdorf, R., Meister, G. & Goldmann, A., "Temperature dependence of shockley-type surface energy bands on Cu(111), Ag(ll1) and Au(111)," Surface Science **336**, 113 (1995)

[110] Ogawa, S., Nagano, H. & Petek, H., "Phase and energy relaxation in an antibonding surface state: Cs/Cu(111)," Phys. Rev. Lett. **82**, 1931 (1999)

[111] Adler, D. A., "Top-site for K on Cu(111) and Ni(111) surfaces," Phys. Rev. B **48**, 17445 (1993)

[112] Williams, R. S., Wehner, P. S., Stöhr, J. & Shirley, D. A., "Thermally induced breakdown of the direct-transition model in copper," Phys. Rev. Lett. **39**, 302 (1977)

[113] Petek, H., Weida, M. J., Nagano, H. & Ogawa, S., "Real-time observation of adsorbate atom motion above a metal surface," Science **288**, 1402 (2000)

[114] Nojima, A., Yamashita, K. & Hellsing, B., "Model calculation of the electron-phonon coupling in Cs/Cu(111)," Phys. Rev. B **78**, 035417 (2008)

[115] Li, J., Chen, G., Wu, Y. Z., Rotenberg, E. & Przybylski, M., "Quantum well states and oscillattory magnetic anisotropy in ultrathin Fe films," IEEE Transactions on Magnetics **47**, 0018 (2011)

[116] Bauer, U. & Przybylski, M., "Quantum well states and oscillatory magnetic anisotropy in ultrathin Fe films," Phys. Rev. B **81**, 134428 (2010)

[117] Tom, H. W., Mate, C. M., Zhu, X. D., Crowell, J. E., Heinz, T. F., Somorjai, G. A. & Shen, Y. R., "Surface studies by optical second-harmonic generation: The adsorption of $O_2$, CO and sodium on the Rh(111) surface," Phys. Rev. Lett. **52**, 348 (1984)

[118] Hayashi, K., Arafune, R., Ueda, S. & Ushioda, S., "Spike structure in the very low energy photoelectron spectra of Ag(001)," Applied Surface Science **237**, 296 (2004)

[119] Sanchez, O., Gracia, J. M., Segovia, P., Alvarez, J., Deparga, A. L. V., Ortega, J. E., Prietsch, M. & Miranda, R., "Lateral confinement of surface states on stepped Cu(111)," Phys. Rev. B **52**, 7894 (1995)

[120] Crommie, M. F., Lutz, C. P. & Eigler, D. M., "Confinement of electrons to quantum corrals on a metal surface," Science **262**, 218 (1993)

[121] Jonker, B. T., Walker, K. H., Kisker, E., Prinz, G. A. & Carbone, C., "Spin -polarized photoemssion study of epitaxial Fe(001) films on Ag(001)," Phys. Rev. Lett **57**, 142 (1986)

[122] Li, H., Li, Y. S., Quin, J. & Tian, D., "Quantitative low electrn-diffaction study of the epitaxy of the Fe on the Ag(001):questions about growth mode," Rapid Communications **42**, 9195 (1990)

[123] Canzian, A., Bozzolo, G. & Mosca, H. O., "Modeling of stable and metastable structures of Co, Cr or Fe deposited on Ag(100)," Thin Solid Films **519**, 2201 (2011)

[124] Bruns, D., *Structure and morphology of ultrathin iron and iron oxide Films on Ag(001)*, Ph.D. thesis, Fachbereich Physik der Universität Osnabrück (2012)

[125] Chiang, T.-C., "Photoemission studies of quantum well states in thin films," Surface science reports **39**, 181 (2000)

[126] Ortega, J. E. & Himpsel, F. J., "Quantum well states and magnetic coupling between noble metals and ferromagnets," J. Appl. Phys. **73**, 5771 (1993)

[127] Fritsche, L., Noffke, J. & Eckardt, H., "A relativistic treatment of interacting spin-aligned electron systems: application to ferromagnetic iron, nickel and palladium metal," J. Phys. F: Met. Phys **17**, 943 (1987)

[128] Eckardt, H., Fritsche, L. & Noffke, J., "Self-consistent relativistic band structure of the noble metals," Journal of Physics F: Metal Physics **14**, 97 (1984)

[129] Schäfer, J., Hoinkins, M., Rotenberg, E., Blaha, P. & Claessen, R., "Fermi surface and electron correlation effects of ferromagnetic iron," Phys. Rev. B **72**, 155115 (2005)

[130] Wang, X., Yates, J. R., Souza, I. & Vanderbilt, D., "Ab initio calculation of the anomalous Hall conductivity by Wannier interpolation," Phys. Rev. B **74**, 195118 (2006)

[131] Yates, J. R., Wang, X., Vanderbilt, D. & Souza, I., "Spectral and Fermi surface properties from Wannier interpolation," Phys. Rev. B **75**, 195121 (2007)

[132] Yao, Y., Kleinman, L., MacDonald, A. H., Sinova, J., Jungwirth, T., sheng Wang, D., Wang, E. & Niu, Q., "First principles calculation of anomalous hall conductivity in ferromagnetic *bcc* Fe," Phys. Rev. Lett. **92**, 037204 (2004)

[133] Crangle, J. & Goodman, G. M., "The magnetization of pure iron and nickel," Proc. R. Soc. Lond. A **321**, 477 (1971)

[134] Gauyacq, J. P., Borisov, A. & Bauer, M., "Photoemission studies of quantum well states in thin films," Solid state communications **22**, 9 (1976)

[135] El-Batanouny, M. & Wooten, F., *Symmetry and Condensed Matter Physics A Computational Approach* (Cambrige university press, 2008)

[136] Eberhardt, W. & Himpsel, F. J., "Dipole selection rules for optical transitions in the *fcc* and *bcc* lattices," Physical review B **21**, 5572 (1980)

[137] Schneider, C. M. & Kirschner, J., "Spin- and angle-resolved photoelectron spectroscopy from solid surfaces with circularly polarized light," Critical Reviews in the Solid State and Materials Sciences **20(3)**, 179 (1995)

[138] Pletikosić, I., Trontl, V. M., Milun, M., Šokčević, D., Brako, R. & Pervan, P., "d-band quantum well states in Ag(111) monolayer films; substrate induced shifts," J. Phys.:Condens. Matter **20**, 355004 (2008)

[139] Terreni, S., Cossaro, A., Gonella, G., Mattera, L., Dò, L., Ciccacci, F., Cvetko, D., Floreano, L., Morgante, A., Verdini, A. & Canepa, M., "Surfactant effect and dissolution of ultrathin Fe films on Ag(001)," Phys. Rev. B **70**, 115420 (2004)

[140] D.A.Luh, Paggel, J., Miller, T. & Chiang, T.-C., "d-band quantum well states," Phys. Rev. Lett. **84**, 3410 (2000)

[141] Milun, M., Pervan, P. & Woodruff, D. P., "Quantum well structures in thin metal films: simple model physics in reality," Rep. Prog. Phys. **65**, 99 (2002)

[142] An., J. M., Raczkowski, D., Wu, Y. Z., Won, C. Y., Wang, L. W., Canning, Hove, M. A. V., Rotenberg, E. & Qiu, Z. Q., "Quantization cindition of quantum-well states in Cu/Co(001)," Phys. Rev. B **68**, 045419 (2003)

[143] Shikin, A. M., Rader, O., Prudnikova, G. V., Adamchuk, V. K. & Gudat, W., "Quantum well states of *sp*- and *d*-character in thin Au overlayers on W(110), journal = Phys. Rev. B, volume = 65, pages = 075403, year = 2002,"

[144] Smith, N. V., Brookes, N. B., Chang, Y. & Johnson, P. D., "Quantum-well and tight-binding analyses of spin-polarized photoemission from Ag/Fe(001) overlayers," Phys. Rev. B **49**, 332 (1994)

[145] Shikin, A. M., Vyalikh, D. V., Prudnikova, G. V. & Adamchuk, V. K., "Phase accumulation model analysis of quantum well resonances formed in ultra-thin Ag, Au films on W(110)," Surface Science **487**, 135 (2001)

[146] Smith, N. V., "Phase analysis of image states and surface states associated with nearly-free electron band gaps," Phys. Rev. B **49**, 332 (1994)

[147] McRAE, E. & KANE, M., "Calculations on the effect of the surface potential barrier in leed," Surface Science **108**, 435 (1981)

[148] ECHENlQlJE, P. & PENDRY, J., "Theory of image states at metal surfaces," Progress in Surface Science **32**, 111 (1990)

[149] Zangwill, A., *Physics at surfaces* (Cambrige, 1988)

[150] Finnis, M. W. & Heine, V., "Theory of lattice contraction at aluminium surfaces," J. Phys. F: Met. Phys **4**, L37 (1974)

[151] Sokolov, J., Jona, F. & Marcus, P., "Trends in metal surface relaxation," Solid state communications **49**, 307 (1984)

[152] Mavrikakis, M., Hammer, B. & Norskov, J. K., "Effect of strain on the reactivity of metal surfaces," Phys. Rev. Lett. **81**, 2819 (1998)

[153] Kisker, K., Schröder, K., Gudat, W. & Campagna, M., "Spin-polarized angle-resolved photoemission study of the electronic structure of Fe(100) as a function of temperaure," Phys. Rev. B **31**, 329 (1985)

[154] Feder, R., Rodriguez, A., Baier, U. & Kisker, E., "Theoretical analysis of spin-resolved photoemission data from ferromagnetic Fe(001)," Solid State Communications **52**, 57 (1984)

[155] Cowburn, R. P., Ferré, J., Jamet, J.-P., Gray, S. J. & Bland, J. A. C., "Role of remanent domain structure and cubic anisotropy in the reorientation phase transition of ultrathin Ag/Fe/Ag(001) epitaxial films," Phys. Rev. B **55**, 11593 (1997)

[156] Chen, J., Drakaki, M. & Erskine, J. L., "Chemisorption-induced change in thin-film spin anisotropy: Oxygen adsorption on the p(1×1)Fe/Ag(100)," Phys. Rev. B **45**, 3636 (1992)

[157] Echenique, P. M. & Uranga, M. E., "Image potential states at surfaces," Surface Science **247**, 125 (1991)

[158] Hotzel2007ProgSurf, "Electron dynamics of image potential states in weakly bound adsorbate layers: A short review," Progress in Surface Science **82**, 336 (2007)

[159] Dose, V., Altmann, W., Goldmann, A., Kolac, U. & Rogoyik, J., "Image-potential states observed by inverse photoemission," Phys. Rev. Lett. **52**, 1919 (1984)

[160] Ferrini, G., Giannetti, C., Fausti, D., Galimberti, G., Peloi, M., Banfi, G. & Parmigiani1, F., "Effective mass and momentum-resolved intrinsic linewidth of image-potential states on Ag(001)," Phys. Rev. B **67**, 235407 (2003)

[161] Hulbert, S. L., Johnson, P. D., Stoffel, N. G., Royer, W. A. & Smith, N. V., "Crystal-induced and image-potential-induced emtpy surface states on Cu (111) and Cu(001)," Phys. Rev. B **31**, 6815 (1985)

[162] Giesen, K., Hage, F., Himpsel, F. J., Riess, H. J., Steinmann, W. & Smith, N. V., "Effective mass of image-potential states," Phys. Rev. B **35**, 975 (1987)

[163] Li, Z. & Gao, S., "Band-theory calculation of image states on a metal surface," Phys. Rev. B **50**, 15349 (1994)

[164] Fauster, T. & Steinmann, W., "Electromagnetic waves: Recent development in research," Elsevier Science **2**, 347 (1995)

[165] Straub, D. & Himpsel, F. J., "Spectroscopy of image-potential states with inverse photoemission," Phys. Rev. B **33**, 2256 (1986)

[166] Giesen, K., Hage, F., Riess, H. J. & Steinmann, W., "Image potential states seen via two-photon photoemission and second harmonic generation," Physica Scripta **35**, 578 (1987)

[167] Reihl, B., Frank, K. H. & Schlittler, R. R., "Empty electronic states at the (100), (110),and (111) surfaces of nickel, copper, and silver," Phys. Rev. B **32**, 1971 (1985)

[168] Giesen, K., Hage, F., Himpsel, F. J., Riess, H. J. & Steinmann, W., "Binding energy of image-potential states: Dependence on crystal structure and material," Phys. Rev. B **35**, 971 (1987)

[169] Duncker, K., Kiel, M. & Widdra, W., "Momentum-resolved lifetimes of image-potential states on Ag(001)," Surface Science **606**, L87 (2012)

[170] Reihl, B., Frank, K. H. & Schlittler, R. R., "Image-potential and intrinsic surface states on Ag(100)," Phys. Rev. B **30**, 7328 (1984)

[171] Ebil, C., Schmidt, A. B. & Donath, M., "Appearence of the minority $d_{z^2}$ surface state and disappearance of the image-potential state: Criteria for clean Fe(001)," Phys. Rev. B **86**, 161414 (2012)

[172] Dose, V., "Image potential surface states," Physica Scirpta **36**, 669 (1987)

[173] Wolf, M., Knoesel, E. & Hertel, T., "Ultrafast dynamics of electrons in image-potential states on clean and Xe-covered Cu(111)," Phys. Rev. B **54**, R5295 (1996)

[174] Nývlt, M., Bisio, F., Franta, J., Gao, C. L., Petek, H. & Kirschner, J., "Surface magnetism during oxygen-aided Fe homoepitaxy," Phys. Rev. Lett **95**, 127201 (2005)

[175] Parihar, S. S., Meyerheim, H. L., Mohseni, K., Ostanin, S., Ernst, A., Jedrecy, N., Felici, R. & Kirschner, J., "Structure of O/Fe(001)-p(1×1) studied by surface x-ray diffration," Phys. Rev. B **81**, 075428 (2010)

[176] Tange, A., Gao, C. L., Yavorsky, B. Y., Maznichenko, I. V., Etz, C., Hergert, A. E. W., Mertig, I., Wulfhekel, W. & Kirschner, J., "Electronic structure and spin polarisation of Fe(001)-p(1×1)O surface," Phys. Rev. B **81**, 195410 (2010)

[177] Błoński, P., Kiejna, A. & Hafner, J., "Oxygen adsorption on the clean and O-precovered Fe(110) and (100) surfaces," J. Phys.: Condens. Matter **19**, 096011 (2007)

[178] Hotzel, A., Ishioka, K., Knossel, E., Wolf, M. & Ertl, G., "Can we controll lifetimes of electronic states at surfaces by adsorbate resonances," Chemical Phys. Lett. **285**, 271 (1998)

[179] Ogawa, S., "Femtosecond electron dynamics studied by interferometric time-resolved two-photon photoemission," Journal of Electron Spectroscopy and Related Phenomena **124**, 245 (2002)

[180] Träger, F., *Sringer Handbook of Lasers and Optics* (Springer, 2007)

# Publications

- M. Dąbrowski, T. R. F. Peixoto, M. Pazgan, A. Winkelmann, M. Cinal, T. Nakagawa, Y. Takagi, T. Yokoyama, F. Bisio, U. Bauer, F. Yildiz, M. Przybylski and J. Kirschner, *Oscillations of the Orbital Magnetic Moment due to d-Band Quantum Well States*, Phys. Rev. Lett., **113**, 067203 (2014)

# Acknowledgments

# Erklärung an Eides statt

Hiermit erkläre ich, dass ich die vorliegende Dissertation

*"Low dimensional electronic states at metal surfaces investigated by photoemission and nonlinear optics"*

selbständig und ohne fremde Hilfe verfasst und keine anderen als die von mir angegebenen Quellen und Hilfsmittel benutzt habe. Die den benutzten Werken wörtlich oder inhaltlich entnommenen Stellen sind als solche kenntlich gemacht habe. Weiterhin erkläre ich, dass ich bisher keine vergeblichen Promotionsversuche unternommen habe.

Halle, den 03.06.2014

Mariusz Pazgan

# Curriculum vitae

## Personal data

| | |
|---|---|
| Surname | Pazgan |
| First name | Mariusz |
| Date of birth | 22.04.1982 |
| Place of birth | Nowy Sącz |
| Nationality | Polish |

## Contact Information

| | |
|---|---|
| Address | Weinberg 2<br>D-06120 Halle (Saale)<br>Germany |
| Email | pazganov@gmail.com |

## Education

| | |
|---|---|
| 04/2010-04/2014 | PhD student at the Max Planck Institute of Microstructure Physics, Halle |
| 03/2005-05/2007 | University of Wrocław<br>Masters studies on Faculty of Physics and Astronomy; completed studies in the field of Physics, majoring in Experimental Physics |
| 10/2001-02/2005 | University of Wrocław<br>Bachelors studies on Faculty of Physics and Astronomy; completed studies in the field of Physics, majoring in Experimental Physics |

Halle (Saale), 03.06.2014

Mariusz Pazgan